Effect of welding induced residual stresses on compressive failure load of column structures

S. Hoogendorp

A thesis presented for the degree of
Master of Science

Faculty of Aerospace Engineering
TU Delft
The Netherlands
September 16, 2019

Delft University Of Technology

Faculty of Aerospace Engineering

Master of Science Thesis

Effect of welding induced residual stresses on compressive failure load of column structures

S. Hoogendorp

September 16, 2019

Graduation Committee

Chair:	Dr. Ir. S.R. Turteltaub	TU Delft
Committee members:	Ir. C.W. Leenders	Femto Engineering
	Dr. ing. S.G.P. Castro	TU Delft
	Ir. J. Sinke	TU Delft

femto engineering

TU Delft

Abstract

Structural members carrying dominantly compressive forces are present in many types of structure. These members are referred to as columns and are frequently present in for example lifting appliances and offshore structures. Whether or not a column consists of longitudinally welded subsections is relevant for its mechanical performance in compression. Steel columns consisting of longitudinally welded members contain residual stresses caused by the non uniform longitudinal expansion and shrinkage during the welding process. The distribution and magnitude of these residual stresses are dependent on the dimensions of the heat affected zone (HAZ), and varies for instance as function of the welding procedure, and whether or not post weld measures are taken to diminish these residual stresses.

In this thesis the width of the region in a column's cross section where tensile residual stress is present is referred to as the HAZ width. Using practical experiments an estimate is made of realistic HAZ widths in column structures using finite element analyses. These column structures where welded and kept free of restraints during this process, so that a resulting curvature is developed upon cooling down to ambient temperature. The established value of the width of the tension zone is on the order of the thickness of the column's cross section.

Based on existing norms a trapezoidal distribution of residual stress having a width of the earlier found value is applied on a finite element model of a single square column, both for pinned and clamped boundary conditions. Mesh independence of the obtained results are verified by convergence studies. The compressive load capacity of the considered column is affected in the intermediate range of slenderness ratios, and shows a maximum reduction of approximately 21%.

The effect of welding residual stresses is also investigated on a scaled model inspired by an existing design of a tower crane. A crane section is modelled by four vertical columns connected by multiple side bars. These side bars reduce the effective slenderness ratio of the columns loaded in compression, and therefore a less severe effect of the residual stresses on the collapse load is found.

Acknowledgements

As the concluding act for a student, I expected during the initial phase of the thesis that the process of doing a master thesis would be rather straightforward. However, reality turned out to be a little different, to say mildly. During my thesis I relived every experience that was also present during the entire period as a student up to the moment of starting the thesis. Sometimes I felt victorious for having a major breakthrough in the research, which is comparable to the feeling of passing a difficult and tough exam. On the other side there were moments of struggling and setback where I realized the value of having good friends and relatives. They provided me with the right amount of help and motivation to finish the master thesis and obtaining a Master of Science degree.

In the first place I would like to thank Stijn Leenders and Sergio Turteltaub for guiding me through the thesis, both for providing perfect technical feedback and for showing their social skills during moments of difficulty. In addition to these Tom Santegoeds and Eric Romeijn can not be missing, for letting me perfom my thesis at Femto Engineering and performing experimental research at Huisman Equipment respectively.

Besides the people who where directly involved in my research, I would like to thank (in random order) Nelly, Jos, Gerben, Arjan, Marcel and Stefanie for their support. Last but not least I am grateful for working with my colleagues at Femto Engineering, and my fellow students at the TU Delft.

Contents

List of Figures

List of Tables

Chapter 1

Introduction

Arc welding is a widely used joining technique that has proven to be able to produce structures with great structural integrity at relatively low costs. Welding requires a large energy input, and a quantitative analysis of a welding process is a complex and multi-discipline field in science. When designing a welded structure the effects of the welding process on the structural performance should be considered with great care. It is commonly known that welding can alter material strength, ductility and crack growth resistance locally near the weld. Due to the local nature of the heat input, large temperature gradients in the region near the weld occur, resulting in the formation of residual stresses. Because these stresses are present even though no external load is applied to the structure, a balance between tensile and compressive stresses has to be established in order to maintain equilibrium of the structure. The effect of these welding induced residual stresses on the collapse load of a welded column and of a welded truss structure is studied in this thesis.

1.1 Background

Structural members carrying dominantly compressive forces are present in almost any type of structure. These members are referred to as columns and are frequently present in for example lifting appliances and offshore structures. Whether or not a column consists of longitudinally welded subsections is relevant for its mechanical performance in compression. Steel columns consisting of longitudinally welded members contain *residual stresses* caused by the longitudinal expansion and shrinkage during the welding process. The distribution and magnitude of these residual stresses are dependent on the welding procedure, and whether or not post weld measures are taken to diminish these residual stresses. For long, slender columns the longitudinal residual stresses will have a minor, if not, negligible effect on the compressive failure load, since elastic buckling will occur prior to exceeding the material's

limit stress. For moderate slender columns however, compressive residual stresses may induce an early onset of yielding compared to columns without these initial stresses. This will cause a reduction in compressive stiffness and can result in plasticity induced buckling. The reduction of the failure load due to welding induced residual stresses in columns has been a well known phenomenon since the early 20^{th} century. Research with numerical models has been performed since the 1960s to study the effects of residual stresses on the compressive failure load of a single column. In relevant design codes the reduction in compressive load capacity is therefore taken into account [7], [8]. In this thesis the study of the effect of residual stresses on the compressive failure load is extended to truss structures consisting of welded steel columns. Thereby the relevance of the geometry of the surrounding structure is revealed.

1.2 Research questions

Because the majority of research studies available nowadays is focussed on the reduction of compressive performance of a single column, the question arises whether these results can be extrapolated to the performance reduction of a truss structure consisting of columns with welding residual stresses. In structures consisting of multiple members the actual boundary conditions on the members are different compared to single columns, and alternative load paths in case of failure of one member might be present. The main research question therefore to be answered in this thesis is:

"What is the effect of welding induced residual stress in steel columns on the compressive failure load of a truss structure?"

In order to provide an answer to the above stated research question, the following subquestions are stated (and answered), thereby providing a guideline throughout the thesis:

1. What is the distribution and magnitude of welding induced residual stress and distortion in a column's cross section?
2. Can the distribution of stresses and welding shrinkage be correlated with performed physical tests?
3. What is the effect and magnitude of the residual stress distribution on the compressive failure load of a single column?
4. What is the sensitivity of the resistance against plasticity induced buckling of a single column regarding various intensities of residual stresses combined with geometric- and loading imperfections?
5. What is the influence of a surrounding truss structure with various geometric properties on the failure load in compression?

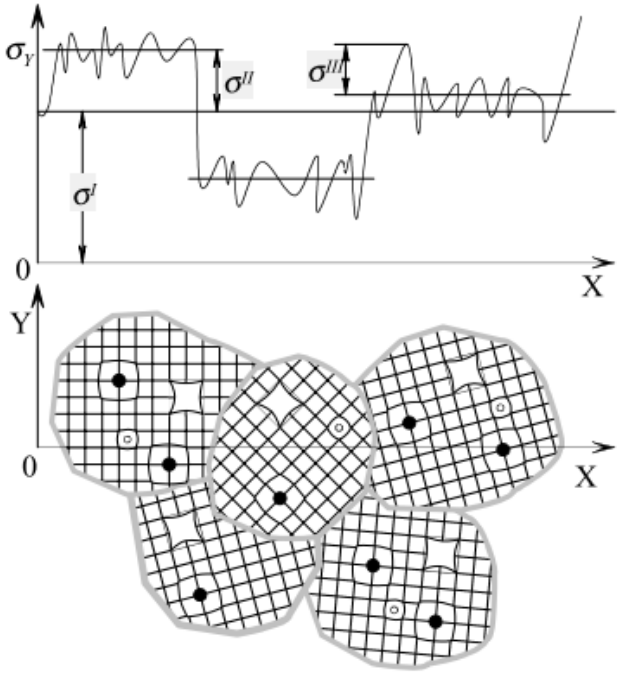

Figure 1.1: Global and local stresses present in material (from fig. II-7 [1])

Since the underlying mechanism of the occurrence of welding induced residual stresses is very complex, the depth of the research must be properly bounded. What factors and phenomena are taken into account in answering the above stated questions are discussed in section 1.3.

1.3 Scope

As mentioned earlier, a welding process involves many branches of computational sciences such as mechanics, thermodynamics, chemistry and electrical- and material engineering. To study the mechanical effects of the welding process, the required level of knowledge of these fields depends on the level of detail to be modelled. In the present thesis only the *global* mechanical effects of a welding process in compressive structural members are taken into account. In a material stresses occur at multiple levels of magnitude. As can be seen in figure 1.1, global stresses (σ^I) are stresses present on average over a distance of multiple grains. In reality the actual present stress may deviate from this average level due to for example varying grain orientation (σ^{II}) and atomic impurities or dislocations (σ^{III}). The actual variations in σ^{II} and σ^{III} are not of great relevance when considering the deformation and stresses in a structure with dimensions in the order of magnitude of meters.

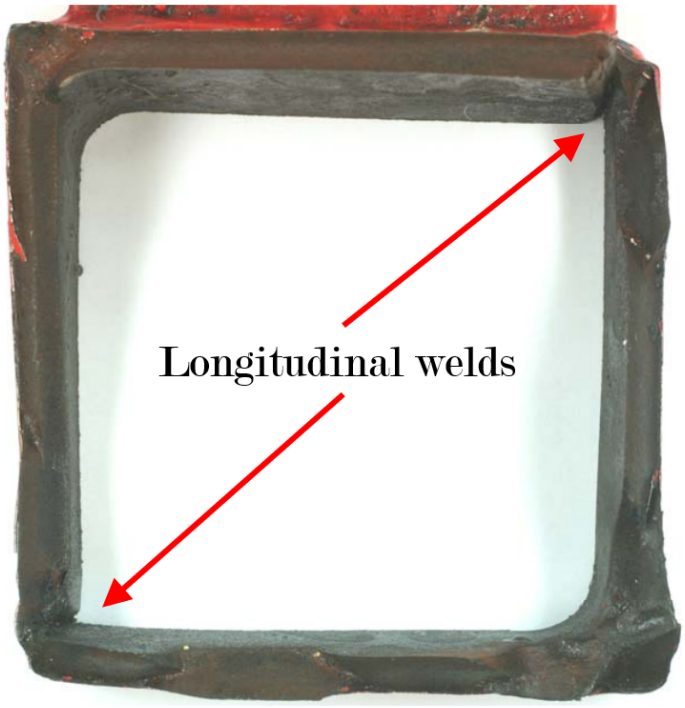

Figure 1.2: Cross section of welded box section, as used in crane structure ([2])

Therefore, in the scope of this thesis a model of the welding induced stresses is considered valid when it is able to predict the global stress σ^I with reasonable accuracy. Moreover, the only materials considered are structural steels, and the welding processes covered are arc welding processes, as these are the most applied techniques for welding structural steel. An introduction in the mechanical effects of arc welding is presented in chapter 2.

The compressive structural members considered are square hollow columns, as used frequently in cranes and offshore structures. In figure 1.2 a column cross section is shown as was used in a construction site tower crane. The shown cross section consists of two longitudinally welded L-profiles, and was installed in each of the four column members in the vertical 'tower' section of the crane structure. In this thesis the compressive failure loads of single columns and truss structures with the two welded L-profiles for various situations are compared with the failure loads for the same column geometry without the longitudinal welds. The results are normalized so that comparison with members of different dimensions is made possible.

1.4 Structure of report

In order to analyze the structural performance of a welded structure in compression, the effect of a welding process should be clear and ready to be applied in a model. An introduction to the effects of an arc welding process is given in chapter 2. In this chapter the working principle of a welding process is explained, as well as the origin of the welding induced distortion and residual stresses.

Experiments are performed to obtain an impression of the magnitude of the zone affected by the welding induced stress. This knowledge is applied in later chapters when the structural performance in compression is investigated using finite element models. A detailed description of the execution of the experiments and how relevant data is extracted from these tests is presented in chapter 3.

Prior to investigating the effect of welding induced residual stresses in structural members for a complete structure, the effect on the failure loads for single columns is quantified first. In chapter 5 the failure loads are determined for a theoretical 'perfect' column. Because this is a rather theoretical exercise, failure loads for columns with imperfections are determined in the next chapters. Chapter 6 presents the effect of failure load reduction for a column with a load offset, and chapter 7 does the same for columns having an initial curvature. By comparing the failure loads for columns with and without residual stresses reduction factors can be established.

The effect on the collapse load for a truss structure where its columns are affected by welding residual stresses is studied in chapter 8.

Chapter 2

Welding induced residual stress

The mechanical consequences of a welding process are build on in upcoming chapters. Therefore relevant background information on welding is presented in this chapter. In section 2.1 a general introduction of the fusion welding process is given. The formation of welding induced residual stresses is explained in section 2.2. Finally important factors that may influence the formation of these residual stresses are briefly described in section 2.3.

2.1 Introduction to welding

By definition a construction never consists of a single part, but of multiple structural components joined together. Welding is one of the available techniques to join structural parts and form a new (sub)structure. Other examples of joining methods with different working principles compared to welding are bolting, riveting and gluing. Among the multiple joining methods of steels, welding is a widely used technique. Welded joints are able to obtain a high joint efficiency, are air and watertight, allow simple structural design and may be produced in a short time. The method of welding can be subdivided in *fusion welding* and *solid-state welding*. The difference between these techniques is that in solid-state welding the joining of sub parts is not established by locally melting these parts. The working principle of fusion welding is to add heat and cause local melting of the sub parts at their joint interface, with or without the addition of a filler material. At the location of the former joint interface material in a liquid state is now present. This liquid material is able to flow and thereby removes the former joint interface. Upon cooling down this liquefied material solidifies resulting in a joined structure in solid state with a strong metallurgical bonding.

Nowadays widely used welding processes are *arc welding* processes. An electric field is applied over the workpieces and the welding torch. When

the intensity of this electric field is high enough, the interlaying gas between workpiece and electrode is ionized and as a result becomes electrical conductive. A stable flow of electric current is reached if the applied voltage and current produces an arc discharge. The product of voltage and electrical current is equal to the electrical power (energy per unit time). A large portion of this energy is transferred to the parts to be welded as heat.

The idea of using electricity as heat source was initialized during the industrial revolution. In 1800 Sir Humphry Davy managed to produce an arc between two carbon electrodes using a battery. When electricity became commercially available technological development of arc welding processes continued rapidly. Within the arc welding processes, a distinction can be made between several used configurations and equipment. In 1948 the *Gas Metal Arc Welding* (GMAW) process was invented by the Batelle Memorial Institute. In a GMAW process a continuously fed consumable electrode is used in the welding torch. The arc is shielded by a supplied gas, which can be an inert gas (such as argon), an active gas (such as carbon dioxide) or a mixture. The gasses are used to maintain a stable, high quality arc and a resulting high quality welding bond. When an inert gas is used, the process is called Metal Inert Gas (MIG) welding, and the term Metal Active Gas (MAG) welding is used for an active shielding gas. The GMAW processes are capable of fast welding passes, is relatively cheap and can be mechanized or fully automated. This makes the process very attractive for many production industries.

A typical cross section of a GMAW welded joint is shown in figure 2.1. The brownish area is fused weld metal, consisting from both the filler material and base metal (workpiece material). This fused area is surrounded by a small zone of fused metal consisting only of base metal, and is referred to as the *unmixed* zone, shown in blue. From this unmixed zone to the base metal (yellow) a transition zone is present, consisting of base metal that remained solid during welding, but have been exposed to microstructural evolutions in a more or less sense. This zone is called the *Heat-affected zone* (HAZ) and is shown in green. The width of the HAZ is dependent on factors as metal composition and heat input. The above given definition is the formal definition for the HAZ. For the global mechanical performance of a welded structure as done in this thesis, the exact boundaries and transitions of the defined zones near the weld are not of practical interest. The fact that there *is* a zone which is affected by the welding process and has shrunk is considered most important. Therefore the zone where welding induced shrinkage has occured is, however strictly incorrect, referred to as the heat-affected zone.

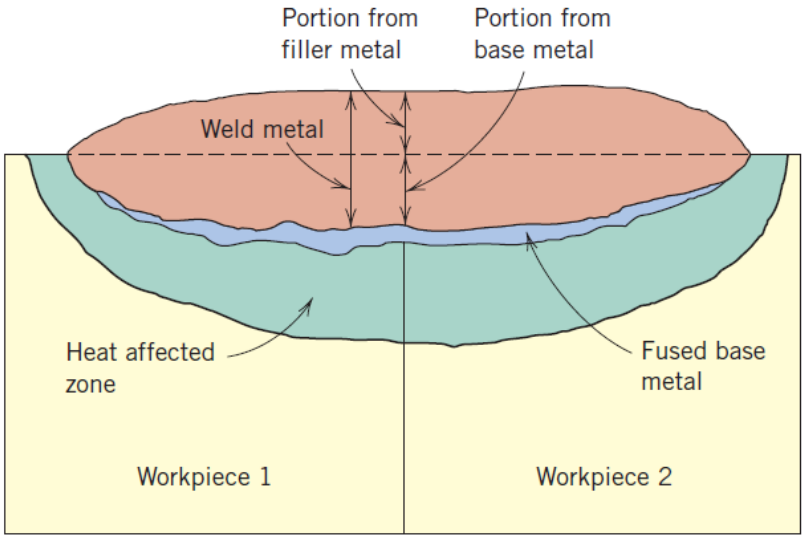

Figure 2.1: Typical cross section of fusion weld ([3])

2.2 Origin of welding induced residual stress

The local heat input as applied in a welding process produces mechanical effects referred to as *distortion* and *residual stress*. The underlying mechanism of these phenomena can be explained best in a simplified example. A longitudinally welded joint can be visualized in by a three bar model, as shown in figure 2.2. The weld line is schematized by the middle bar, and the surrounding base metal is represented by the two outer bars. The bars are rigidly connected at the ends, as shown by the grey boundaries. In the initial condition all material is assumed to be in a zero stress state and having the same temperature. During the approach of the welding arc the zone near the arc is heated, which can be shown by the middle bar having an increased temperature. As a result thermal expansion causes the middle bar to elongate, but this elongation is partially resisted by the (cold) base metal. This results in a state of compression in the weld zone (middle bar) en tension in the base metal. Even though in this heating stage the length of the joint has increased compared to the initial condition, the resistance to thermal expansion causes compressive plastic deformation in the middle bar. When the welding arc has passed the cooling stage starts and thermal shrinkage occurs in the middle bar. Due to the compressive plastic deformation in the heating stage, the middle bar has now become shorter in length with respect to the neighbouring bars. The thermal shrinkage is again resisted, causing a state of tension in the middle bar and compression in the outer bars. As can be seen, after cooling down to ambient temperature the joint

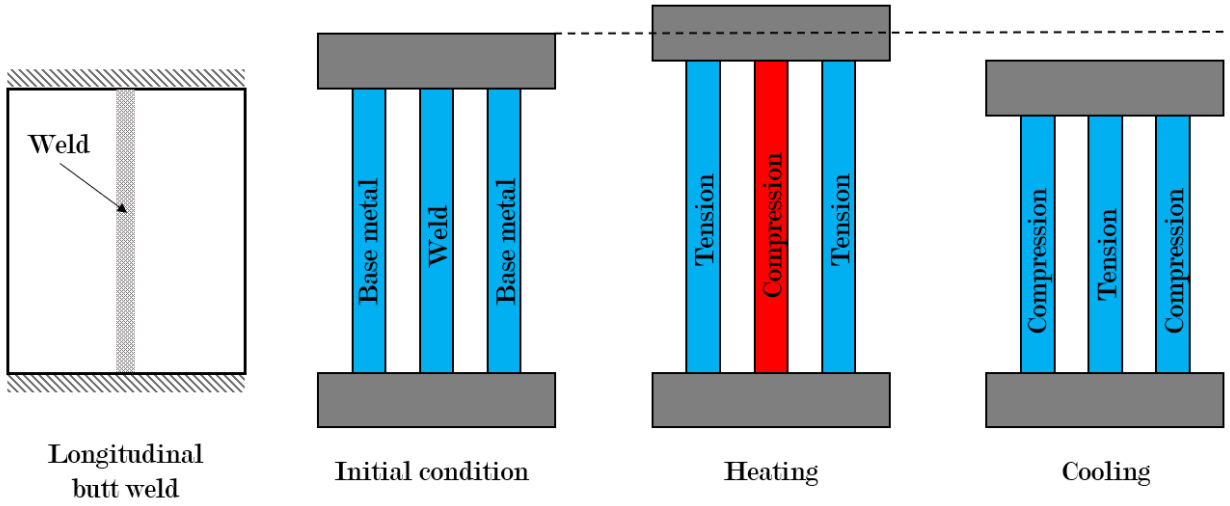

Figure 2.2: Simplified model of welding heat cycle

has shrunk compared to the initial condition. This resulting deformation is referred to as welding distortion, and the final stress state is called welding induced residual stress. This stress state remains in the joint even though no external load is applied.

The development of welding induced residual stresses is shown more detailed in figure 2.3. This figure consists of four graphs showing the history of temperature, stress and strain as a function of time. At the bottom right a typical temperature versus time curve is shown. The welding process starts at $t = t_0$. At $t = t_1$ the temperature is increasing, and the thermal strain increases linearly as shown in the bottom left figure. At this stage the compressive stress in the weld has reached the value of the plastic yield stress, as shown in the stress versus strain curve in the top left, and in the stress versus time plot in the top right. Until $t = t_2$ the temperature and thermal strain are increasing, while the stress has stabilized during plastic deformation. From $t = t_2$ via $t = t_3$ to $t = t_4$ the temperature is decreasing, as well as the thermal strain. The stress in the weld is increasing towards the value of the tensile yield stress, while deforming elastically. At $t = t_4$ the tensile yield stress level is reached and again plastic deformation occurs, but now with opposite sign compared to the heating stage. At $t = t_5$ the temperature has returned to its initial value, and the thermal strain is no longer present. A certain amount of plastic deformation is still present in the weld and the final stress state is reached. Because no external loads are applied, the tensile stresses near the weld are cancelled by compressive stresses in the base metal to maintain equilibrium.

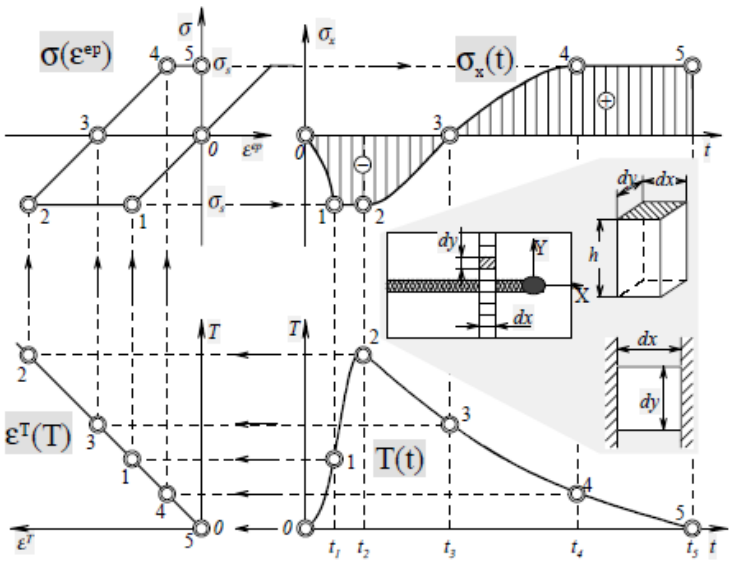

Figure 2.3: Formation of residual stress during welding process [1]

2.3 Factors of influence on residual stress

As described in previous sections, the longitudinal stress in general reaches the tensile yield stress in a zone near the weld. The exact distribution of the residual stresses is dependent on various factors. These factors are briefly described below.

Depending on the exact material composition (i.e. carbon content), microstructural evolutions occur during the temperature cycle in the welding process. The microstructure of high alloyed steels transforms to austenite at elevated temperatures. Upon cooling phase transformations occur, and the exact composition and phases present is depending on the cooling time. The specific volume of a stable microstructure at ambient temperature may vary from the specific volume of high temperature austenite. This phenomenon is referred to as transformation induced plasticity and can cause relaxation in the formation of the tensile residual stress near the weld [9].

The restraints applied to the joint during the welding process influences both the amount of distortion and the formation of residual stress. As expected, a high amount of restriction (clamping) reduces the freedom to deform, resulting in a low amount of distortion. In general it can be stated that the more restraint is present during welding, the less distortion will occur. For residual stress the opposite relation is true. For an increasing amount of restraint, the thermal and transformation strains are counteracted in an increased sense. This produces a higher tensile stress near the weld and as a result higher compressive stresses in the neighbouring base metal.

Applying heat *before* the actual welding arc passage is called pre-heating. This raises the effective initial temperature of the welding process, thereby reducing the temperature difference between the peak temperature and "initial" temperature. This reduced temperature difference causes a less severe local heat cycle and reduces residual stress formation. Moreover, pre-heating also causes a slower cooling rate thereby influencing the microstructural changes upon cooling. The whole joint can also be heated *after* the welding process, this is a so called post weld heat treatment (PWHT). During the PWHT the temperature is raised uniformly to a level high enough to cause atoms in the material to form new bonds with lower energy, but the temperature must be low enough to prevent phase changes. PWHT is an effective process to reduce welding induced residual stresses, however it is costly and may be impractical or even impossible for large constructions.

Various steel alloys may have different values for their coefficient of thermal conductivity. A relative high conductivity produces a more even heat distribution around the weld zone, reducing the temperature gradient in this zone and thus causing less restriction against thermal expansion and contraction compared to a low conductivity [10].

A welded joint cannot always be made with a single weld pass, and a multi-step welding process is used. From a residual stress point of view the amount of welding layers on top of each other should be as little as possible. However, when multiple layers are unavoidable, attention must be paid to the welding sequence. The sequence of the welding steps must be done in a symmetrical and balanced way [11].

Chapter 3

Width of Heat Affected Zone

To determine the width of the heat affected zone (HAZ) due to an arc welding process, practical measurements are performed. Section 3.1 explains the methodology and the reasoning behind the experiments. A description of *how* the measurements are executed is given in section 3.2. The procedure of extracting relevant data from these measurements is described in section 3.3. The finite element models used to simulate the shrinkage force in the specimen and the obtained widths of the HAZ are presented in sections 3.4 and 3.5 respectively.

3.1 Methodology

The width of the heat affected zone in a steel specimen is derived by assuming a residual stress distribution found in existing literature. As explained in chapter 2, the welding process causes the specimen to deform with respect to its initial unwelded state, where the shape and magnitude of deformation are dependent on the applied displacement boundary conditions during welding. In this experiment the specimens were able to deform freely, and the deformed shape is reconstructed in finite element analysis. Using the assumed residual stress distribution, the width of the "shrinkage" zone, also referred to as HAZ in this thesis, can be established.

Distribution Of Residual Stress

A brief description about the formation of residual stresses due to welding was given in section 2.2. In figure 3.1 a slightly more detailed overview is shown of the formation of these stresses. In this figure the heat cycle and stress state are plotted at four stages for a specimen welded from bottom to top. Cross section A-A is ahead of the welding torch and therefore has a uniform ambient temperature and has an assumed average zero stress state. Section B-B is at the exact location of the welding torch and therefore

shows a highly non-uniform temperature distribution ranging from melting temperature at the weld to ambient temperature further away from the weld. At the weld location the stress is zero because material has locally molten, but neighbouring material still in solid phase is under compression due to restriction in thermal expansion. This local compressive stresses are equilibrated by tensile stresses in cold material. In section C-C the material is cooling down, as can be seen by the diffused temperature distribution. During this cooling stage the thermal shrinkage near the weld is restricted and therefore tensile stresses start to develop, compensated by compressive stresses in neighbouring colder material. In section D-D the temperature is again uniformly distributed with a value equal to the ambient temperature. The final stress state has now been reached, with a narrow zone of high tensile stresses near the weld, compensated by a larger area with compressive stress. It can be shown that the tensile stresses near the weld in general have reached the material‘s yield stress. This assumption is valid for low strength steels, but for high strength steels other effects play a role in the formation of residual stresses, so that the yield stress is not always reached. As a simplifying assumption, the distribution of longitudinal residual stresses is assumed to have a small area with constant stress at yield level. This model is used for strength analysis by the Swedish handbook for steel welded structures. Schematic distributions as such are shown in figure 3.2, where f_y represents the material‘s yield stress. The HAZ is modelled as a zone with constant yield stress over a certain width, followed by an area of the same width where the stress returns to the value of the equilibrating compressive stress. The width of the HAZ is the variable to find based on physical tests.

Determining Curvature Of Welded Specimens

A total of eight specimens are constructed with various welding parameters such as joint geometry, heat input, material- and plate thickness. All specimens have a large length compared to their cross sectional dimensions, so that a model of a beam can be used to describe its mechanical behaviour. Therefore from now on the specimens are referred to as beams during mechanical analysis. The welds are placed with an offset with respect to the beam‘s neutral axes so that the “shrink force” causes a bending moment. The weld parameters are kept constant over the length of the beam so that it is assumed that the tendency to bend is constant over the length of the beam. According to general linear beam theory, the curvature of the beam must be constant when a constant moment M is applied over the beam:

$$\frac{d^2y}{dx^2} = \frac{M}{EI} \tag{3.1}$$

Given that the Young‘s modulus E and moment of inertia I are constants as well. The geometrical shape with constant curvature is a circular arc,

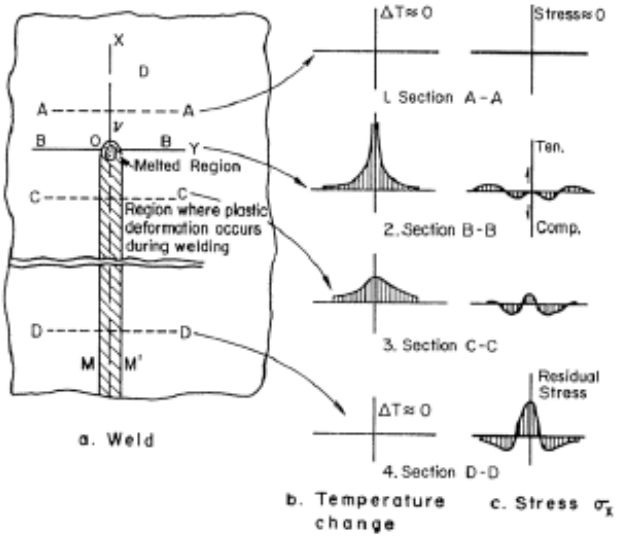

Figure 3.1: Formation of longitudinal residual stresses due to welding [4]

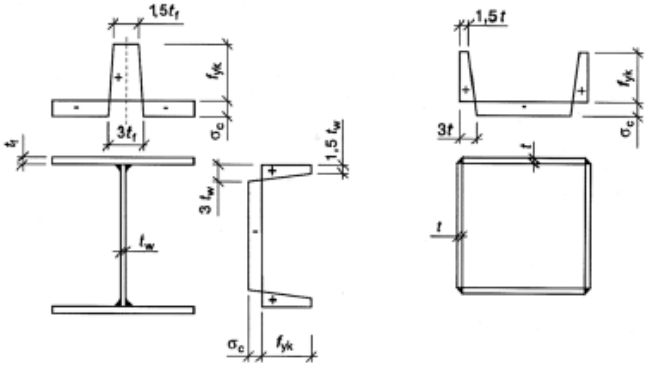

Figure 3.2: Simplified models of longitudinal residual stress distributions in welded beams [5]

therefore it is expected that the resulting displacement due to the welding process is circular. In the derivation of above formula it was assumed that the beam undergoes small deformations, so that the beam's curvature can be approximated by the second derivative of displacement in primary direction with respect to the beam's distance over the length. That is:

$$\kappa = \frac{\frac{d^2y}{dx^2}}{\left(1 + \left(\frac{dy}{dx}\right)^2\right)^{\frac{3}{2}}} \tag{3.2}$$

$$\kappa \approx \frac{d^2y}{dx^2} \quad \text{if} \quad \frac{dy}{dx} \ll 1$$

Using a scanning machine provided by Faro® the outer surfaces of the beams are scanned before and after the welding process. The difference between these two scans provide the displacement of the measured points along the beam. These displacements are fitted with a circle by a least square regression algorithm. Using the assumed distribution of residual stresses presented in subsection 3.1 the width of the HAZ needed to produce the measured curvature is determined using finite element models.

Finite element model

Using a linear elastic finite element analysis of the beam, the measured curvature can be reconstructed by applying a zone of thermal shrinkage near the weld. The total strain tensor $\boldsymbol{\varepsilon}^{tot}$ for the model's plate elements can then be written as the sum of elastic- ($\boldsymbol{\varepsilon}^{e}$) and thermal strain ($\boldsymbol{\varepsilon}^{th}$):

$$\boldsymbol{\varepsilon}^{tot} = \begin{pmatrix} \varepsilon_x \\ \varepsilon_y \\ \varepsilon_{xy} \end{pmatrix}^{tot} = \boldsymbol{\varepsilon}^{e} + \boldsymbol{\varepsilon}^{th} = \begin{pmatrix} \varepsilon_x \\ \varepsilon_y \\ \varepsilon_{xy} \end{pmatrix}^{e} + \begin{pmatrix} \alpha\Delta T \\ \alpha\Delta T \\ 0 \end{pmatrix} \tag{3.3}$$

Where α is the coefficient of linear thermal expansion and ΔT is the difference in temperature with respect to the reference temperature, which is set to zero. The resulting stress state is then calculated as follows:

$$\boldsymbol{\sigma} = \mathbf{D}\left(\boldsymbol{\varepsilon}^{tot} + \boldsymbol{\varepsilon}^{th}\right) \tag{3.4}$$

Where $\mathbf{D}$ is the constitutive matrix for isotropic material in plane stress. The thermal load on the beam model is applied such that the stress $\boldsymbol{\sigma}$ is equal to the material's yield stress in a given width of the HAZ, and the resulting curvature is read. The search is considered complete when a certain width of the HAZ produces the same curvature of the beam as measured by the tests.

3.2 Measurements

In this section is described how the physical experiments were performed. First an overview is given of the specimens that are welded. Respectively the welding procedure and scanning procedure are described in subsequent subsections. Photographs of the specimen being scanned and welded are attached in Appendix A.

Specimen overview

In table 3.1 an overview is given of the specimens that are welded for the tests. The geometry of these specimens is schematically shown in figure 3.3. Throughout the remainder of this report the specimen are referred to their code letter. The fillet weld in subfigure 1 in figure 3.3 is changed in dimension for various specimens. Therefore the weld dimension is referred to as FWa in the figure.

Table 3.1: Overview of welded specimen

Code	Description	Thickness [mm]	Material	Profile	See subfigure
A	FW6	10	S355	T	1
B	t = 25mm	25	S355	T	1
C	FW5	10	S355	T	1
D	FW7 multi-pass	10	S355	T	1
E	FW4	10	S355	T	1
F	S690	10	S690	T	1
G	L-profile	10	S355	L	2
H	Box	10	S355	Box	3

Welding parameters

Prior to placing the weld over the specimen's full length, three tack welds of 65 mm are placed. One is located in the middle of the specimen, and the other two are placed symmetrically at a distance of about 210 to 220 mm away from the edge on each side. For specimens A to F the tack welds are placed at the opposite side of the joint where the full length fillet weld is placed. For specimen G and H the tack welds are placed in the prepared slot where also the full length weld is placed. A photograph of a placed tack weld is shown in Figure 3 1. The specimens listed in subsection 3.2 are welded with Gas Metal Arc Welding (GMAW) with a shielding gas containing 82% Argon and 18% Carbon dioxide. For the specimens with S355 as material a "4-60" filler wire is used, while the specimen with S690 as material "742" filler is used. An overview of the welding parameters used for the specimens is given in table 3.2.

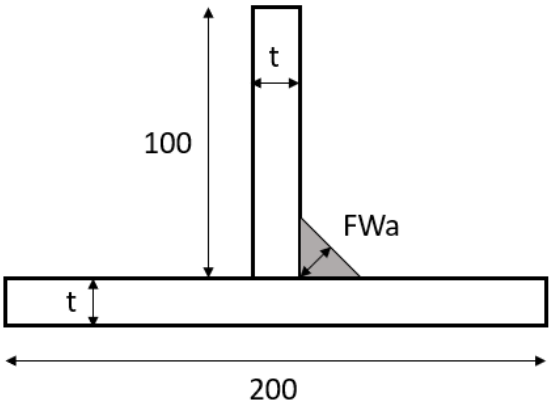

Subfigure 1: T-profile

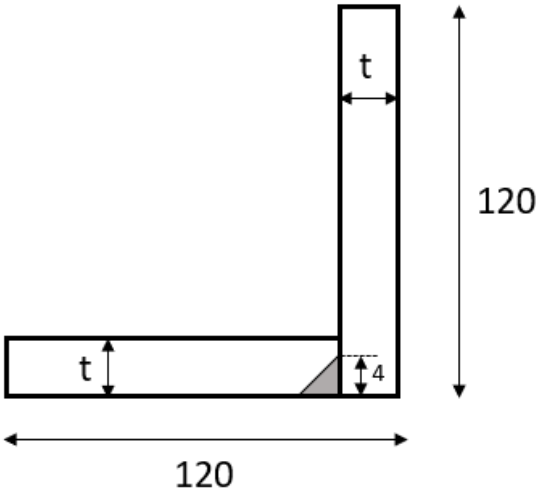

Subfigure 2: L-profile

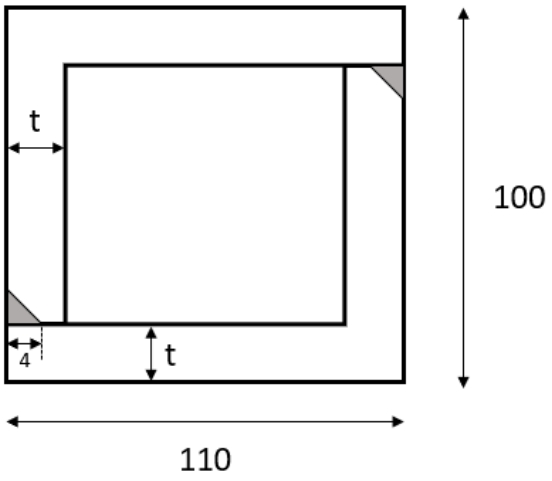

Subfigure 3: box-profile

Figure 3.3: Schematic cross sections of specimen

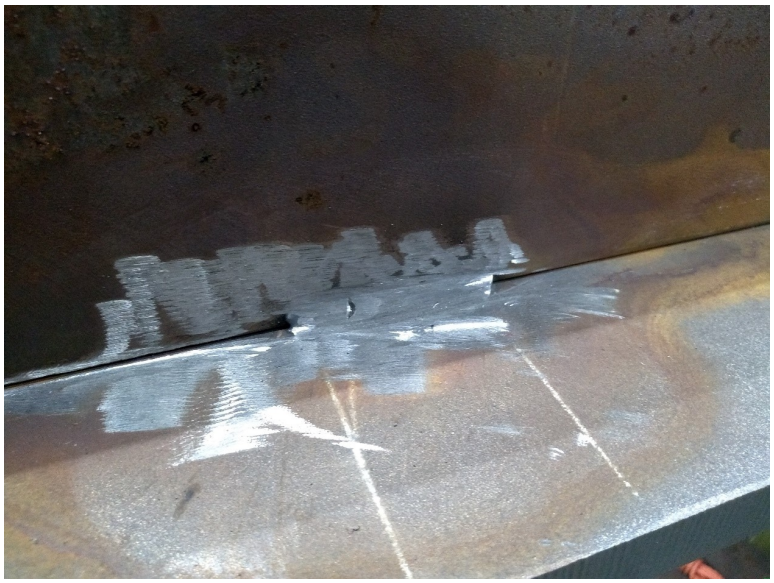

Figure 3.4: One of the three tack welds laid on specimen

Scanning procedure

By means of a demonstration, the company Faro was willing to scan the specimens using a costly measurement arm. The arm is mounted on a tripod, and free to move in all directions, inspired by the joints and movement of a human arm. The scanning device at the arm's end knows its position with respect to the tripod, and a laser beam is used to determine the distance towards the specimen. A photograph taken during scanning is shown in figure 3.5. The grid of sampling points of the measurement were set to a resolution of 2 mm, with an accuracy of ± 0.05 mm. Because the measurements before and after welding are not performed on the same day, a fixed reference on the specimens must be created. This is done by physically indenting the specimen at three distinct locations prior to the first scan. By pointing a measurement ball into these indents before the first and second scan, the orientation of the specimen in 3D space can be uniquely determined, and the two measurements can be compared. In practice it is hard to find three locations on a specimen that will not deform with respect to each other. Therefore the measurement result of the second scan is compared to the result of the first scan by a best-fit algorithm in the PolyWorks software. The resulting displacement of the reference points are shown in Appendix B.

The raw scanning data is made available in two PolyWorks ".pwzip."-files that can be opened with a free version of PolyWorks Viewer that can be downloaded from the web. In PolyWorks Viewer the scanning data is visualized by the intermediary surfaces between the data points. In this

Table 3.2: Welding specifications of specimen

Ref.	Description	Current [A]	Voltage [V]	Speed [cm/min]	Heat input [kJ/mm]
A	FW6	241	27.4	17.9	2.22
B	t = 25mm	237	27.4	19.3	2.02
C	FW5	250	27.5	20.0	2.06
D	FW7 pass 1	242	26.9	25.0	1.56
D	FW7 pass 2	240	26.9	25.0	1.55
D	FW7 pass 3	245	26.9	22.8	1.21
E	FW4	245	26.9	24.3	1.63
F	S690	237	27.4	19.3	2.02
G	L-profile	241	27.5	22.9	1.74
H	Box	260	27.7	21.4	2.01

way the scan data is represented by surfaces forming the outer contour of the beam. For data analysis use is made of the raw data points, and these are obtained by exporting the scan data to a ".txt"-file containing a list of point coordinates corresponding to the data points. The procedure of data extraction is described in section 3.3.

3.3 Data extraction

In this section the processing of the raw scanning data towards the resulting beam curvatures due to the welding process is described. This process involves three steps that are described in the corresponding subsections: Reading the measurement points along the length of the beam in the point cloud (subsection 3.3), determining the displacement between pre- and post-welding (subsection 3.3), and finally creating a circular fit on the obtained displacements (subsection 3.3). The results of the obtained circle are discussed in subsection 3.3.

Extracting measurement points

The scan data point cloud is available in a ".txt"-file containing the XYZ-coordinates of the measured points. In this coordinate reference system the X-axis is aligned along the beam's length, and the Y- and Z-axes are in the plane of the cross-section., as shown in figure 3.6. Since the sampling points are obtained using a hand-held scanner, the sampling locations are not structurally ordered in a regular mesh. To extract data points to analyze the beam's curvature in the XY- and ZX-plane, Python 3.6 scripts are written (attached in Appendix C). In these scripts the beam is divided in N sections along its length. For the script in Appendix C.1 in each section the

Figure 3.5: Faro measurement arm and operator in action during scanning

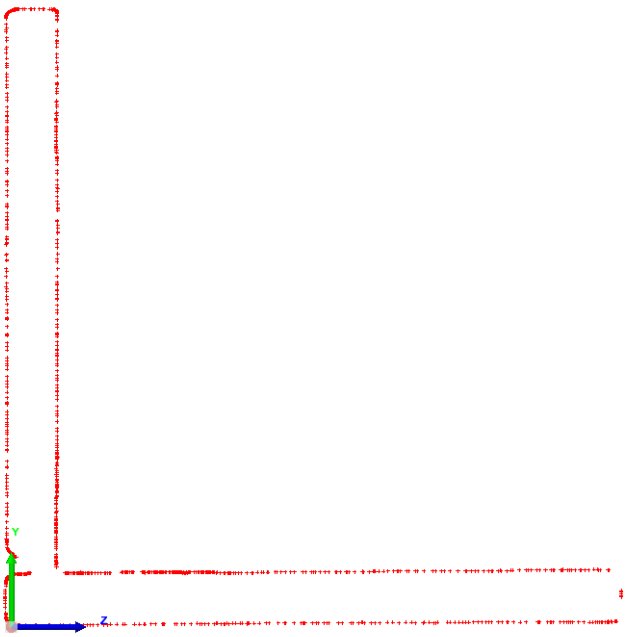

Figure 3.6: The Y- and Z-axes are in the cross-sectional plane

sampling point with maximum Y-coordinate is stored such that the output file contains a list with N sampling points. The sampling points originally stored in the output file for beam G before welding is show in figure 3.7. It should then be checked whether the stored sampling points are according to expectation and make sense. Note that here an outlying sampling point is present at the beam's end. If the location of the outlying sampling point is not on the beam section's aimed location, it is ignored in further analysis. For all specimen, the amount of sampling points is set to 250, so that an average distance of 10 mm is present between two consecutive points.

Determining difference in shape due to welding

When for all beams 250 sampling points are stored for the pre- and post-welded state, the difference in location between these two states is determined. Because the X-location for the 250 stored sampling points does not have to be equal for the pre- and post-welded beam, the Y- (or Z-) coordinates must be determined at identical X-locations for the two states for the same beam. In order to obtain the sampling data at identical X-locations, use is made of the Python 3.6 script in Appendix C.2. With linear interpolation the intermediary value for Y is expressed in terms of the already known values at a certain interval boundary according to equation (3.5). The visual representation is shown in figure 3.8.

$$y_{new} = y_l + \frac{y_r - y_l}{x_r - x_l}\left(x_{new} - x_l\right) \tag{3.5}$$

Substituting "z" for "y" in Equation results in an expression for the intermediary Z-coordinate of the sampling point.

Circle fit

A circle fit is made on the curves that represent the displacement due to the welding process using the python script in Appendix C.3. However, it should be noted that the curvature of the beam about its neutral plane should be circular. In the measurement data, only projections of the curved beam on the XY- and ZX-plane respectively are read. In reality these projections are ellipses with eccentricity greater than zero. Since the aim of the study is to match the measured displacements with displacements generated in a finite element model, it is sufficient to generate a circular approximation to the projections and do the same in the finite element model. In this way the deformation of the beam is uniquely described.

The circle that fits best has a radius r_c and center location (x_c, y_c). The distance between each data point i and the circle's center is given by equation (3.6).

$$r_i = \sqrt{(x_i - x_c)^2 + (y_i - y_c)^2} \tag{3.6}$$

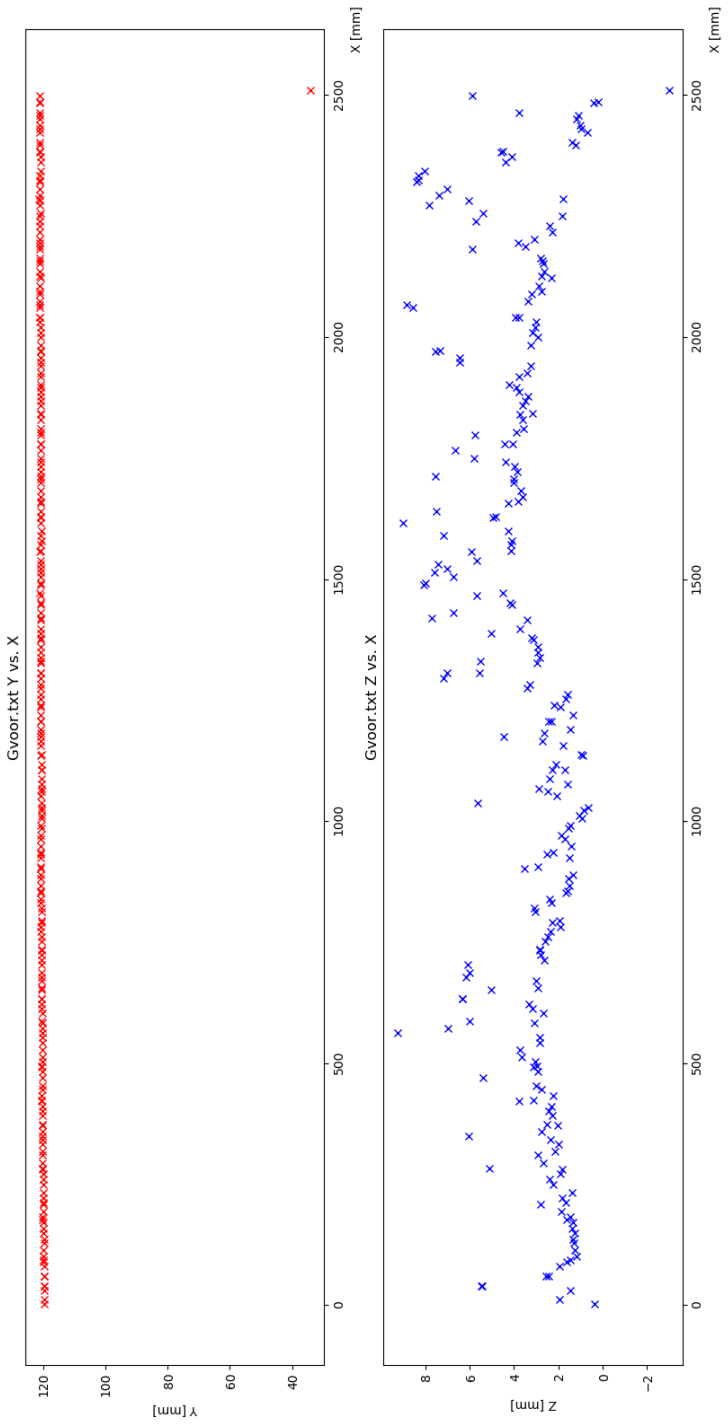

Figure 3.7: Left: 250 sampling points with maximum Y-coordinate. Right: The same points in ZX-plane

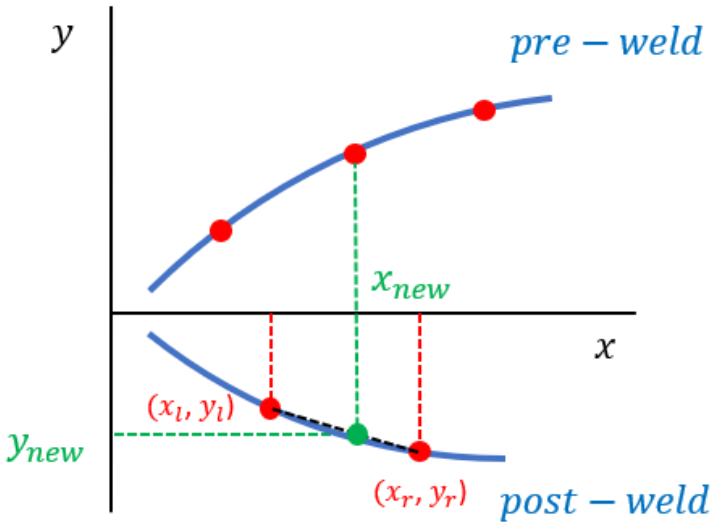

Figure 3.8: The new value y_{new} for the post-welded measurement has an identical x-location as that for the pre-welded measurement

The best fit found using the least squares regression method is the circle where the sum of the differences in radius squared Φ over all data points is minimum:

$$\Phi = \sum_{i=1}^{n} (r_i - r_c)^2 \tag{3.7}$$

Where r_c is the radius of the best fitting circle. The number of points N used for the circular regression determines the level of accuracy of the found radius of curvature r_c. To establish accurate results the output value for r_c is tested as function of the amount of points N for specimen G. These points are sampled equidistantly over the specimen's length. The results are presented in table 3.3. The relative difference in the third column is calculated as follows:

$$Relative\ difference = \frac{r_i - r_{i-1}}{r_{i-1}} \tag{3.8}$$

Where the subscript i is an integer number corresponding to an amount of points N as shown in table 3.3.

In figure 3.9 the relative difference is plotted versus the amount of points used for the circular regression. A converging trend is established for increasing values of N. It can be seen that the value found for r_c when 250 points are used varies -0.02% compared to when 125 points are used. Even though using 250 points may seem to be an unnecessary effort compared to its increase in accuracy, the computational costs are still negligible due to fast

Table 3.3: Overview of circle fits

i [-]	N [-]	r_c [m]	Relative difference [-]
1	3	51.71	-
2	6	51.12	-1.13%
3	12	51.06	-0.09%
4	25	51.15	$+0.15\%$
5	50	50.93	-0.43%
6	125	50.87	-0.12%
7	250	50.86	-0.02%

performing algorithms used for point selection and regression. Therefore 250 is the number used for the circular regression.

The output for beam G is shown in figure 3.10 and figure 3.11 respectively. Table 3.4 gives an overview of the curve fitting data for all specimens. In this table R_{xy} is the radius of curvature in the XY-plane, and Φ is defined in equation (3.7), which is a measure of how well the data is fitted by the circle. The radii of curvature in the ZX-plane for specimens A to F are considered negligible compared to the radii of curvature in the XY-plane. This is due to the fact that the T-profile specimens have a much higher bending stiffness in the ZX-plane.

Table 3.4: Overview of circle fits

Specimen	R_{xy}	Φ	R_{zx}	Φ
A (T-profile)	152	33.80	$\gg R_{xy}$	-
B (T-profile)	-	-	$\gg R_{xy}$	-
C (T-profile)	148	28.37	$\gg R_{xy}$	-
D (T-profile)	211	24.44	$\gg R_{xy}$	-
E (T-profile)	260	23.39	$\gg R_{xy}$	-
F (T-profile)	576	34.32	$\gg R_{xy}$	-
G (L-profile)	51	3.93	48	6.81
H (Box-profile)	331	1.91	275	2.85

Critical note on results

From the results listed in table 3.4 and the plots in Appendix D it can be concluded that the displacement data contains noise for specimens A to F. These displacement curves are heavily waved so that it is not trivial to discover a global trend, and an average curvature represented by the circle fit is therefore not reliable. This is also the case when the curvatures in the specimen are very small. The fluctuations from a circular trend are most

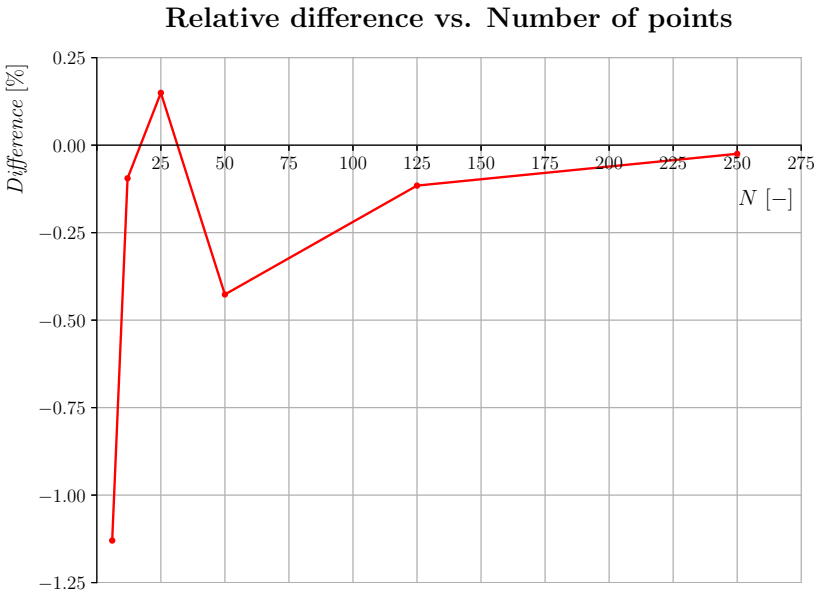

Figure 3.9: Relative difference of radii of curvature for various amount of data points

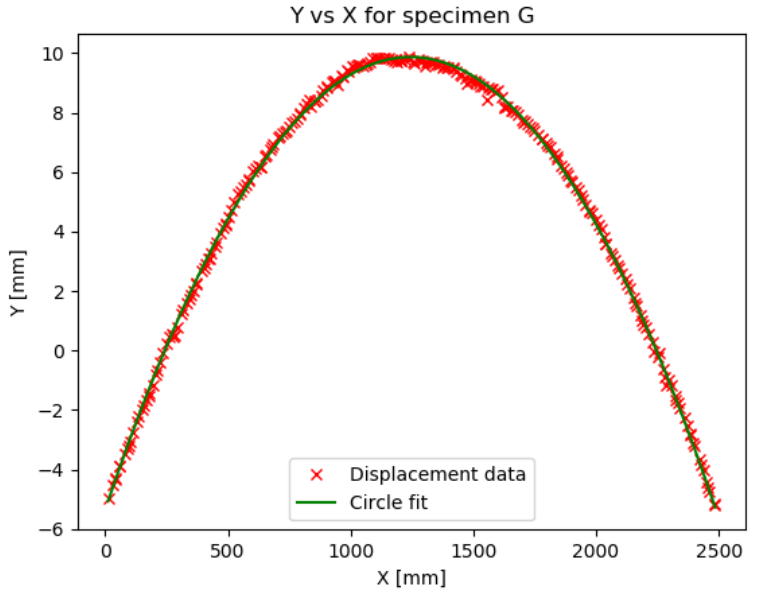

Figure 3.10: Circle fit in XY-plane of specimen G

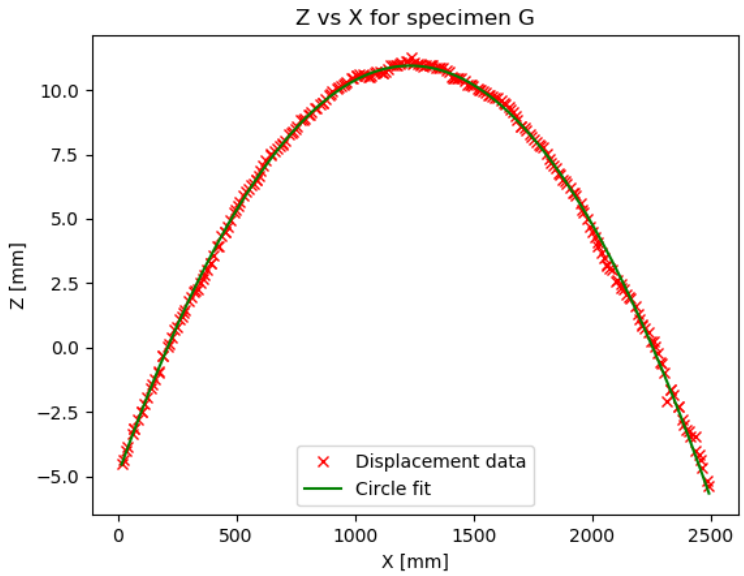

Figure 3.11: Circle fit in XZ-plane of specimen G

likely caused by the fact that the tack welds are located with an offset with respect to the full length weld in these specimens. The tack welds cause the beam to have no constant mechanical behaviour over its length, and keep their stiffness during the welding process of the full length weld. Therefore it is likely that the presence of these tack welds may have contributed to the disturbance in the displacement curves.

For specimen H the radii of curvature are 275m in the XZ-plane and 331m in the XY-plane after the addition of two welds placed on opposite sides of the box section. It is doubtful if a reliable conclusion can be drawn based on these measurements. The average axial shortening of the specimen may still provide information about the size of the two HAZs, but the measurements lack accuracy near the specimen's edges and therefore a reliable determination of the axial shortening based on this scanning data will hardly have physical significance. The error resulting in the measurement of the axial shortening will be large compared to the quantity to be measured. An image of the scan data at specimen H's edge is shown in figure 3.12. Specimen G shows a much more smooth displacement curve in both the XY- and XZ plane. Therefore the assessment of finding the width of the HAZ that matches measured displacement is continued only with specimen G.

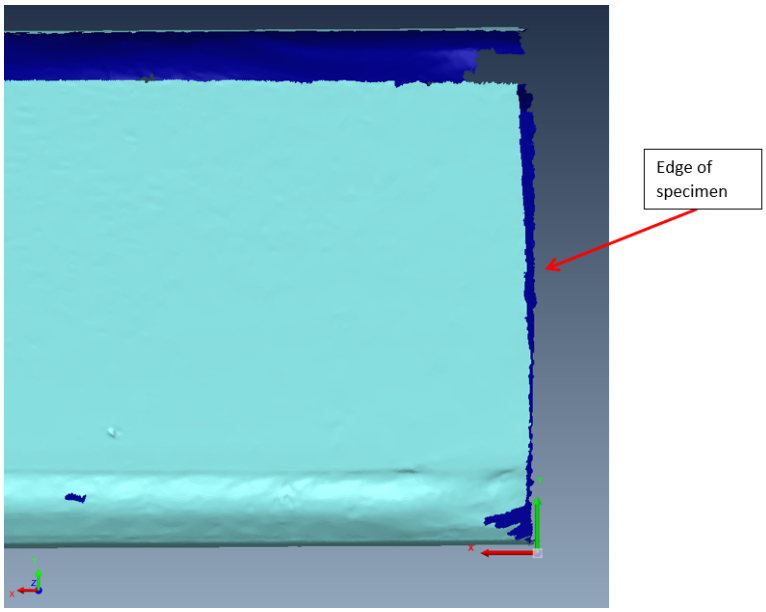

Figure 3.12: Edge of specimen H causes difficulty in determining axial shortening due to coarse scan resolution

3.4 Finite element analysis

This section describes the linear elastic finite element analysis performed. Mesh related properties as well as the used material properties are presented in subsection 3.4. The boundary condition used and the applied loads are shown in subsection 3.4. In subsection 3.4 it is aimed for to match the welding induced curvature by applying a symmetrical HAZ, and in subsection 3.4 an asymmetrical HAZ is applied.

Mesh- and material properties

The beam is meshed using linear 4-noded CQUAD4 plate elements. In figure 3.13 a cross section of the beam is shown. The HAZ consists of two elements in the cross-section, and the neighboring elements have half the dimension of the total width of the HAZ. Each beam has that amount of elements along its length such that the HAZ elements are squares. In table 3.5 the material properties used are listed.

Boundary condition and applied load

Because the beam is not loaded externally and is internally in a state of equilibrium, no reaction forces and moments are needed to solve for the stress state. Therefore the applied boundary condition is only applied to

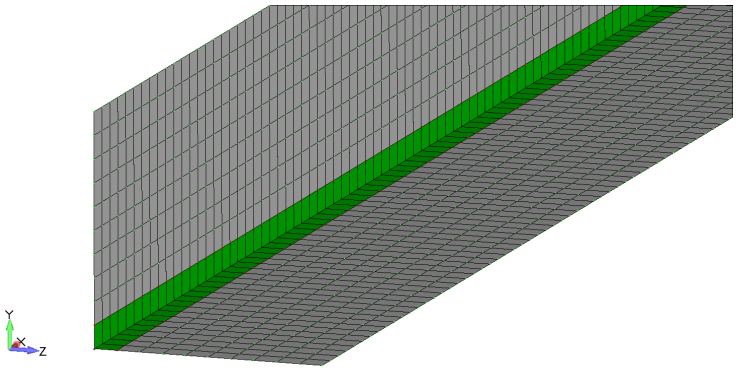

Figure 3.13: Plate mesh of specimen G with HAZ elements shown in green

Table 3.5: Mechanical properties of S355 steel

Property	Symbol	Value	Unit
Modulus of elasticity	E	211	GPa
Poisson's ratio	ν	0.3	-
Mass density	ρ	7850	kg/m^3
Yield stress	σ_y	355	MPa
Coefficient of thermal expansion	α	$1.1 \cdot 10^{-5}$	K^{-1}

avoid rigid body motions and hence a singular stiffness matrix. The node at mid length of the beam, at the intersection of the two beam sections is held fixed (123456). The application of this boundary condition is shown in figure 3.14. The shrinkage of the HAZ is modelled by applying a nodal temperature load on the nodes of the HAZ elements. Because the HAZ contains two elements in the cross section, three rows of nodes are loaded with temperatures. The thermal shrinkage of the HAZ elements are elastically resisted by the neighbouring elements, so that a tensile stress will occur in the HAZ. Using the model for the distribution of residual stresses due to welding (see subsection 3.1), the nodal temperature loads are given that value so that the material's yield stress is reached in longitudinal direction at the nodes of the HAZ elements. Because the HAZ is not located at the beam‘s neutral axis, both axial tension and bending stresses are introduced by the thermal shrinkage. The values for the nodal temperatures are found by iteration using a written API (Application Programming Interface), using the Newton-Raphson algorithm. The temperatures converge to a value where yielding in the plate elements starts to occur. In the used models, this is the plate‘s top X longitudinal stress. The application of the nodal temperatures to the HAZ elements is shown in figure 3.15.

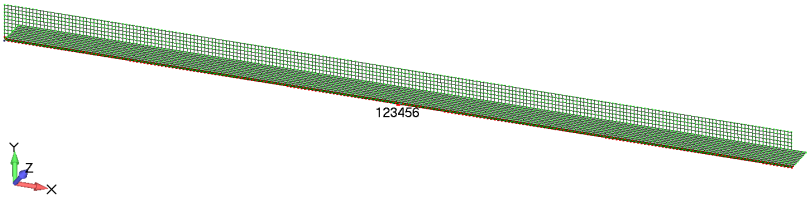

Figure 3.14: Clamped boundary condition at midlength

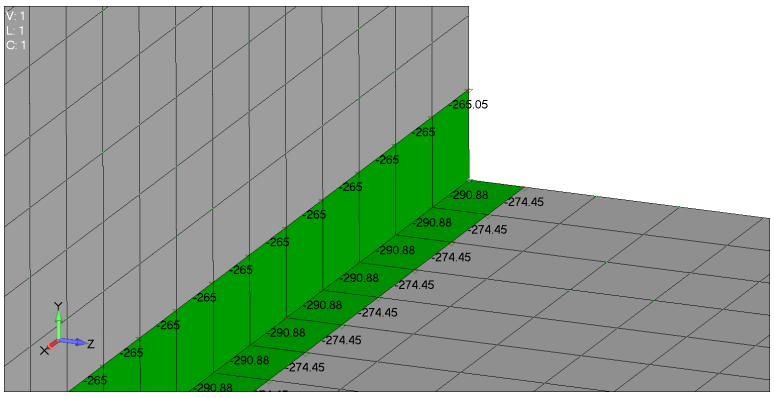

Figure 3.15: Nodal temperatures applied to nodes of the HAZ elements

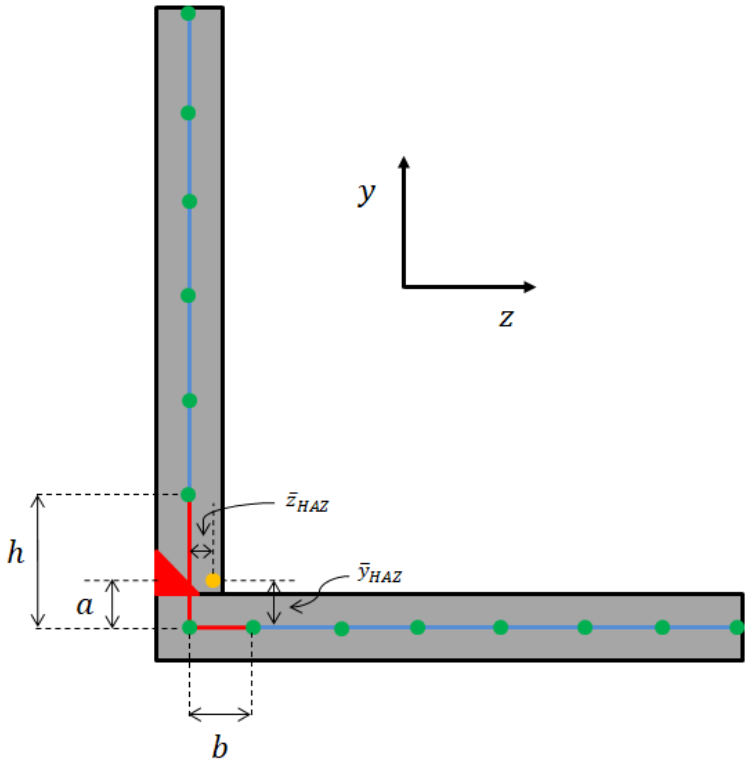

Figure 3.16: Schematization of applied HAZ on specimen G

Results for symmetric HAZ

A schematization of the plate model is shown in figure 3.16. In the figure h and b are the height and width of the HAZ elements respectively, and $\overline{y}_{HAZ}$ and $\overline{z}_{HAZ}$ are the coordinates of the geometrical center of the zone where the stress equals the material's yield stress. In this section the HAZ is applied symmetrically, so that $h = b$ and $\overline{y}_{HAZ} = \overline{z}_{HAZ}$. The distance a is the distance from the offset of the weld's center with respect to the midplane of the lower plate section. This distance is equal to:

$$a = 5 + \frac{4}{3} = 6.3\text{mm} \tag{3.9}$$

With the application of the symmetric HAZ, only one of the two curvature projections can be matched. The required dimensions of the HAZ elements to match the curvature projection in the XY plane are presented in table 3.6. It can be seen that a total width of the HAZ elements, which is equal to h+b, of 22.8mm is required. The curvature in the XY plane is matched with 0.34% error, and the curvature in the XZ-plane has an error of 6.03%.

Table 3.6: Results of finite element model with symmetric HAZ

Property	Value	Unit
Total width HAZ elements	22.8	mm
h	11.4	mm
b	11.4	mm
$\overline{y}_{HAZ}$	5.4	mm
$\overline{z}_{HAZ}$	5.4	mm
Max. y displacement	15.4	mm
Max. z displacement	15.4	mm
R_{xy} in FEM	51	m
Error w.r.t. measurement	-0.3%	-
R_{zx} in FEM	51	m
Error w.r.t. measurement	+6.0%	-

Results for the Plate Top longitudinal stress in undeformed and deformed state are shown in figure 3.17 and figure 3.18. The HAZ elements are clearly recognizable by the high (red) tensile stress in longitudinal direction. Outside the HAZ a region of compressive longitudinal stresses are present. No external loads are acting on the specimen, and therefore at the ends the stress state deviates from the prescribed residual stress distribution to a state of zero longitudinal stress.

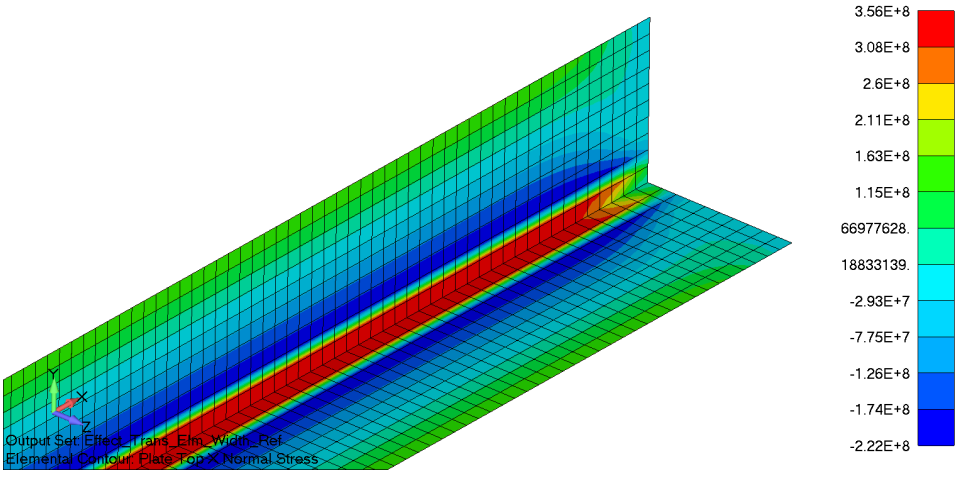

Figure 3.17: Plate top longitudinal stress (units in [Pa])

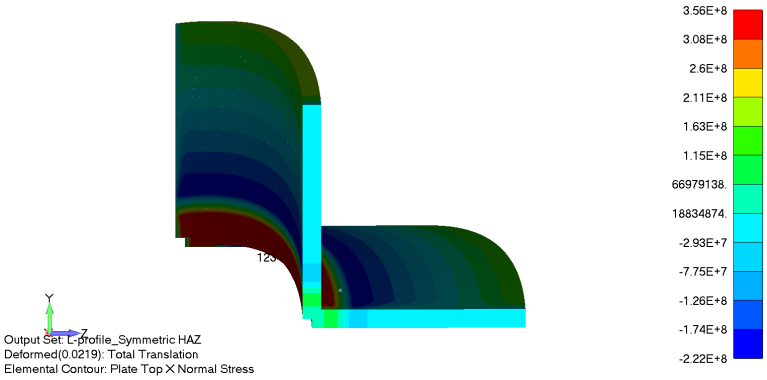

Figure 3.18: Plate top longitudinal stress on deformed specimen (units in [Pa])

Because the HAZ is applied symmetrically, the residual stress distribution in the finite element model is identical in both plate sections. The longitudinal stresses at the nodes are plotted in figure 3.19. With a symmetrically applied HAZ, the distance $\overline{y}_{HAZ}$ is not equal to a. In the next section the HAZ is applied so that these distances are equal, and the HAZ is located more according to reality.

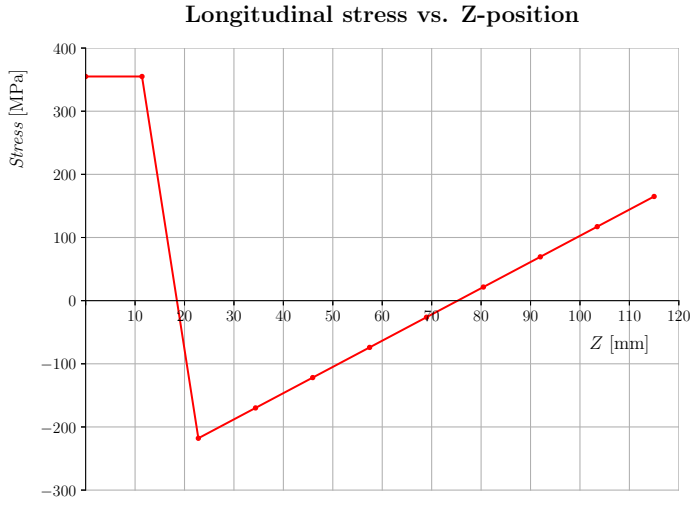

Figure 3.19: Longitudinal stress plotted versus Z-coordinate

Results for asymmetric HAZ

In this subsection the HAZ is applied so that the Y-coordinate of the center of the yield zone is equal to the Y-coordinate of the center of the weld. The required dimensions of the HAZ elements to match the curvature projection in the XY- and XZ planes are presented in table 3.7. It can be seen that a total width of the HAZ elements, which is equal to $h + b$, of 23.9mm is required. The curvature in the XY plane is matched with 1.1% error, and the curvature in the XZ-plane has an error of 0.3%.

Table 3.7: Results of finite element model with asymmetric HAZ

Property	Value	Unit
Total width HAZ elements	23.9	mm
h	17.4	mm
b	6.5	mm
$\overline{y}_{HAZ}$	6.3	mm
$\overline{z}_{HAZ}$	0.8	mm
Max. y displacement	15.5	mm
Max. z displacement	16.4	mm
R_{xy} in FEM	50	m
Error w.r.t. measurement	-1.1%	-
R_{zx} in FEM	48	m
Error w.r.t. measurement	-0.3%	-

3.5 Results

Based on the experiment performed the following conclusions are drawn:

- For specimens A to F (all T-profiles) it is considered that a mean resulting curvature due to the welding process is hard to establish. The disturbance in the data may have been caused by the placement of the three tack welds along the specimen.
- Based on the measurements performed the resulting radii of curvature due to the welding process in specimen H (box-section) are 331m in the XY-plane and 275m in the ZX plane. It is doubtful if a reliable conclusion can be drawn based on the small measured curvature. The small resulting curvature is a result of two (almost) balancing deformations due to the two welds.
- The average axial shortening of the specimen may still provide information about the size of the two HAZs, but the measurements lack accuracy near the specimen's edges and therefore a reliable determination of the axial shortening based on this scanning data will be difficult.
- Based on the measurements performed the resulting radii of curvature due to the welding process in specimen G (L-profile) are 51m in the XY-plane and 48m in the ZX plane. Assuming the distribution of residual stresses as presented in subsection 3.1, the required total width of the HAZ is 23.3mm. This HAZ is asymmetrically distributed with the center of the plastic zone matching the Y-location of the actual weld.
- When the same approach is applied to specimen A (T-profile), a total HAZ width of 73mm is required to match the measured curvature. However, because the offset of the weld and the specimen's neutral axis is small, the obtained results are prone to assumptions about the HAZ centroid.

Chapter 4

Finite element models of columns

The maximum load capacity of welded structures is determined using finite element analyses. A single column structure is discretized into a number of elements. The finite element representation of these structures is discussed in section 4.1. The material properties of the structures are represented by a constitutive relation that is used in the analyses. The selected material models are presented in section 4.2. The obtained width of the heat affected zone in chapter 3 is used in following analyses to determine the maximum load capacity of welded structures. The procedure for application of the residual stresses is explained in section 4.3.

4.1 Discretization

Finite element models are created using Siemens PLM's Femap as pre- and postprocessor. The structures are discretized using four-noded bilinear plate elements. The column used in the finite element analyses represents a square box section consisting of two longitudinally welded L-sections, as is used in practice. The width of the cross section is 100 mm and the material used is steel S355 grade. The exact material models used are discussed in section 4.2. At the top and bottom ends of the column RBE2 rigid elements are present that connect the end nodes of the cross section to a single node at the cross section's centroid. All degrees of freedom are transferred by the RBE2 element. A prescribed displacement boundary condition is applied at the centre top node and only translations in the cross-sectional plane are restricted (12). At the bottom all translations are constrained and in addition rotation about the longitudinal (z) axis of the column is restricted (1236) to avoid any rigid body motion. The HAZ is modelled in a similar fashion as done in chapter 3 for the test specimen: 4 elements in an L-shaped HAZ, the nodes of the two center elements are loaded with a shrinkage

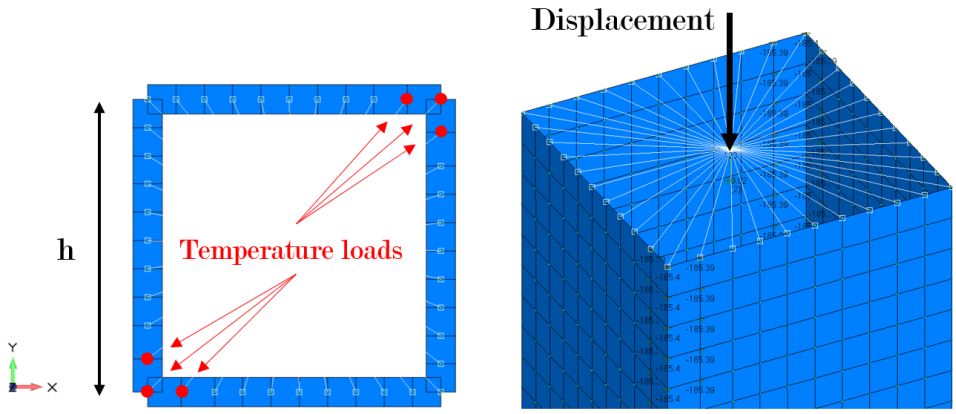

Figure 4.1: Cross section (left) and top boundary condition (right) of finite element model

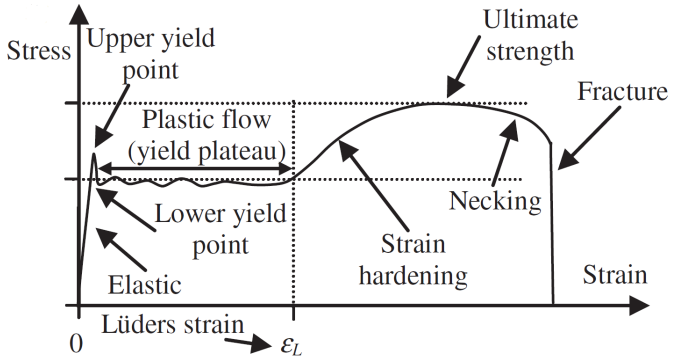

Figure 4.2: Schematic engineering stress-strain curve for typical structural carbon steel (from figure 1 [6])

temperature and the two outer elements with identical dimension are used as transition element. The model is shown in figure 4.1, together with the stresses as a result of the local shrinkage in the model.

4.2 Material model

A typical stress-strain curve for a tensile test specimen of structural steel is shown in figure 4.2. Change of the cross sectional dimensions due to the Poisson effect is not accounted for in the graph, therefore the stresses and strains are *engineering* stresses and strains. Four important regions can be distinguished from the schematic plot. The first region is the linear stress versus strain response, where the material obeys Hooke's law and the strain is fully elastic. The upper boundary of this linear region is at the yield

point, where the occurring strain is no longer totally elastic, but also plastic (irreversible) strain starts developing. For some steels even a distinction can be made between a upper- and lower yield point. After the yield point(s) the second region is characterized as the so-called "yield plateau". In this region the slope of the stress-strain curve, if any, is very small compared to the Young's modulus. The physical phenomenon causing this low stiffness is the propagation of Lüders bands through the specimen, and the strain at which the Lüders bands have traversed the full specimen is called the Lüders strain ε_L. This strain level indicates the start of the third region, where strain hardening starts developing. In this region the amount of dislocations in the crystal lattice increases significantly, thereby reducing the mobility of other traversing dislocations. This causes an increase in stiffness and therefore a finite slope in the stress-strain curve is measured. The stress level increases to a maximum value, the ultimate strength. From the strain level corresponding to the ultimate strength up to the fracture strain *necking* occurs, and the stress state in the test specimen can no longer be considered 1-dimensional and uniform. This occurs in the fourth and last region of the stress-strain curve.

Three different material models are used in the finite element models: elastic-perfectly-plastic (also referred to as elasto-plastic), elastic with linear hardening, and a modified Ludwik model. The used S355 steel grade has a yield stress of 355 MPa and an ultimate stress of 575 MPa, corresponding to a strain of $\varepsilon = 0.25$. These engineering stress and strain values are transformed to true stress and strain values according to the following formulas:

$$\varepsilon_{true} = \ln\left(1 + \varepsilon_{eng}\right) \tag{4.1}$$

$$\sigma_{true} = \sigma_{eng}\left(1 + \varepsilon_{eng}\right) \tag{4.2}$$

The *true* stress versus *true* strain curves for the used material models are shown in figure 4.3. All three models share the same linear behaviour up to the yield stress of 355 MPa, with a slope of $E = 210$ GPa. The elasto-plastic model has a hardening modulus H equal to zero, and therefore a zero slope from the onset of yielding until the failure strain. For this model the ultimate stress equals the yield stress. For the model using linear hardening and the modified Ludwik model, the true ultimate stress is equal to 719 MPa, using equation (4.2). The true strain at this stress level is $\varepsilon_{max} = 0.22$. The hardening modulus for the linear hardening model is equal to:

$$H = \frac{1}{\frac{1}{T} - \frac{1}{E}} = \frac{1}{\frac{1}{1.64 \cdot 10^9} - \frac{1}{210 \cdot 10^9}} = 1.65 \text{ GPa} \tag{4.3}$$

Where T is the tangent modulus i.e. the instantaneous slope of the true stress-strain curve.

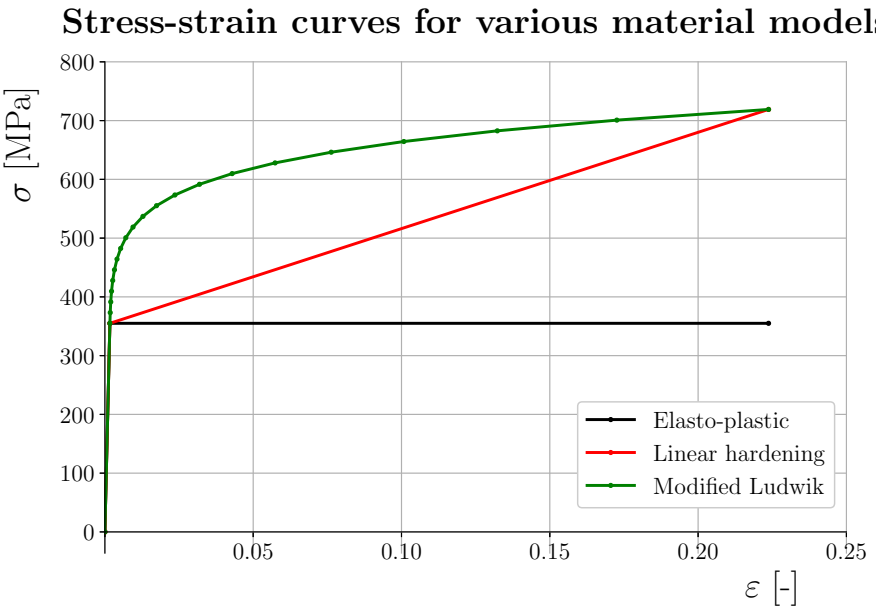

Figure 4.3: True stress-strain curves for different material models used in finite element analyses

The modified Ludwik model is based on the simple power law of Ludwik [12]:

$$\sigma_{true} = C\varepsilon^n \tag{4.4}$$

where C is a constant stress and n is the dimensionless strain hardening exponent. Because n has a value less than one, this model has an infinite slope at zero strain. Therefore the model is modified by dividing the model in two parts: one linear elastic part identical to the elasto-plastic and linear hardening models, and the second part follows Ludwik's power law. At the yield stress, the slopes of the two parts are made tangent, so that the slope of the stress-strain curve is continuous. The stress-strain relation is then defined as:

$$\sigma = \begin{cases} E\varepsilon & \text{if } \varepsilon \leq \dfrac{\sigma_y}{E} \\ \sigma_y \left(\dfrac{E\varepsilon}{n\sigma_y} - \dfrac{1-n}{n} \right)^n & \text{if } \varepsilon \geq \dfrac{\sigma_y}{E} \end{cases} \tag{4.5}$$

The value for n to be used is found by equating the bottom expression for the stress in (4.5) to the ultimate stress at $\varepsilon = \varepsilon_{max}$. This yields a value of $n = 0.098$.

4.3 Application of residual stress

The distribution of welding induced residual stresses is modelled by applying thermal shrinkage to longitudinal rows of nodes in the HAZ. These rows of nodes are shown in figure 4.1. To establish the yield stress in the HAZ by varying the shrinkage temperature applied to the nodes a modified Newton-Raphson method is used. An initial temperature $T^{i=0}$ is applied to the nodes, leading to a longitudinal stress $\sigma^{i=0}$ at mid length in each row. For each row the longitudinal stress is then approximated by a linear Taylor expansion around the new stress state $\sigma^{i=0}$:

$$\sigma = \sigma^i + \left(\frac{\partial \sigma}{\partial T}\right)_{i=0} (\Delta T)^i \tag{4.6}$$

The stress should converge to σ_y, and therefore $(\Delta T)^i$ is calculated using equation (4.6):

$$(\Delta T)^i = \frac{\sigma_y - \sigma^i}{\left(\frac{\partial \sigma}{\partial T}\right)_{i=0}} \tag{4.7}$$

The updated temperature is then:

$$T^{i+1} = T^i + (\Delta T)^i \tag{4.8}$$

Equations (4.7) and (4.8) are repeated until σ^i approximates the yield stress within a tolerance of 0.05%. The resulting longitudinal stress distribution in the column is shown in figure 4.4.

4.4 Nonlinear static analysis

In figure 4.5 a schematic load-displacement diagram is shown for a structure loaded in compression. The physical meaning of the curve's slope is the stiffness of the structure at a given location. As can be seen, there may be combinations of load and displacement where the tangent of the curve is either horizontal or vertical. These locations on the curve are referred to as limit points. In order to determine the collapse load of a structure, the (local) maximum of the load-displacement curve has to be found. This load is from now on referred to as the *failure load* of the column. Note that a column can also be considered failed when the internal stresses exceed a certain critical value, or when the deformation becomes unacceptable large. In this context however the failure load is taken as the maximum load the column structure can withstand.

Because convergence at a force limit point is hard to establish for the ordinary force-controlled Newton-Raphson algorithm, a displacement controlled algorithm is used. With this strategy the load-displacement curve in the region near the collapse load can be reconstructed.

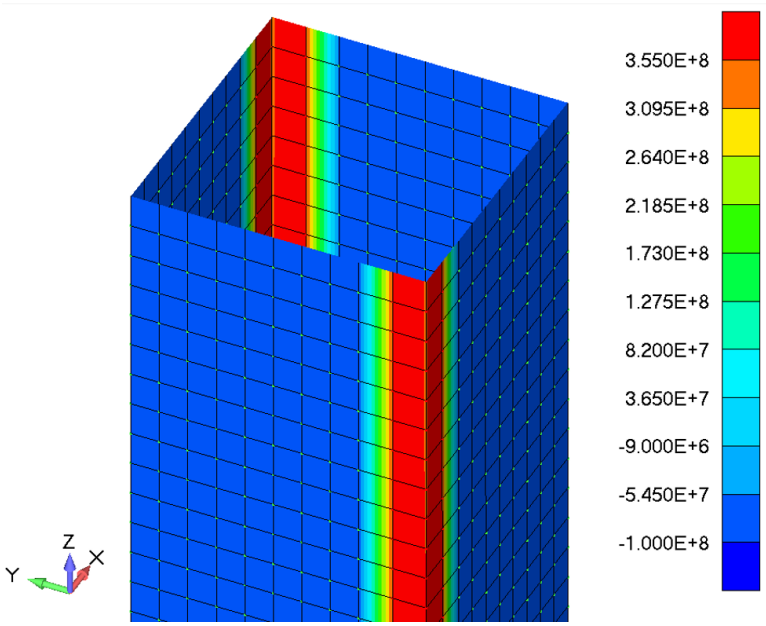

Figure 4.4: The applied thermal shrinkage in the HAZ causes a stress distribution corresponding to longitudinal welding residual stresses

The solution process in a displacement controlled nonlinear finite element analysis can best be understood by demonstrating the strategy first for a *linear* static analysis. For a linear static analysis the following system of equations is solved:

$$[\boldsymbol{K}]\{\boldsymbol{U}\} = \{\boldsymbol{F}\} \tag{4.9}$$

Here, $[\boldsymbol{K}]$ is the stiffness matrix, $\{\boldsymbol{U}\}$ is the vector with nodal displacements and $\{\boldsymbol{F}\}$ is the nodal force vector. The force vector can be rewritten in a form consisting of a residual force vector and a known force distribution multiplied by a scaling factor λ:

$$\{\boldsymbol{F}\} = \{\boldsymbol{R}\} + \lambda\{\boldsymbol{P}\} \tag{4.10}$$

The system of equation (4.9) is now split into two systems, solving for two displacement solution vectors:

$$\begin{aligned} [\boldsymbol{K}]\{\boldsymbol{U_R}\} &= \{\boldsymbol{R}\} \\ [\boldsymbol{K}]\{\boldsymbol{U_P}\} &= \{\boldsymbol{P}\} \end{aligned} \tag{4.11}$$

The solution for the displacements in the model is then:

$$[\boldsymbol{U}] = \{\boldsymbol{U_R}\} + \lambda\{\boldsymbol{U_P}\} \tag{4.12}$$

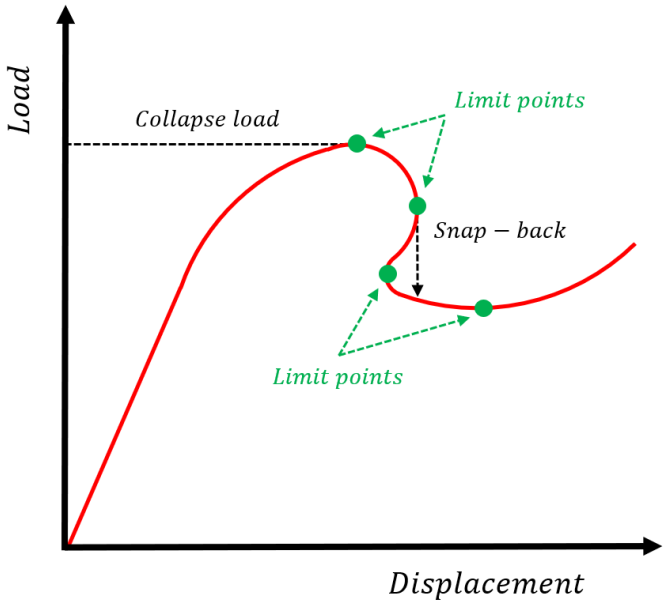

Figure 4.5: Schematic load-displacement diagram for structure under compression

For the displacement controlled analysis, the q^{th} component of the total displacement vector $\{\boldsymbol{U}\}$ is known a priori. Therefore, after solving the two systems in equation (4.11) the load factor λ can be found by stating that:

$$\left[\boldsymbol{U_R^q}\right] + \lambda \left\{\boldsymbol{U_P^q}\right\} = \{\boldsymbol{U^q}\} \tag{4.13}$$

Now the factor λ can be solved for by rewriting equation (4.13):

$$\lambda = \frac{\{\boldsymbol{U^q}\} - \left\{\boldsymbol{U_R^q}\right\}}{\left\{\boldsymbol{U_P^q}\right\}} \tag{4.14}$$

In the nonlinear analysis the enforced displacement is discretized in steps $\Delta\{\boldsymbol{U^q}\}$, and iterations are made in order to establish equilibrium between the external forces and internal forces. A difference between these quantities implies a force imbalance in the structure, and this is represented by the residue force vector. At the start of the analysis, the prescribed displacement component is updated, and for iteration $i = 0$ it is imposed that:

$$\{\boldsymbol{U}^q\}_{i=0} = \{\boldsymbol{U}^q\}_{i=0} + \Delta\{\boldsymbol{U}^q\} \tag{4.15}$$

The following systems of equations are now solved for $\Delta\{\boldsymbol{U}_R\}$ and $\Delta\{\boldsymbol{U}_R\}$:

$$\begin{aligned} \left[\boldsymbol{K}^T\right]_i \Delta\{\boldsymbol{U_R}\}_i &= \{\boldsymbol{R}\}_i \\ \left[\boldsymbol{K}^T\right]_i \Delta\{\boldsymbol{U_P}\}_i &= \{\boldsymbol{P}\} \end{aligned} \tag{4.16}$$

In above equation $\left[\boldsymbol{K}^T\right]_i$ is the tangent stiffness matrix, $\{\boldsymbol{R}\}_i$ is the force residual, both corresponding to $\{\boldsymbol{U}\}_i$. The total displacement increment $\Delta\{\boldsymbol{U}\}_i$ is equal to:

$$\Delta\{\boldsymbol{U}\}_i = \Delta\{\boldsymbol{U}_R\}_i + \Delta\{\boldsymbol{U}_P\}_i \tag{4.17}$$

During the iterations towards force equilibrium the enforced displacement is kept constant, so that:

$$\Delta\{\boldsymbol{U^q}\}_i = \Delta\{\boldsymbol{U}_R\}_i + \Delta\lambda_i\Delta\{\boldsymbol{U}_P\}_i = 0 \tag{4.18}$$

From above equation $\Delta\lambda$ can be solved for:

$$\Delta\lambda_i = -\left(\frac{\Delta\{\boldsymbol{U}_R\}}{\Delta\{\boldsymbol{U}_P\}}\right)_i \tag{4.19}$$

From where the updated displacement vector and load factor can be updated for the next iteration:

$$\begin{aligned}\{\boldsymbol{U}\}_{i+1} &= \{\boldsymbol{U}\}_i + \Delta\{\boldsymbol{U}\}_i \\ \lambda_{i+1} &= \lambda_i + \Delta\lambda_i\end{aligned} \tag{4.20}$$

Equations (4.16) till (4.19) are repeated until a convergence criterium is met, corresponding to obtaining force equilibrium in the structure. The here described algorithm was developed by Bartoz and Dhatt [13].

It should be kept in mind that another limit point can be present from a displacement-controlled point of view. The exact load-displacement curve in the region of this "snap-back" location is missed when a displacement controlled algorithm is used. Therefore, the used strategy for determining the collapse load of the structure should not be used for determining the post-buckling behaviour. Instead of either force controlled or displacement controlled algorithms, arc-length methods should be considered.

To obtain the maximum compressive load of the column, two steps are required in the analysis. At first the temperatures in the HAZ must be applied so that the yield stress is reached in the center HAZ elements. This process is done iteratively. When the yield stress is established in these elements, a displacement in downward direction is applied stepwise at the centred top node of the column. The reaction force in longitudinal direction of this node is extracted from the analysis results and plotted as function of the load step. The extreme value of the obtained curve is the maximum load of the column in compression F_{fail}.

Chapter 5

Compressive strength of perfect column

The influence of the welding induced residual stresses on the compressive strength of a single perfect column discussed in this chapter. The adjective 'perfect' suggests there are no imperfections such as loading eccentricity and initial curvature present. In reality these imperfections are never completely absent, since (con)structural dimensions can be guaranteed up to certain levels of tolerance only. The perfect column is therefore a rather utopian structural member that only exists in theory. However, to understand the failure modes of a column with realistic imperfections, it is convenient to study its failure behaviour for a perfect situation first. An introduction in the failure modes of a column loaded in compression is given in section 5.1. A description of the convergence analyses for the finite element models used is presented in section 5.2. The presence of compressive stresses in the column's cross section contributes to a reduction in the failure load. In order to determine the influence of the welding induced residual stress, failure loads of a column with residual stresses are compared with columns where these initial stresses are not present in section 5.3. In this section the used material model is elasto-plastic. The effect of material hardening is taken into account in section 5.4. As a stepping stone towards chapter 8 where a truss structure is analyzed with clamped boundary conditions, the effect of welding induced residual stresses on the collapse load of a clamped single column is analyzed in section 5.5.

5.1 Theory

When considering a perfectly straight column loaded in compression at the cross section's centroid two global failure mechanisms can already be distinguished. An example of such a column is shown in figure 5.1. The column is loaded with force F and has pinned boundary conditions at its ends. Fail-

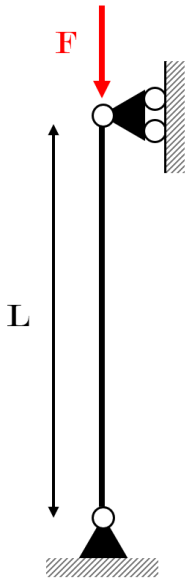

Figure 5.1: Column loaded in compression

ure may occur when the material's ultimate stress is exceeded or when the column cannot withstand an infinitesimal disturbance under compression resulting in a sudden loss of stiffness and collapse. When this happens if all normal stresses in the column remain below the elastic limit, the phenomenon is referred to as elastic buckling, and the load at which this occurs was first derived by Leonhard Euler in 1757. The critical buckling load for a column in the example is given as:

$$F_{buckling} = \frac{\pi^2 EI}{L^2} \tag{5.1}$$

where E is the material's Young's modulus, I the area moment of inertia of the cross section and L the length of the column. When equation (5.1) is divided by the column's cross sectional area A, an expression is obtained for the *stress* at which elastic buckling occurs.

$$\sigma_{buckling} = \frac{\pi^2 E}{\left(\frac{L}{\rho}\right)^2} \tag{5.2}$$

For a given material and boundary conditions, this stress is a function only of the column's *slenderness ratio* $\frac{L}{\rho}$. The symbol ρ is for the radius of gyration, defined as the squared root of the ratio of area moment of inertia to cross sectional area:

$$\rho = \sqrt{\frac{I}{A}} \tag{5.3}$$

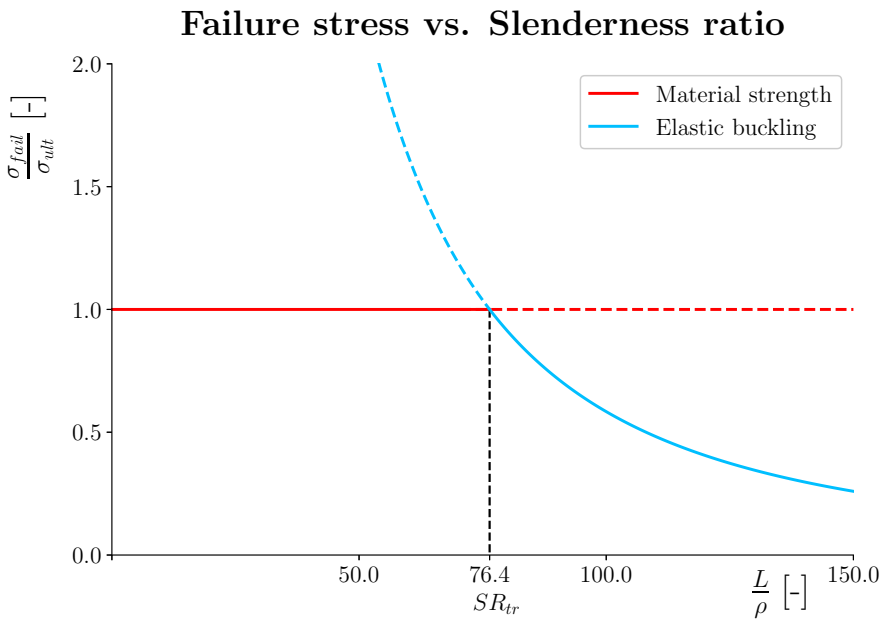

Figure 5.2: Normalized failure stress of column as function of slenderness ratio for material with $\sigma_{ult} = 355$ MPa and $E = 210$ GPa

The radius of gyration has unit length and basically transforms a particular cross section to an imaginary hollow circular cross section with the same moment of inertia and cross sectional area. In other words, when two column cross sections have the same radius of gyration and length, their critical elastic buckling load will be identical in theory for a given material.

A graphical overview of the theoretical failure stresses is shown in figure 5.2. The vertical axis represents the failure stress, which is normalized by dividing by the material's ultimate stress. On the horizontal axis the slenderness ratio is shown. The stress levels of the dotted curve sections are in practice never reached, since failure occurs already at a lower stress due to another failure mode. For a given material ultimate strength, the slenderness ratio corresponding to the intersection of the curves can be calculated by equating equation (5.2) to the ultimate stress. This slenderness ratio is referred to as the transition slenderness ratio (SR_{tr}) and is shown for a material with $\sigma_{ult} = 355$ MPa and $E = 210$ GPa and is approximately equal to 76.4.

In practice the failure stress of a column will not exactly correspond to those as shown in figure 5.2. Imperfections in geometry, load application and material properties will generally decrease the failure load and therefore the stresses shown are too optimistic. The presence of welding induced residual stresses will also contribute to a reduction in compressive strength. In upcoming sections this reduction is quantified for various loading conditions

and material hardening behaviour and a comparison is made with columns not having a residual stress distribution due to welding.

5.2 Mesh and load step convergence

The used finite element model should be able to describe the possible failure modes of the compressed column. The proper mesh size and load step for obtaining accurate results is determined by comparing the maximum compression load for a column without welding residual stresses with the theoretical results given in figure 5.2. It should be noted that failure in elastic buckling for the column shown in figure 5.1 happens in case of an arbitrarily small imperfection applied to the structure. When this imperfection is absent in the finite element model, the maximum compressive load found from the analysis is equal to the material's ultimate stress multiplied by the cross sectional area. This load is in practice never reached for columns with high slenderness ratios, and therefore an infinitesimal offset e in the point of load application with respect to the centroid of the cross section is applied. When this offset gets smaller, the theoretical result shown in figure 5.2 is approximated with greater accuracy. The failure stress as function of the slenderness ratio for a column with a load eccentricity of $e = 0.25$ mm is shown in figure 5.3. The absolute value of the deviation $|\epsilon|$ of the finite element results compared to the theoretical result for a column without offset is represented by the green curve. It can be seen that the deviation diminishes towards the smallest and largest slenderness ratios analysed, with values of 0.35% and 0.91% respectively. The used mesh consists of 10 elements over the column's width, and the number of elements over the length is set so that the HAZ elements are perfect squares. The HAZ itself is modelled by a single element loaded in tensile yield stress, and one transition element where the residual stress changes from tension to compression. This mesh was already shown in figure 4.4. The mesh independence of the finite element results are verified by refining the HAZ elements by a factor 2 and 3. These refinements resulted in a negligible deviation of 0.003% with respect to the result without refinement. This is because the HAZ is not in the region where failure of the column initiates.

The deviation of the finite element results compared to the theoretical model as function of the number of load increments is shown graphically in figure 5.4. The applied total displacement on the model is 1 cm, so an analysis with 100 load increments corresponds to a step size of 0.1 mm each increment. It can be seen that this number of load increments the deviation with the theoretical model is approximately 1.2%. Increasing the number of load increments further will only result in a slight decrease in this deviation, at the expense of a longer simulation run time. Therefore the selected load step size for the finite element analyses on the single column is 0.1 mm per

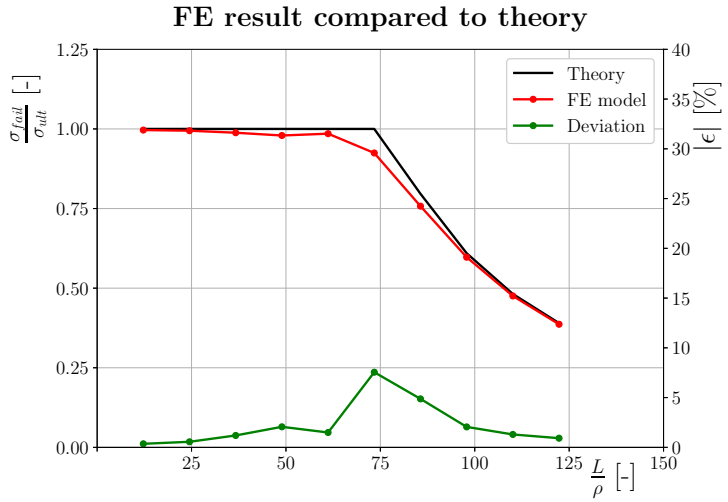

Figure 5.3: Failure stress and error for used model discretization

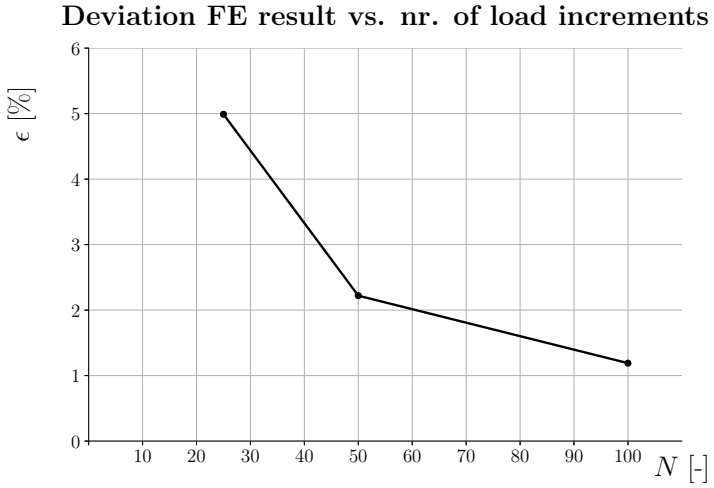

Figure 5.4: Deviation of FE results with theoretical model as function of the amount of load increments

increment.

5.3 Finite element failure load of perfect column

As already explained in subsection 5.2 the failure load in compression for a perfectly straight column without imperfections in load introduction can only be approximated by applying a very small imperfection. Failure loads are obtained by applying an offset in load introduction of 0.25 mm with

Figure 5.5: Column in buckled state

respect to the centroid of the cross section. To investigate the effect of welding residual stresses on the column's failure load, various widths of the HAZ are applied. The column in buckled state is shown in figure 5.5. In the top graph of figure 5.6 the results are shown for columns in the relevant interval of slenderness ratios. The label "1 HAZ" refers to 1 times the determined HAZ width in table 3.6 for a symmetric HAZ. The failure loads for respectively one half and one-and-a-half times this HAZ width are determined as well. For small and large slenderness ratios the effect of the welding induced residual stresses is negligible. This is explained by the fact that for small slenderness ratios the failure of the column is dominated by the material strength. For large slenderness ratios the failure mode is elastic buckling, and this is determined by the bending stiffness of the column. This bending stiffness is unaffected by the presence of residual stresses, as long as the occurring normal stresses are within the elastic range.

In the intermediate range of slenderness ratios however a significant reduction in compressive strength is present. The failure mode in this range is dominated by the occurrence of plasticity in the column's cross section. The small offset in load application causes a bending moment in the column, and the column will slightly bend prior to failure. The internal bending moment varies over the height of the column and reaches a maximum at the location with largest lateral displacement, which is at mid length. The normal stress distribution due to the bending moment is superimposed on the already present uniform normal stress due to the compressive force. The elastic limit is exceeded first on the concave side of the column. The bending stiffness is then reduced because the material in the cross section at mid length locally responds with the reduced tangent modulus E_t on increasing strain instead of the initial Young's modulus E. This decrease in bending stiffness results in the collapse of the column. It is evident that the presence

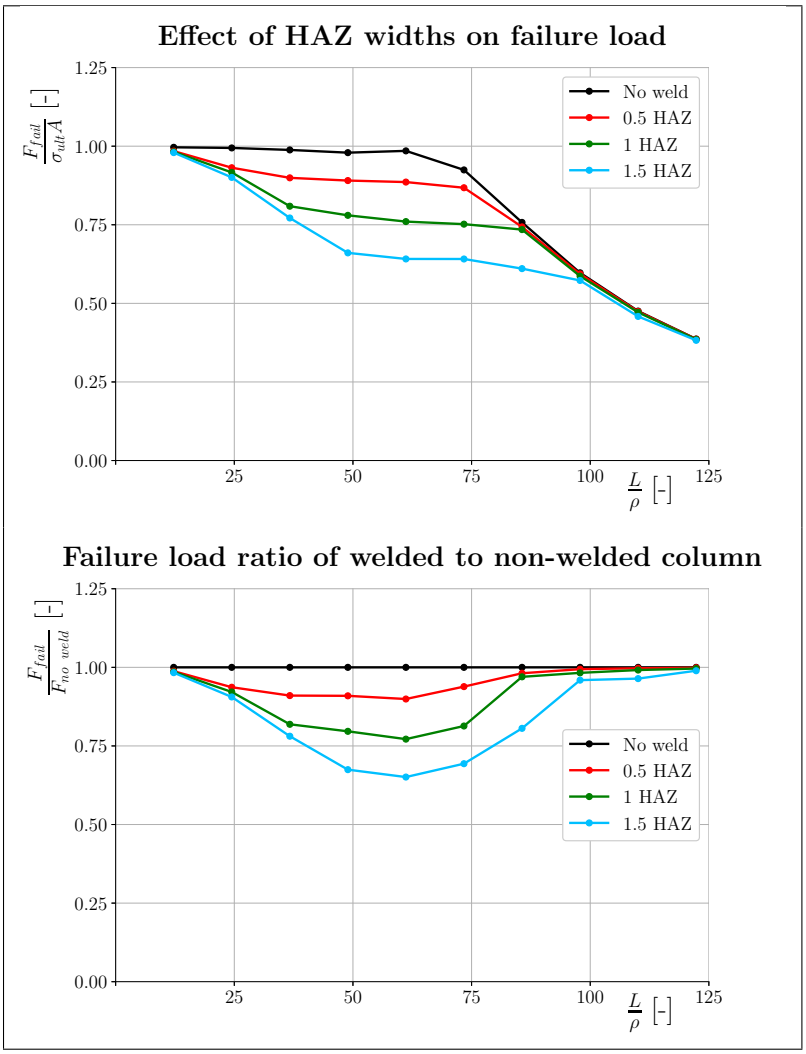

Figure 5.6: Failure loads for various HAZ widths (top) and failure load ratio of welded vs. non-welded column (bottom)

of compressive residual stresses reduces the stress margin from an unloaded state till the onset of plasticity and therefore a lower failure load for these pre-stressed columns is according to expectation.

The ratio of the failure load of columns *with* welding induced residual stresses to the failure load $F_{no\ weld}$ of a column *without* these residual stresses is shown in the bottom graph of figure 5.6. It can be seen that the reduction in maximum load capacity is larger when the width of the applied HAZ is larger. When the HAZ width b_{HAZ} is increased, so does the region with tensile residual stresses with magnitude equal to the material's yield stress. With this increasing HAZ width the region c that must balance the tensile force exerted on the HAZ gets smaller, resulting in a higher compressive

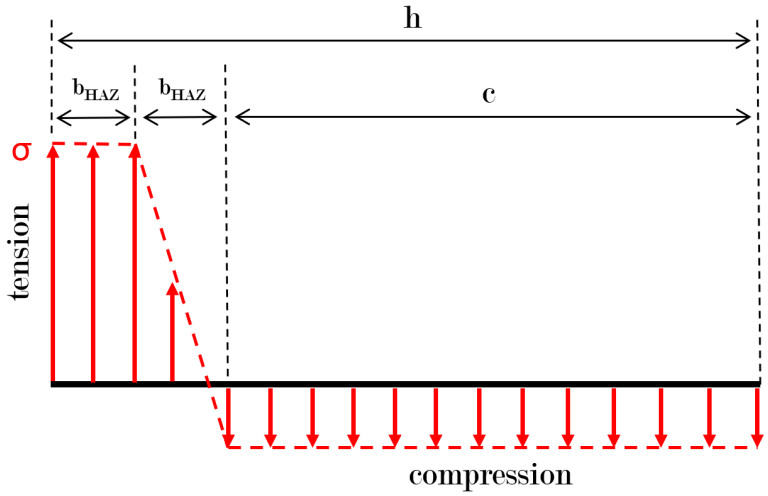

Figure 5.7: Schematic distribution of normal stress in column section

stress in absolute sense outside the HAZ. The distribution of the residual stresses in longitudinal direction for one of the four sides of the column is schematically shown in figure 5.7. It should be noted that the neighbouring side of the column's cross section must have the mirrored stress distribution as shown in the figure, due to moment equilibrium. The magnitude of the compressive residual stress σ_c is found by vertical force equilibrium:

$$+\uparrow \sum F_{vertical} = \sigma_y t b_{HAZ} + \left(\sigma_y - \frac{(\sigma_y + \sigma_c)}{2}\right) t b_{HAZ} - \sigma_c t b_{HAZ} = 0$$

Note that the compressive stress is defined positive in downward direction. Dividing by the thickness t and rearranging gives the expression for σ_c:

$$\sigma_c = \frac{3 b_{HAZ}}{2c + b_{HAZ}} \sigma_y \tag{5.4}$$

Knowing that a compressive load will superimpose a uniform compressive stress distribution over the shown residual stress distribution, the theoretical load can be calculated at which the stresses in region c are reaching the yield stress:

$$F_{yield} = (\sigma_y - \sigma_c)\, A \tag{5.5}$$

For columns with low slenderness ratio the force F_{yield} is lower than the collapse load, because after the onset of yielding in the region c the HAZs are able to carry an increasing load. For columns with high slenderness ratio F_{yield} is never reached because these will buckle elastically already at a lower load level. For columns with slenderness ratios near SR_{tr} the load F_{yield} is an upper boundary of the failure load. Due to the onset of plasticity and reduction in stiffness of the major portion of the cross section,

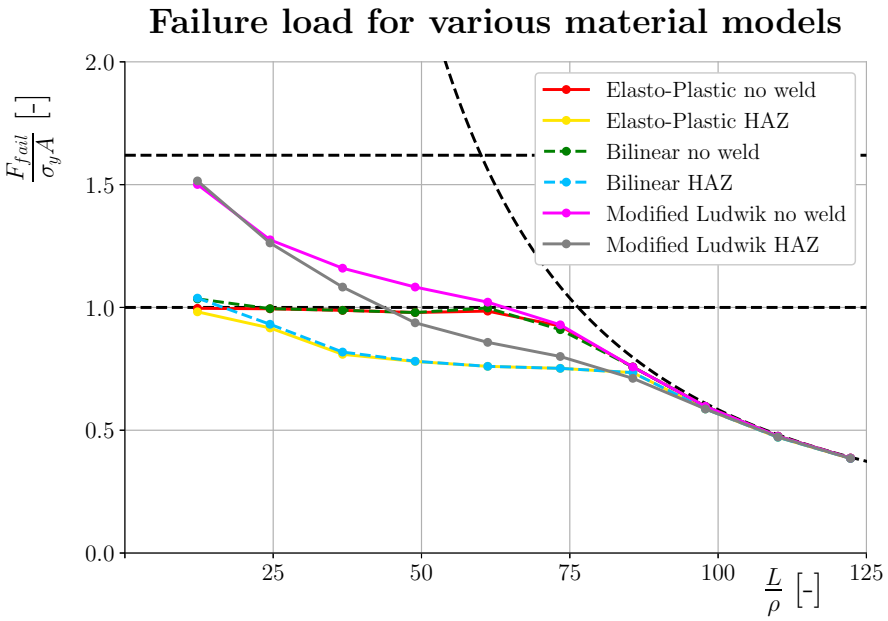

Figure 5.8: Failure loads for three material models

the remaining compressive stiffness emanates from the two HAZs. The loss of bending stiffness causes an increase in the effective slenderness of the column that leads to elastic buckling of the two HAZ portions of the cross section. Table 5.1 presents the minimum ratio of failure load for welded columns with varying HAZ widths to a non-welded column. These values correspond to the minima of the curves shown in bottom graph of figure 5.6. For comparison the ratio of F_{yield} over F_{ult} is shown, where $F_{ult} = \sigma_{ult} A$. It can be concluded that for the column considered the calculated value of F_{yield} is indeed an upper boundary of the maximum compressive load.

Table 5.1: Maximum reduction in load capacity due to residual stress

HAZ width	$\text{Min}\left(\frac{F_{fail}}{F_{no\ weld}}\right)$	$\frac{F_{yield}}{F_{ult}}$
0.5 HAZ	89.9%	90.7%
1 HAZ	77.2%	79.3%
1.5 HAZ	65.1%	65.5%

5.4 Failure load with material hardening

The failure loads for the three material models described in section 4.2 are shown in figure 5.8. In this figure the curved dotted black line shows the theoretical elastic buckling load. Two horizontal black dotted lines are present. The lower line corresponds to the failure load $F_{fail} = \sigma_y A$, and the upper line to $F_{fail} = \sigma_{ult} A$ respectively. The failure loads for the elasto-perfectly-plastic material models are shown in red and yellow for a non-welded and welded column respectively. It can be immediately seen that the failure loads for the bilinear models with linear hardening (green and blue) almost exactly matches the results of the simplified elasto-plastic model. A slight increase in load capacity can be discovered at the lower extreme slenderness ratio. However a significant increase in load capacity for a wider range of slenderness ratios can be established by using the modified Ludwik material model. The stress-strain curve for the modified Ludwik model was shown in figure 4.3. This material model has a smaller decrease in tangent modulus from the onset of yielding, and therefore the drop in bending stiffness due to local yielding is less severe. This can be seen by the fact that the pink and grey curves in figure 5.8 show a higher failure load for a given column slenderness and welding state. The decrease in failure load for a welded column compared to a non-welded column can however still be seen, but not as severe. A maximum drop of 16% in failure load is established for the modified Ludwik material model (compared to 23% for elasto-plastic model). This shows that even a longitudinally welded column consisting of a material with a gradual decrease in stiffness after yielding is still prone to a premature collapse.

The slope of the yield plateau in the used linear hardening model is 0.6% of the Young's modulus. According to Sadowksi et al. [6] a typical slope of the yield plateau in a material's stress-strain curve is approximately 0.3% of the Young's modulus. These slopes can be regarded negligible compared to the material's initial Young's modulus. It can therefore be concluded that when a yield plateau is present in the material's stress-strain curve, the failure load can be established with reasonable accuracy using an elastic-perfectly plastic material model in the finite element analyses.

5.5 Failure load for clamped column

Up till this section the effect of welding induced residual stresses are determined for single columns having pinned boundary conditions at the top and bottom. Depending on the dimension of the HAZ, a significant reduction in failure load was found for slenderness ratios roughly in the range between 15 and 90. It is expected that for a column with clamped boundary conditions at the top and bottom (no translations and rotations allowed), a different range of slenderness ratios is affected by a reduction in failure load. This is due to the fact that the Euler buckling load for a clamped column is 4 times higher than for a pinned column, as a result of the different buckling mode. The failure loads for a welded and non-welded clamped column are shown graphically in figure 5.9. The relative failure load of a welded column compared having a HAZ width equal to the found value in table 3.6 with respect to a non-welded column is shown in figure 5.10. It can be concluded that the maximum reduction in failure load of 20% is of the same order as was found for a pinned column. The affected range of slenderness ratios is indeed shifted to higher values, and is now roughly between slightly less than 50 and 200. Outside these boundaries the effect of welding residual stresses on the failure load is negligible, because the failure mode is different than plasticity induced buckling.

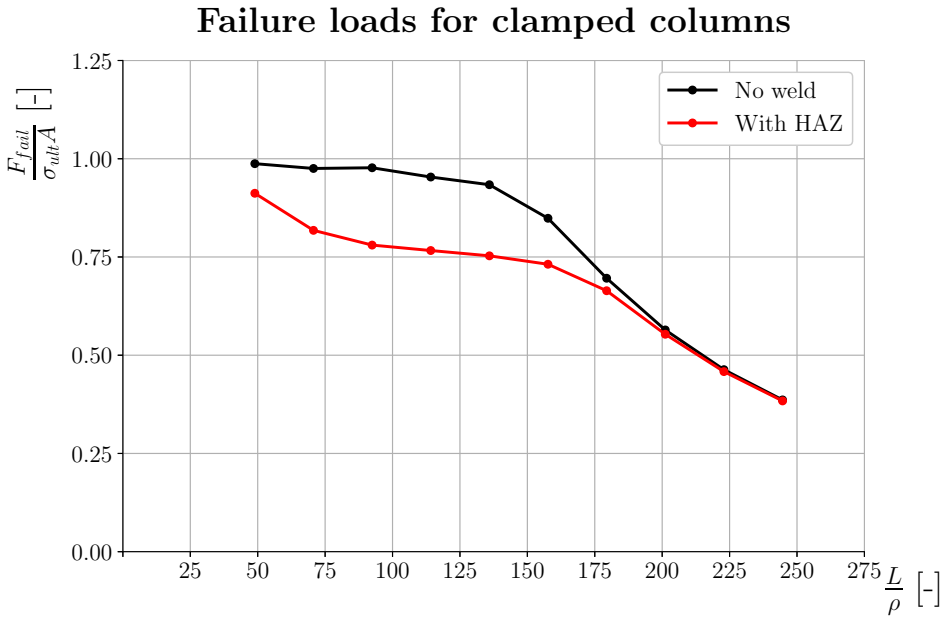

Figure 5.9: Failure loads for clamped column

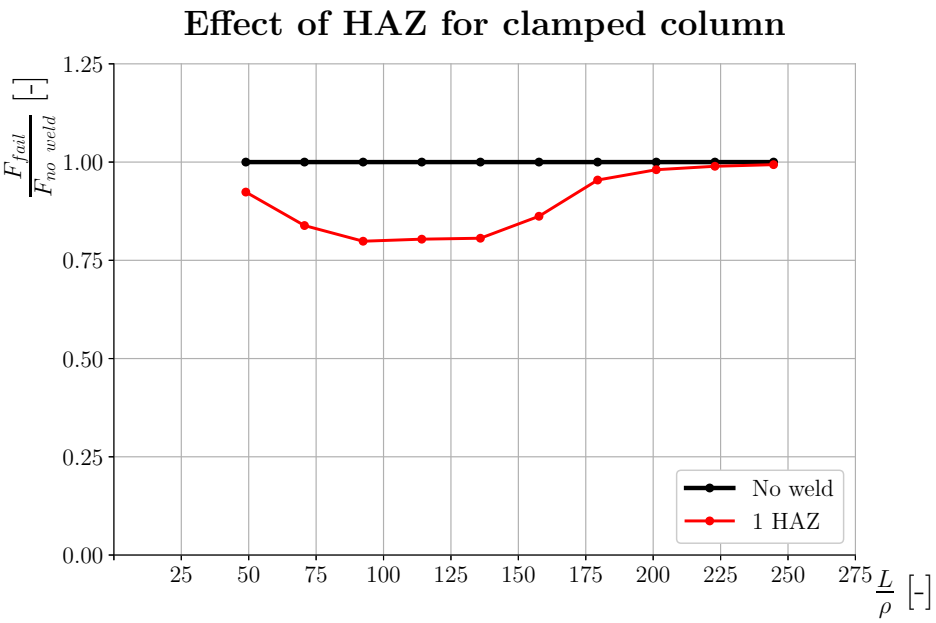

Figure 5.10: failure load ratio of welded vs. non-welded column

Chapter 6

Column with load eccentricity

In the previous chapter the effect of welding residual stresses on the collapse load for a perfect column was discussed. In the present chapter the same question is answered but now for a column compressed with an eccentric load introduction. This load case is schematically shown in figure 6.1. A theoretical background is given in section 6.1. The failure loads for a column with elasto-plastic material are presented in sections 6.2 and 6.3 for situations without and with residual stress respectively. The effect of material hardening is treated in section 6.4.

6.1 Theory

The compressive force is introduced with an offset e with respect to the cross section's centroid. This distance is exaggerated in the left image for clarity, however in the performed analyses the point of load application lies within the outer boundaries of the cross section. In the right image the same column in deformed state is shown. The x axis lies aligned with the load and the lateral displacement of the column w is defined positive to the left. An expression for the displacement w as function of the load F is derived by starting with the equation for moment equilibrium at an arbitrary location along the column. First, recall the relation between the internal bending moment and the curvature of the column for small slopes:

$$M(x) = EI\frac{d^2w}{dx^2} \tag{6.1}$$

The internal bending moment must be in equilibrium with the externally applied moment. At any location x along the column this external moment is equal to $F(w+e)$. The equilibrium condition therefore states:

$$EI\frac{d^2w}{dx^2} + F(w+e) = 0 \tag{6.2}$$

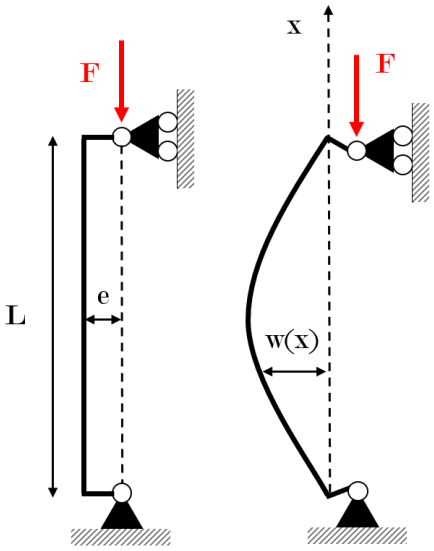

Figure 6.1: Column compressed with eccentric load introduction in initial state (left) and deformed state (right)

Rearranging in standard form for a inhomogeneous linear second order differential equation gives:

$$EI\frac{d^2w}{dx^2} + Fw = -Fe \tag{6.3}$$

The general solution for this differential equation is:

$$w(x) = C_1 \sin\left(\sqrt{\frac{F}{EI}}x\right) + C_2 \cos\left(\sqrt{\frac{F}{EI}}x\right) - e \tag{6.4}$$

The constants C_1 and C_2 are found by applying the boundary conditions $w(x) = 0$ at $x = 0$ and $\dfrac{dw}{dx} = 0$ at $x = \dfrac{L}{2}$. The particular solution is then found to be:

$$w(x) = e\tan\left(\sqrt{\frac{F}{EI}}\frac{L}{2}\right)\sin\left(\sqrt{\frac{F}{EI}}x\right) + e\cos\left(\sqrt{\frac{F}{EI}}x\right) - e \tag{6.5}$$

Recalling the critical (elastic) buckling load from equation (5.1):

$$F_{buckling} = \frac{\pi^2 EI}{L^2}$$

The expression $\sqrt{\frac{F}{EI}}\frac{L}{2}$ can be written in a more readable form:

$$\sqrt{\frac{F}{EI}}\frac{L}{2} = \sqrt{\frac{F}{EI}}\frac{L}{2}\sqrt{\frac{F_{buckling}}{F_{buckling}}} = \frac{\pi}{2}\sqrt{\frac{F}{F_{buckling}}} \tag{6.6}$$

Equation (6.5) can now be written as:

$$w(x) = e \tan\left(\frac{\pi}{2}\sqrt{\frac{F}{F_{buckling}}}\right) \sin\left(\sqrt{\frac{F}{EI}}x\right) + e\cos\left(\sqrt{\frac{F}{EI}}x\right) - e \quad (6.7)$$

It follows from the derived expression for $w(x)$ that the lateral displacement is linear dependent on the initial load eccentricity e, and that the relation between $w(x)$ and the load F is nonlinear. It should be noted that as $F = F_{buckling}$, the displacement goes to infinity. This is the condition of elastic buckling, and therefore columns with load offset e share the same elastic buckling load as for a column loaded without initial offset. The necessary condition for equation (6.7) to hold is that all normal stresses in the column remain below the elastic limit. The x location of maximum absolute stress in the column is at $x = \frac{L}{2}$, because here the lateral displacement w is maximum. The elastic stresses in the cross section at this location are calculated by superimposing the uniform compressive stress due to the force F and the linear distribution due to the bending moment:

$$\sigma_{max} = \frac{F}{A} + \frac{F\left[w\left(x = \frac{L}{2}\right) + e\right] y_{max}}{I} \quad (6.8)$$

Here y_{max} is the location in the cross section with maximum distance with respect to the neutral axis. The expression for the lateral displacement at $x = \frac{L}{2}$ is found by evaluating equation (6.5). Substitution in equation (6.8) and rearranging provides:

$$\sigma_{max} = F\left[\frac{1}{A} + \frac{e\sec\left(\frac{\pi}{2}\sqrt{\frac{F}{F_{buckling}}}\right) y_{max}}{I}\right] \quad (6.9)$$

where $\sec(\theta) = \frac{1}{\cos(\theta)}$. When the right hand side of equation (6.9) is equated to the material's yield stress σ_y, an expression for the load F for which plasticity starts developing can be obtained. This numerically obtained load is referred to as F_{yield} and is used in next subsections for comparison with the failure loads obtained by the finite element models. The used offset distance e is along the diagonal of the square cross section. The distance y_{max} is therefore equal to $\frac{1}{2}\sqrt{2}h$, where h is the width of the cross section.

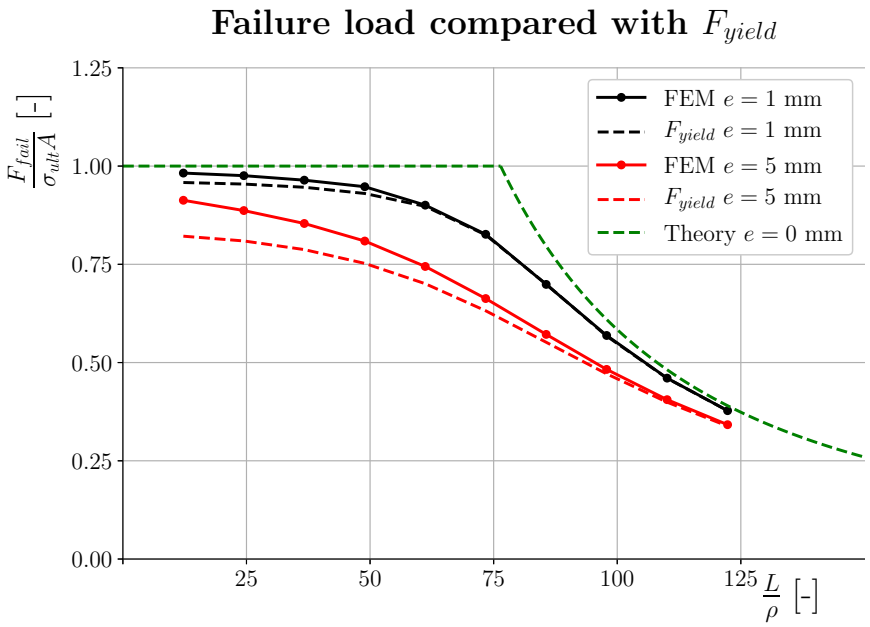

Figure 6.2: Failure stress for column compared with load where yielding starts

6.2 Column without residual stress

Even though the elastic critical buckling load for columns with load offset e is equal to a column without offset, the failure load in compression is lower for a column *with* offset. In contrast to column without load offset, the load-displacement diagram for columns with load offset lacks a bifurcation point, and a non-trivial solution for the lateral displacement is followed from the onset of loading. The sudden decrease in lateral stiffness as was present for elastic buckling of the perfect column is not occurring for columns with load offset. Instead, the lateral stiffness gradually reduces to zero.

Over the full range of slenderness ratios considered, the failure load decreases with increasing offset distance. Failure loads for values $e = 1$ mm and $e = 5$ mm are shown in figure 6.2. It can be seen that for high ratios of slenderness the failure load approximates the elastic buckling failure load. This also holds for the dotted lines corresponding to F_{yield}. However, in the intermediate and low slenderness range the columns are experiencing an increasing amount of plasticity with increasing offset distance. For a given compressive load and offset distance, the ratio $\frac{F}{F_{buckling}}$ reduces for decreasing slenderness ratios. This results in less lateral displacement according to equation (6.7), and therefore reducing the internal bending moment. This reduced moment increases the load capacity of the column, resulting in a failure load increasingly higher than F_{yield} for decreasing slenderness.

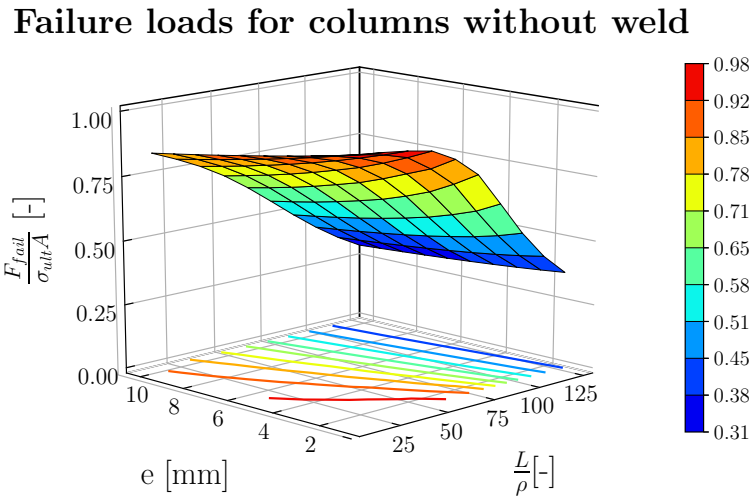

Figure 6.3: Failure stress for single column without residual stress

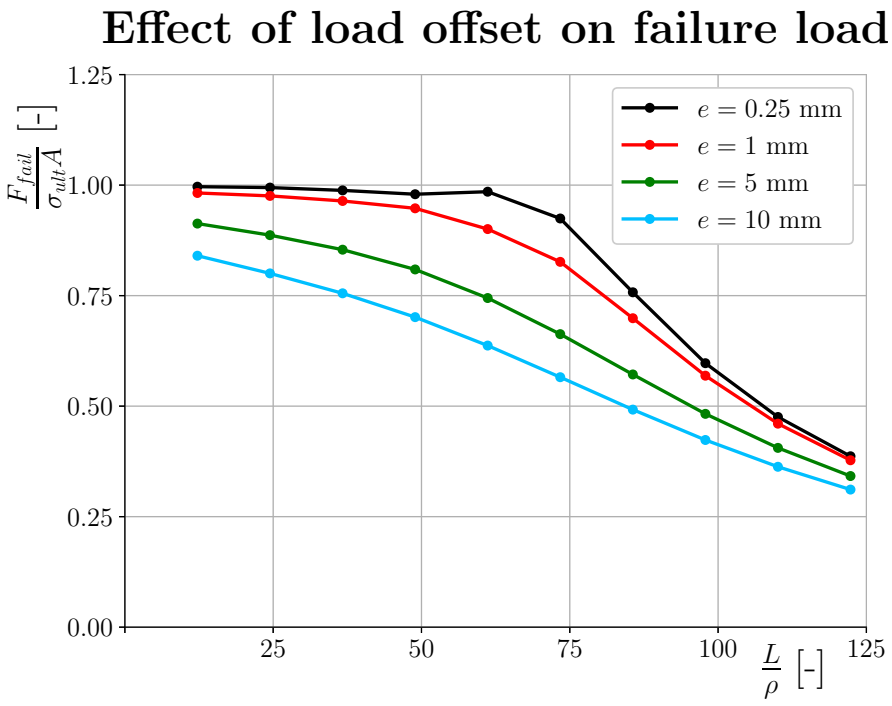

Figure 6.4: Effect of load offset for single column without residual stress

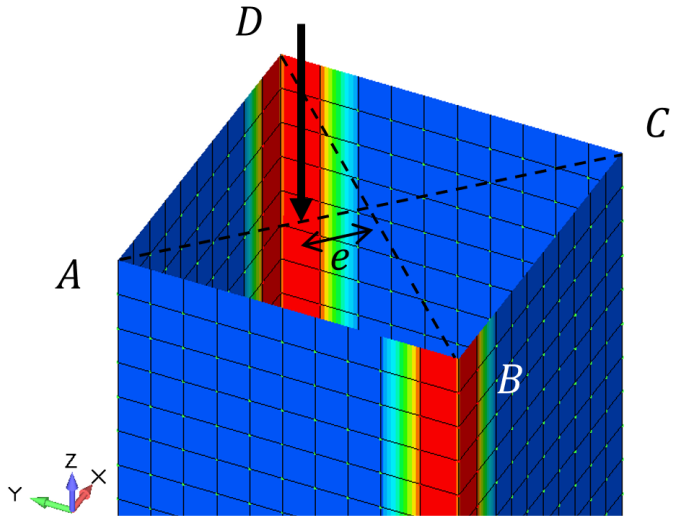

Figure 6.5: Direction of offset distance e is towards corner with compressive residual stresses

The effect of the offset distance e on the failure load is graphically shown in figure 6.3. The isolines of the 3D surface are projected on the bottom plane of the image. It can be seen that for high ratios of slenderness the isolines are tending to be parallel with the e-axis. This indeed confirms that the collapse load is not significantly influenced by the load offset for these ratios of slenderness. This trend does not hold for low slenderness ratios, as can be seen by the varying orientation of the isolines. Furthermore it can be clearly seen that the distance between the isolines crossing the plane at $e = 10$ is larger than for the plane at $e = 1$. This means that the decrease in failure load for higher ratios of slenderness is less severe at high values of offset. This is explained by the fact that the external bending moment $F(w + e)$ has a more and more dominant effect on the failure behaviour compared to the compressive force F. This effect is also visualized by making sections of the graph at various offset distances are shown in figure 6.4.

6.3 Column with residual stress

The direction of the loading offset distance e is shown in figure 6.5. This distance is measured from the cross section's centroid along the diagonal AC. In this way the induced bending moment causes an early onset of yielding in corner A, where compressive residual stresses are acting. The failure load for welded columns with offset $e = 1$ mm and $e = 5$ mm is shown in figure 6.6. The used HAZ width corresponds to the found value for the welded L-profile with symmetric HAZ in chapter 3. The failure loads are compared

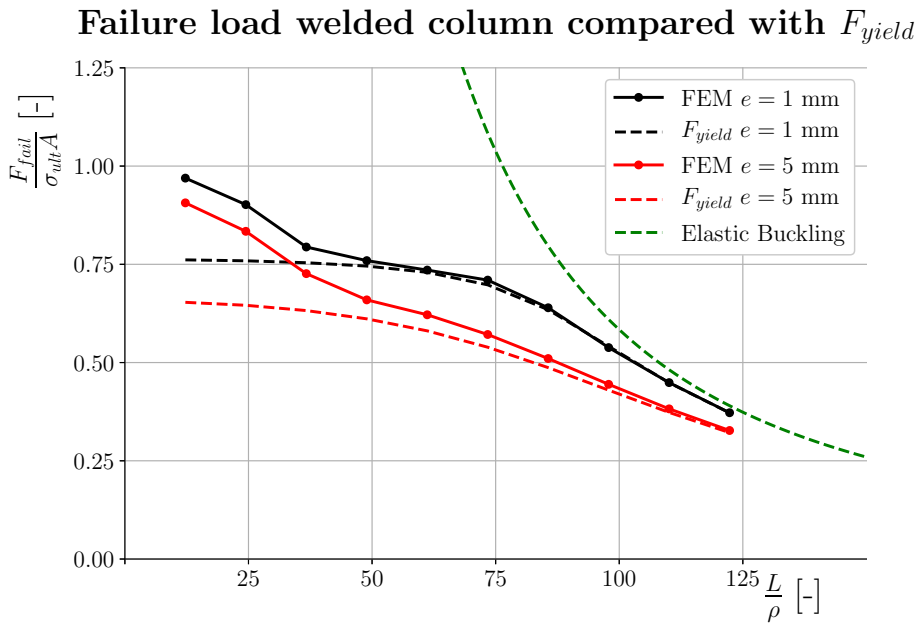

Figure 6.6: Failure load for column with HAZ compared with load where yielding starts

with the load F_{yield} where yielding in the cross section starts developing. This load is calculated by subtracting the compressive residual stress from the left hand side of equation (6.9) and solving numerically for F:

$$\sigma_y - \sigma_c = F \left[\frac{1}{A} + \frac{e \sec\left(\frac{\pi}{2} \sqrt{\frac{F}{F_{buckling}}} \right) y_{max}}{I} \right] \tag{6.10}$$

where σ_c is calculated using equation (5.4). It can be seen that also for a welded column both the failure load obtained from the finite element analyses and the manually obtained F_{yield} approximate the failure load corresponding to elastic buckling for high ratios of slenderness. For slenderness ratios $\frac{L}{\rho} > 50$ in the shown figure, the failure load is reasonably predicted by F_{yield}. For slenderness ratios lower than this value the actual failure load shows a significant deviation from the conservative F_{yield}. These stocky columns are less prone to instability, even after a relatively large portion of the cross section has lost its compressive stiffness. The compressive residual stresses on the convex side of these columns cause an increase in stress capacity before yielding in tension can occur. This effect postpones the loss of stiffness in tension and results in a higher load capacity.

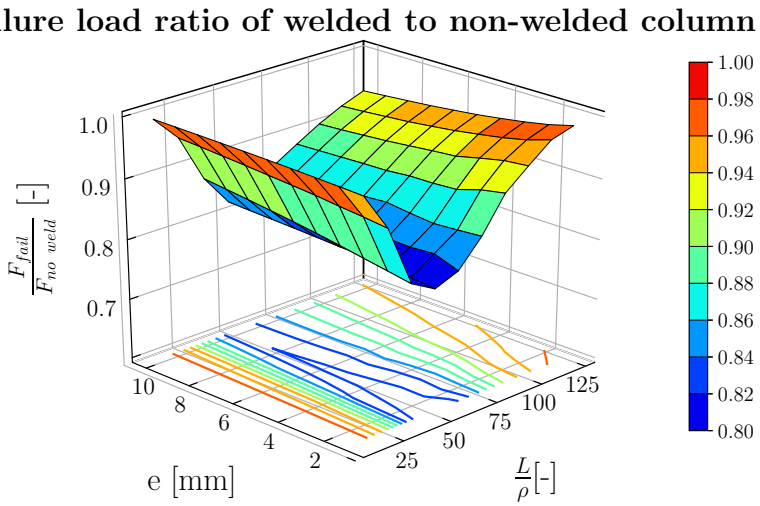

Figure 6.7: Ratio of compressive strength of column with and without residual stress

The ratio of the failure load for a column with weld to a column without weld is shown graphically in figure 6.7 for offset values ranging from $e = 1$ to $e = 10$. As can be derived from the isolines projected on the bottom plane of the image, no reduction in failure load is found for the lowest extreme slenderness ratio for the entire range of offset values. The negative effect of compressive residual stresses on the early onset of yielding on the concave side is counteracted by the increased capacity in tension on the convex side.

It is interesting to derive from the isolines in figure 6.7 that the largest reduction in failure load due to the weld occurs for the smallest offset distance e. The depth of the "trough" at the intermediate slenderness ratios slightly decreases with increasing offset distance. The failure of columns in this intermediate range is preceded by local yielding at the concave side of the cross section. As explained, increasing the offset distance increases the bending moment in the column. This increased bending moment causes a higher maximum stress in absolute sense in the cross section. It makes sense that with higher bending induced stresses the relative impact of the already present residual stresses is smaller.

Sections of the graph in figure 6.7 along the lines $e = 1$ mm and $e = 5$ mm are shown in figure 6.8. The ratios of failure load compared to a column without weld are shown for three HAZ widths. As expected the reduction in failure load increases for increasing widths of the heat affected zone. Comparing the top graph with the bottom graph, it can be seen that the re-

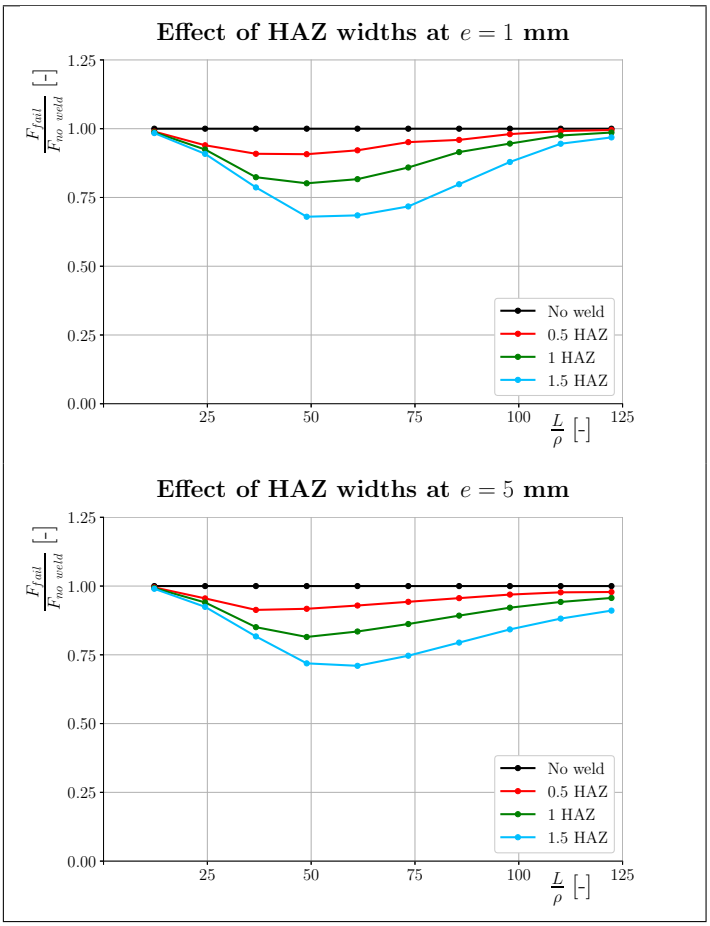

Figure 6.8: Effect of various HAZ widths at $e = 1$ mm and $e = 5$ mm

duction in collapse load due to the welding induced residual stresses indeed becomes less severe for increasing offset distance. This effect is present at all the considered HAZ widths, however it is more noticeable for larger HAZ widths.

Another effect that can be clearly seen from figure 6.8, is that for increasing offset distance, a wider range of slenderness ratios is affected by a reduction in failure load. This effect was already predicted by equations (6.9) and (6.10). It was shown that for high ratios of slenderness the failure load is equal to F_{yield}. When equation (6.10) is compared to equation (6.9), it can be seen that the left hand side of equation (6.10) is reduced in magnitude. For a given slenderness ratio the right hand sides of these two formulas are equal in magnitude, except for the load F. Therefore, a lower failure load $F = F_{yield}$ is expected for all ratios of slenderness when welding induced residual stresses are present.

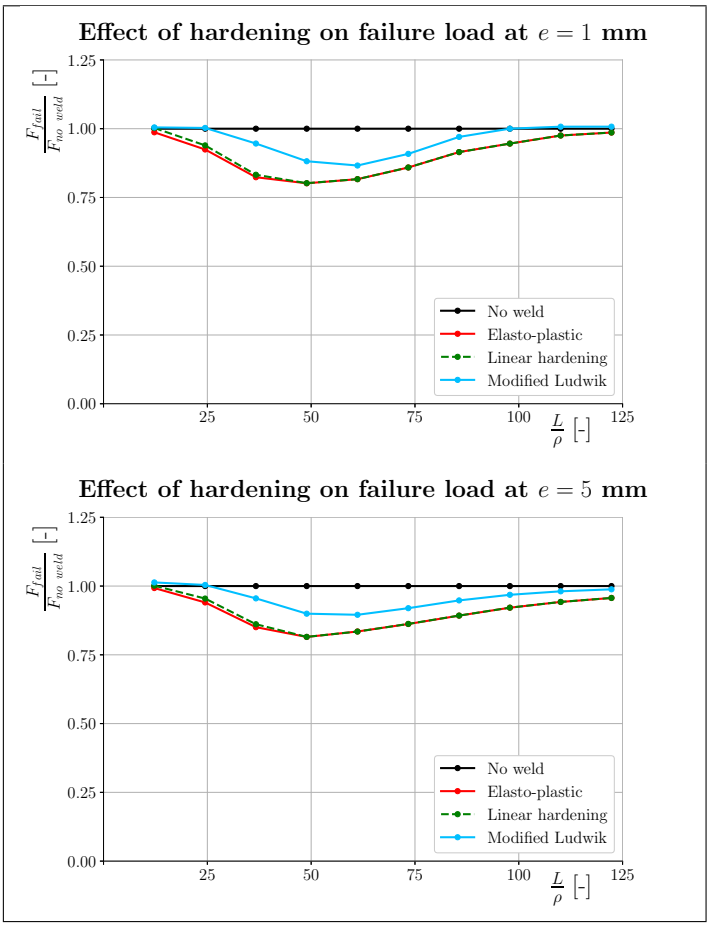

Figure 6.9: Effect of various material models for HAZ width 1 HAZ at $e = 1$ mm and $e = 5$ mm

6.4 Failure load with material hardening

The effect of strain hardening on the failure load is shown in figure 6.9. The failure load ratios are shown for columns with a HAZ width corresponding to the HAZ width in table 3.6 for a symmetric HAZ. A negligible difference in the effect of residual stresses can be observed between the elasto-plastic and linear hardening material model. Columns made from these materials respond the same to the presence of a longitudinal weld. This was also concluded for a column without imperfections in section 5.4. Materials with a more gradual decrease in Young's modulus from the onset of yielding have a higher bending stiffness when yielding occurs, and are therefore more stable than columns where the majority of the stiffness is lost in the zone where the stress is higher than the yield stress. This makes the column less prone to an early onset of yielding due to welding induced residual stresses.

Chapter 7

Column with initial curvature

In the present chapter the compressive failure load is determined for a column with an initial curvature. This load case is schematically shown in figure 7.1, where $w_0(x)$ is the function that describes the initial shape. Columns used in structures are never perfectly straight and can have various shapes. For the column considered with two longitudinal welded L-profiles, a resulting curvature arises when the welds are not placed simultaneously and as a result the distortion due to the shrinkage after welding is not identical for each weld. Unfortunately the curvature 'helps' to collapse the column in its critical buckling mode. A theoretical background for obtaining the buckling load for a column with initial curvature is given in section 7.1. The failure loads for a column with elastic-perfectly plastic material are presented in sections 7.2 and 7.3 for situations without and with residual stress respectively. A comparison between the results for a column with an initial curvature and for a column having an initial load offset is made in section 7.4.

7.1 Theory

The elastic behaviour for columns with an initial curvature without residual stresses can be derived from the principle of minimum total potential energy. When a configuration of a structure is found under a given loading condition that minimizes the total potential energy, the equilibrium conditions are satisfied. The total potential energy Π of a structure is defined as:

$$\Pi = U - W \tag{7.1}$$

where U is the strain energy and W is the externally applied work for a conservative force. It can be derived that the potential energy for a column *without* initial curvature is:

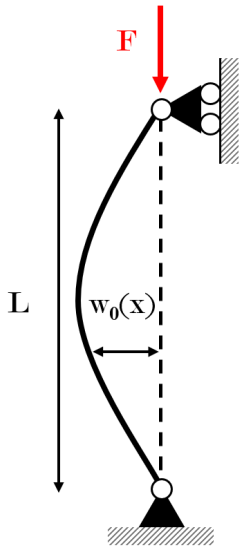

Figure 7.1: Column with initial curvature $w_0(x)$ compressed by load F

$$\Pi = \frac{EA}{2}\int_0^L \left[\frac{du}{dx} + \frac{1}{2}\left(\frac{dw}{dx}\right)^2\right]^2 dx + \frac{EI}{2}\int_0^L \left(\frac{d^2w}{dx^2}\right)^2 dx + F\int_0^L \frac{du}{dx}dx \quad (7.2)$$

where u is the axial displacement in the column. For determination of the critical buckling load the axial strain $\frac{du}{dx}$ due to the compression is equal to the stretching due to the bending $\frac{1}{2}\left(\frac{dw}{dx}\right)^2$ but with opposite sign. Therefore the potential energy expression for a perfect column can be reduced to:

$$\Pi = \frac{EI}{2}\int_0^L \left(\frac{d^2w}{dx^2}\right)^2 dx - \frac{F}{2}\int_0^L \left(\frac{dw}{dx}\right)^2 dx \quad (7.3)$$

The strain energy for a column with an initial shape $w_0(x)$ can be found by using the difference between the deformed shape and the initial shape:

$$U = \frac{EI}{2}\int_0^L \left[\frac{d^2}{dx^2}(w - w_0)\right]^2 dx \quad (7.4)$$

The vertical shortening δ along the x-axis is the difference of the displacement at the deformed state and the initial state:

$$\delta = \frac{1}{2}\int_0^L \left(\frac{dw}{dx}\right)^2 dx - \frac{1}{2}\int_0^L \left(\frac{dw_0}{dx}\right)^2 dx \quad (7.5)$$

The total potential energy for a column with initial shape w_0 can now be written as:

$$\Pi = \frac{EI}{2}\int_0^L \left[\frac{d^2}{dx^2}(w - w_0)\right]^2 dx - \frac{F}{2}\int_0^L \left[\left(\frac{dw}{dx}\right)^2 - \left(\frac{dw_0}{dx}\right)^2\right] dx \quad (7.6)$$

Using the Ritz method, the displacement function $w(x)$ can be approximated by a trigonometric series with undetermined coefficients b_n:

$$w(x) = \sum_{n=1}^{\infty} b_n \sin\left(\frac{n\pi x}{L}\right) \quad (7.7)$$

It can be seen that the expression for the deformed shape in equation (7.7) satisfies the boundary conditions for zero displacements at the pinned column's ends, shown in figure 7.1. The initial state of the displacement $w_0(x)$ can also be written as a trigonometric series with coefficients a_n:

$$w_0(x) = a_n \sin\left(\frac{\pi x}{L}\right) \quad (7.8)$$

where a physically represents the amount of initial deflection at $x = \frac{L}{2}$, and is known a priori in this analysis. Substituting equations (7.7) and 7.8 in equation 7.6 results in an expression for the total potential energy as function of the unknown coefficients b_n:

$$\begin{aligned}\Pi = {} & \frac{EI}{2}\int_0^L \left[\sum_{n=1}^{\infty}(a_n - b_n)\left(\frac{n\pi}{L}\right)^2 \sin\left(\frac{n\pi x}{L}\right)\right]^2 dx \\ & - \frac{F}{2}\int_0^L \left\{\left[\sum_{n=1}^{\infty} b_n \frac{n\pi}{L}\cos\left(\frac{n\pi x}{L}\right)\right]^2 - \left[\sum_{n=1}^{\infty} a_n \frac{n\pi}{L}\cos\left(\frac{n\pi x}{L}\right)\right]^2\right\} dx \quad (7.9)\end{aligned}$$

The minimum total potential energy is now found by stating that $\frac{d\Pi}{db_m} = 0$ for $m = 1, 2, \ldots$ Hence:

$$\begin{aligned}& -\frac{EI}{2}\int_0^L \frac{2\pi^2}{L^2}\left[\sum_{n=1}^{\infty} n^2 (a_n - b_n)\sin\left(\frac{n\pi x}{L}\right)\right]\left[\left(\frac{m\pi}{L}\right)^2 \sin\left(\frac{m\pi x}{L}\right)\right] dx \\ & \quad - \frac{F}{2}\int_0^L 2\left[\sum_{n=1}^{\infty} b_n \frac{n\pi}{L}\cos\left(\frac{n\pi x}{L}\right)\right]\left[\frac{m\pi}{L}\cos\left(\frac{m\pi x}{L}\right)\right] dx = 0 \quad (7.10)\end{aligned}$$

Due to orthogonality, the integral of the following product is zero, except when $n = m$:

$$\int_0^L \sin\left(\frac{n\pi x}{L}\right)\sin\left(\frac{m\pi x}{L}\right) dx = 0 \quad \text{if} \quad n \neq m \quad (7.11)$$

Using this property, equation (7.10) reduces to:

$$EI\frac{\pi^4 m^4}{L^4}(a_m - b_m) + \frac{Fm^2\pi^2}{L^2}b_m = 0 \tag{7.12}$$

Solving for b_m now results in:

$$b_m = \frac{a_m}{1 - \dfrac{FL^2}{\pi^2 m^2 EI}} = \frac{a_m}{1 - \dfrac{F}{m^2 F_{buckling}}} \tag{7.13}$$

Recalling equation (7.7), the horizontal displacement can now be written as:

$$w(x) = \sum_{n=1}^{\infty} \frac{a_n}{1 - \dfrac{F}{n^2 F_{buckling}}} \sin\left(\frac{n\pi x}{L}\right) \tag{7.14}$$

From equation (7.14) it can be seen that a non-trivial solution for the lateral displacement is present for at any applied load F. When this applied load approaches the buckling load for a perfect straight column, the amplitude of the sine in equation (7.14) grows without bound. At load levels this high the given equation is no longer valid due to violation of the assumption of having small rotations in the column, and the presence of plastic zones. The collapse load will therefore always be lower than the critical buckling load of a perfect column ($F_{buckling}$)

Because the critical buckling shape for a perfect column is a half wave sine function, a worst case initial imperfection $w_0(x)$ would be a half sine wave. The used imperfection shape in this chapter is therefore the expression in equation (7.8).

7.2 Column without residual stress

The failure load versus slenderness ratio is plotted in figure 7.2 for various values of the offset distance w_0. The larger this distance, the larger the initial curvature of the column. As expected, the failure load reduces for increasing initial curvature. This trend is similar compared to the column with initial load offset e as treated in section 6.2.

Referring back to the found curvatures in the welded specimen in table 3.4, the established radii of curvatures lie roughly in the range between 50m and 600m. To obtain the initial offset at mid length w_0 based on a given radius of curvature R the following formula can be used:

$$w_0 = R\left[1 - \cos\left(\arcsin\left(\frac{L}{2R}\right)\right)\right] \tag{7.15}$$

Here L is the length of the column. Note that for some specimen presented in chapter 3 the established radius of curvature was a component of the

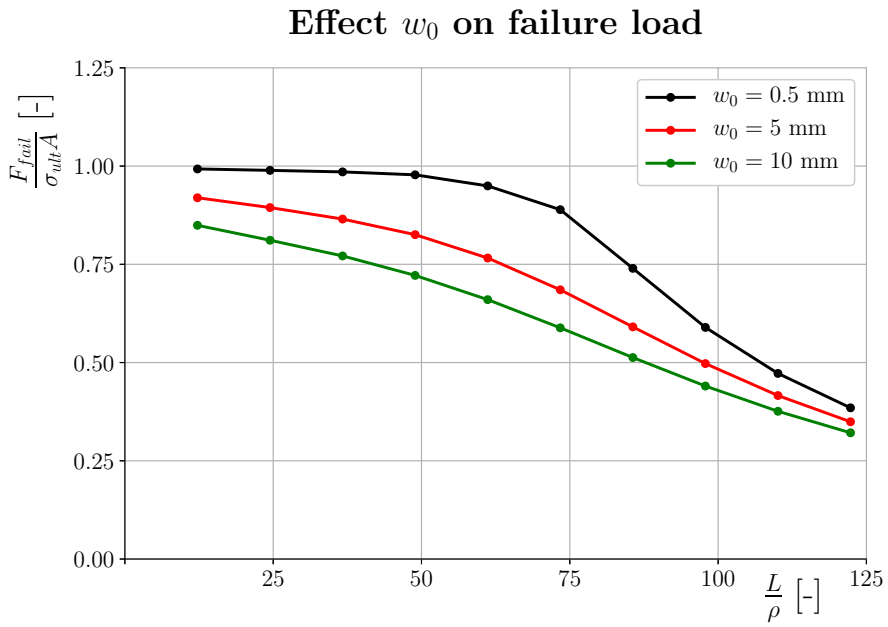

Figure 7.2: Failure load versus slenderness ratio for various initial curvatures

total occurring curvature. Based on the experiments it can be shown that the welding deformation under the used circumstances caused an initial curvature at mid length in the order of millimeters. Therefore the range of investigated values for w_0 is limited to small values compared to the length of the column.

7.3 Column with residual stress

For a given value of $w_0 = 1$ mm, both the failure load versus slenderness ratio and the relative effect of the welding residual stresses are plotted in figure 7.3 for multiple values of the HAZ width. The occurring effects are similar compared to the column with initial load offset e as treated in section 6.3. When the failure load is determined for various values of w_0, the same effects are recognized as for the column with initial load offset:

1. The presence of welding induced residual stress has no effect for all values of w_0 for low slenderness ratios
2. The maximum amount of reduction of the failure load decreases slightly for increasing values of w_0
3. The amount of reduction in failure load for high slenderness ratios slightly increases for increasing values of w_0

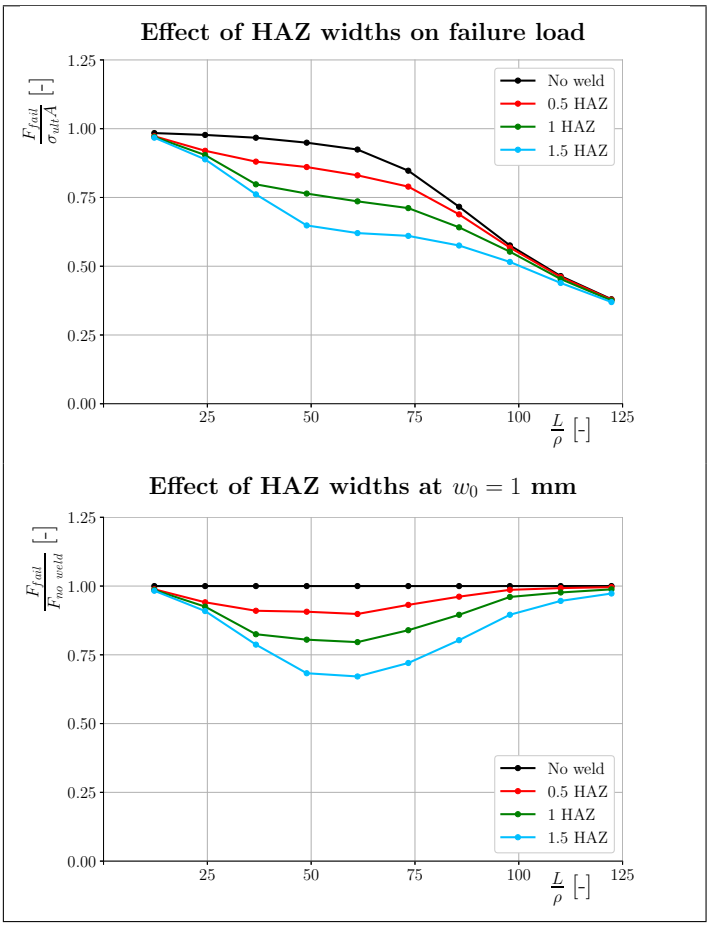

Figure 7.3: Effect of various HAZ widths at $w_0 = 1$ mm

7.4 Comparison between two types of imperfections

For investigating the effect of welding induced residual stresses two types of imperfection were considered: an initial load offset and an initial curvature on the column. It was shown that both conditions react similar to the presence of a given HAZ width. In figure 7.4 a comparison of failure load results is shown for a column with an initial load offset of $e = 10$ mm and $w_0 = 10$mm. The top graph shows the failure load for both imperfections, and both for a non-welded and welded column. It can be seen that the failure load for the column with initial curvature is slightly higher. For the given amount of imperfection the columns with initial curvature (both welded and non-welded) have an approximate 3% higher failure load relative to the columns with initial load offset. Because the bending moments in the columns are different for the two considered imperfections, a difference

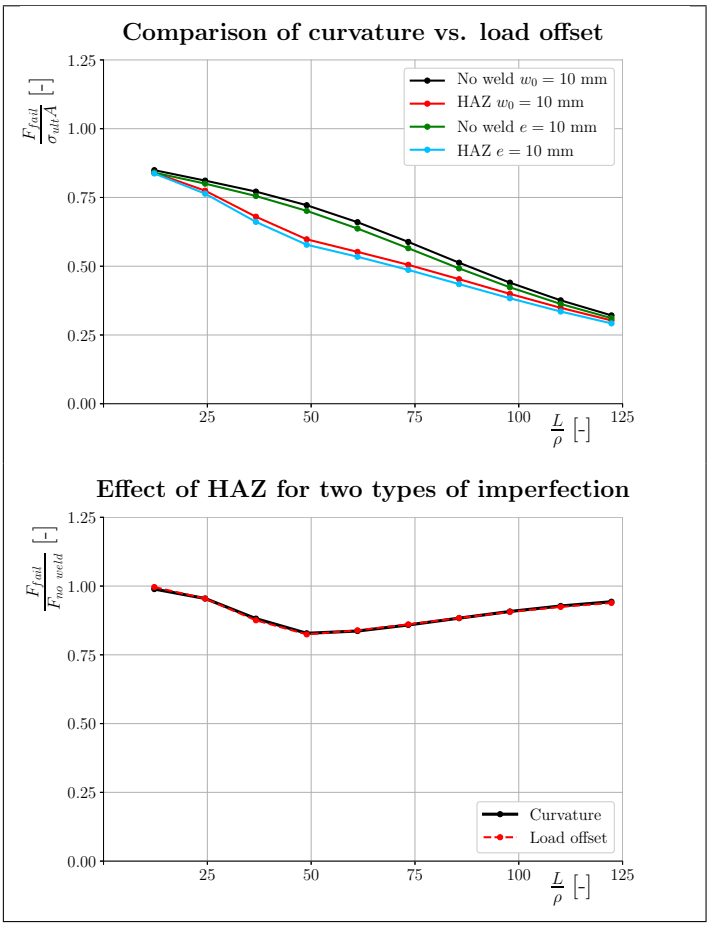

Figure 7.4: Comparison of reduction in failure load for two types of imperfections

in failure load is according to expectation. The difference diminishes for decreasing amount of imperfection, since the column then approximates a perfect straight column.

The bottom graph in figure 7.4 shows the relative failure load for a welded versus a non-welded column for the two imperfection types. Both curves coincide, and this effect was also present for different values of imperfection magnitude. Therefore it can be concluded that the presence of the simulated welding residual stresses have the same effect on a column with the considered imperfections.

Chapter 8

Compressive strength of truss structure

To study the effect of welding induced residual stresses on the compressive load capacity of a truss structure, a typical section of a crane structure is modelled. This section is referred to as a tower crane element, and represents one repetitive unit of the vertical structure of a tower crane. The used finite element model is described in section 8.1. Various loading configurations are analyzed, these are presented in section 8.2. The results are presented in section 8.3.

8.1 Finite element model

The finite element model of a tower crane element is shown in figure 8.1. It consists of four columns positioned in a square layout with respect to each other. These columns are meshed with linear plate elements. The columns are interconnected by side bars with small cross sectional area compared to the vertical columns and are modelled as two-force members (rod elements). These rod elements are placed with an angle of 30° with respect to the horizontal. The end nodes of these rod elements are placed in the centroid of the square cross section of the columns, and rigidly connected with a RBE2 element to the circumferential nodes of the column cross section. This detail is also shown enlarged in figure 8.1.

Typically, crane sections are interconnected to neighbouring crane sections allowing no translations and rotations. Therefore a fully clamped boundary condition is applied at the bottom of the four columns (see figure 8.1). The top nodes of the crane section are rigidly connected to a node at a certain offset e with respect to the crane section's center (see figure 8.2). This offset distance is varied in the finite element analyses performed. A downward displacement is applied at this node and the reaction force at this node is read for each displacement step. In this way a load-displacement

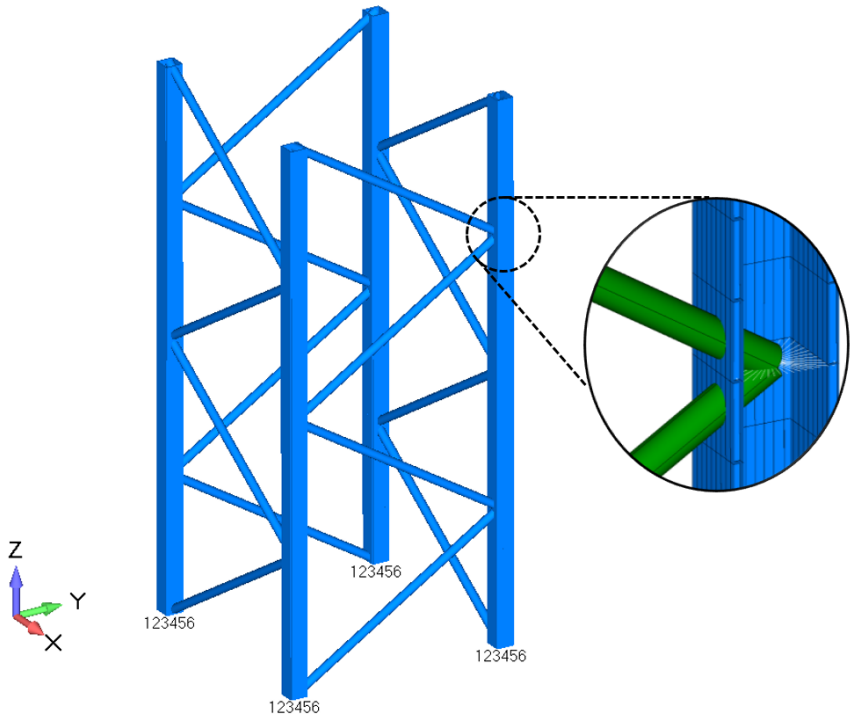

Figure 8.1: Finite element model of typical crane section

curve is obtained for a particular load case. The extreme value of this curve is considered as the collapse load of the crane section. The longitudinal welds in the four columns are modelled by applying a shrinkage temperature load at the weld location, as was done in previous chapters. A mesh convergence analysis has been performed to allow for mesh independent results, as well as for the displacement increment. The HAZ of the columns is again meshed as one element loaded in tensile yield stress, and one element where a transition in stress is present from tensile yield stress to the equilibrating compressive stresses in the remaining cross section. This is the same methodology as for a single column in previous chapters. Each column consists of 40 elements over its full length, thus having 20 elements between the connections with the side bars.

8.2 Structures analysed

The dimensions of the crane element are based on scaled down realistic dimensions of an existing tower crane, so that columns with identical cross sectional dimensions as in previous chapters are used for the vertical crane columns. This allows for a comparison between the results for the here studied crane element and the earlier found results for a single column. The

down scaling is performed in a way that the slenderness ratio $\frac{L}{\rho}$ for the full column length studied here is equal to the slenderness ratio found for the columns in the realistic crane element. This scaling results in a full length of the crane element model of 3.26 m, and a separation distance of 1.32 m. The cross sectional area of the rod elements are scaled down by the same factor as was applied for the columns. A top view of the crane section is schematically shown in figure 8.3. Two types of analyses are performed: one crane structure *without* longitudinal weld in the four columns, and one crane structure *with* weld. The applied HAZ width is based on the earlier found value in section 3.4. The slewing angle α at which the displacement

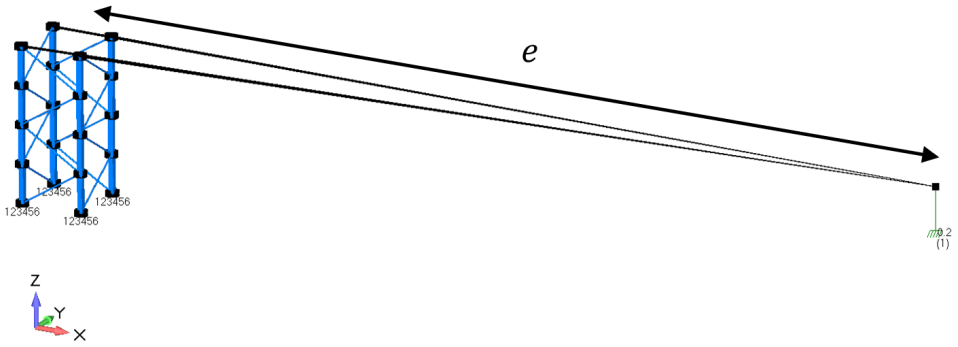

Figure 8.2: Finite element model of crane section with node where displacement is applied

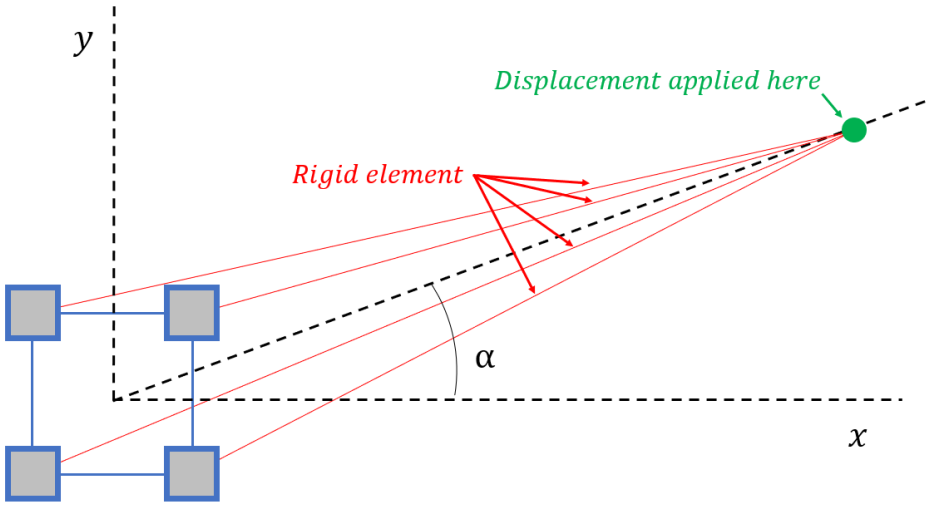

Figure 8.3: Schematic top view of crane section with node where displacement is applied

is applied with respect to the x-axis in figure 8.3 is varied between 0 and 90 degrees, because the crane section is rotational symmetric over 90 degrees. This angle is of importance for the load distribution over the four columns. The horizontal distance e from the center of the crane structure to the point of application of downward displacement is varied over three distances, being approximately 10m, 20m and 40m. Finally the cross sectional area of the side bars is varied from its initial value to its doubled value.

8.3 Results

The collapse load of the crane structure is determined for a non-welded structure in subsection 8.3, followed by the results for the welded crane structure in subsection 8.3.

Non-welded crane structure

The collapse loads for the non-welded crane structure for the three different offset distances are shown as function of the slewing angle α in figure 8.4. In this graph the offset distance e is equal to 20 m. It can be seen that it holds in general that for increasing offset distance the collapse load decreases due to the larger induced bending moment at larger offset distance. Furthermore, the load capacity is maximum for angles of $\alpha = 0°$ and $\alpha = 90°$. In fact these load cases are identical because the crane structure is rotational symmetric over 90 degrees. The minimum load capacity is at an angle of $\alpha = 45°$. At this angle the neutral line of the cross section in the XY-plane of the crane structure lies diagonally, intersecting two columns. These columns only carry the vertical compressive force implied by the downward displacement, and do not carry the induced bending moment. The bending moment is fully carried by the remaining two diagonally opposed columns. This uneven load distribution over the columns causes the column closest to the point of displacement application to be loaded in the maximum amount of compression and is therefore the most prone to buckle prematurely.

In figure 8.4 the "dip" in load carrying capacity as function of the slewing angle appears to be less significant for increasing the offset distance e. This is an illusion due to the fact that the failure loads are presented in absolute sense. The relative failure load at $\alpha = 45°$ equals approximately 73% of the failure load at $\alpha = 0°$ for all considered offset distances.

The failure mode is determined by the slewing angle α. At an angle of 0 degrees the crane structure is bending in the XZ-plane under the applied load. The side bars oriented in this plane will provide resistance to column buckling in this same plane, however, the side bars oriented in the YZ-plane do not provide resistance against the bending deformation of the column. This is because the bars are modelled as two-force members, and therefore cannot carry any shear force or bending moment. All stiffness provided by

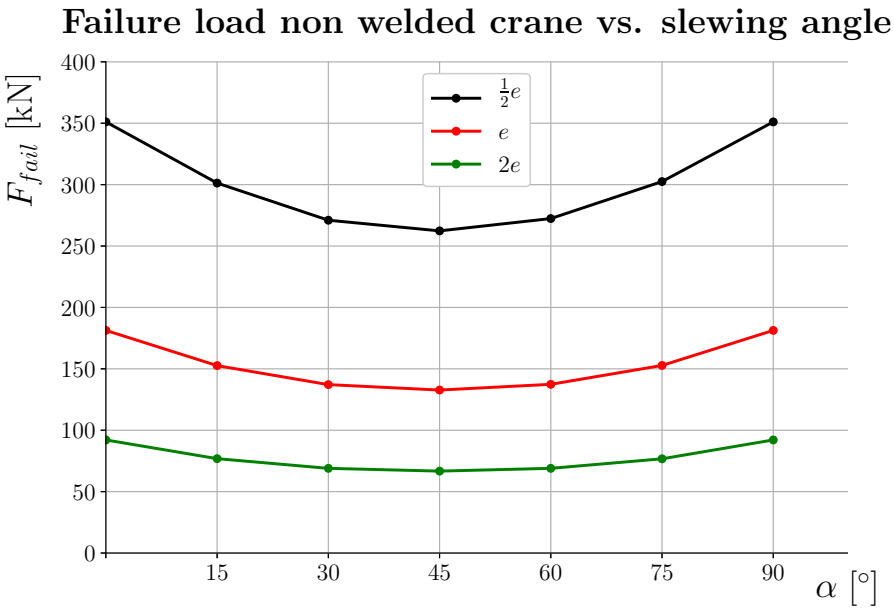

Figure 8.4: Collapse load for various offset distances as function of angle α

these bars lies in the YZ-plane. The failure mode for this load case is shown in figure 8.5, where the deformed state is scaled for clarification. The same behaviour and failure mode holds for the case where $\alpha = 90°$, but than rotated over 90 degrees. It should be kept in mind however that in reality a pure slewing angle of 0 and 90 degrees is exceptional. A slight imperfection may induce asymmetric load distribution and one of the four columns will buckle first, instead of two columns at the same instant as found for this load case.

For all considered angles except for $\alpha = 0°$ and $\alpha = 90°$ failure occurred according to the failure mode shown in figure 8.6. In this graph the deformation is scaled for clarification. As already explained, in these load cases the four columns are loaded unevenly, and the one closest to the point of displacement application is loaded in maximum compression. The side bars in these load cases however, all contribute to the restriction in bending deformation of this maximum loaded column. Eventually buckling occurs in the lower half of the this column, and the closer the slewing approaches 45 degrees, the lower this failure load is.

Doubling the cross sectional area of the side bars did not have any influence on the results compared with the here analyzed initial cross sectional area. This can also be deduced from the failure modes shown, as the column buckling already occurs between the connections of the side bars only, and not over the full length of the column.

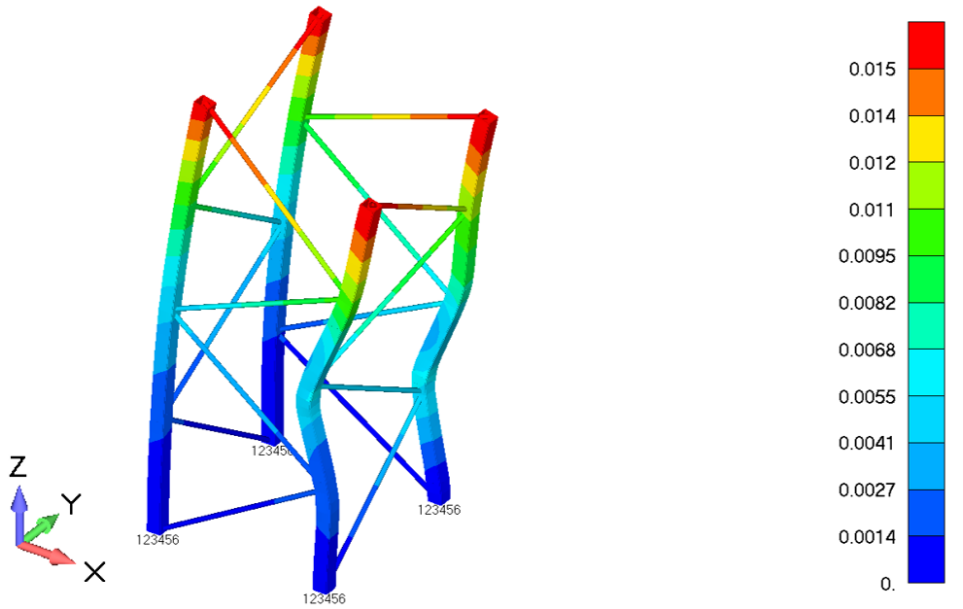

Figure 8.5: Total translation in buckled state for non-welded crane structure at $\alpha = 0$

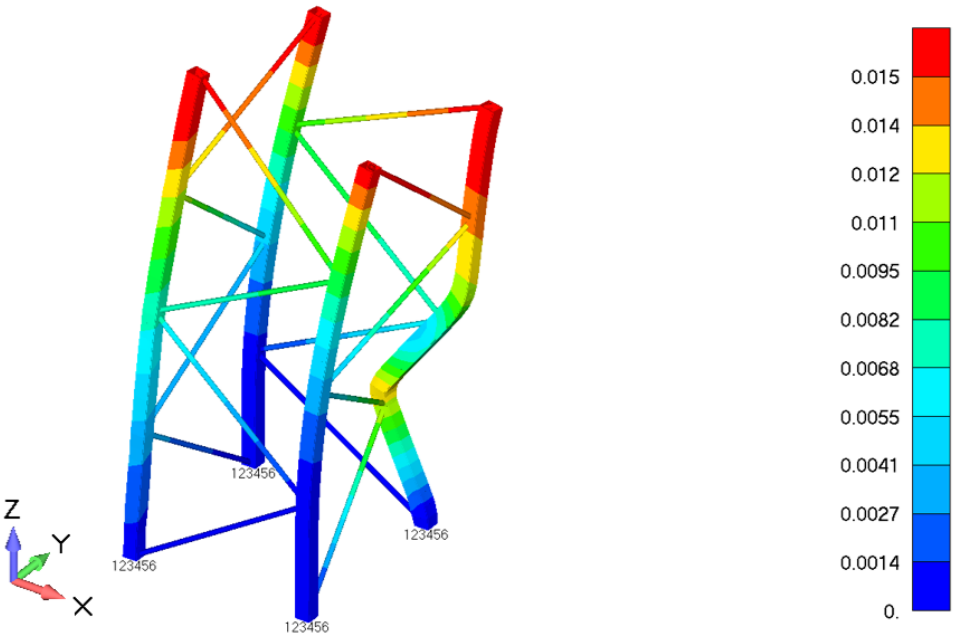

Figure 8.6: Total translation in buckled state for non-welded crane structure at $\alpha = 45$

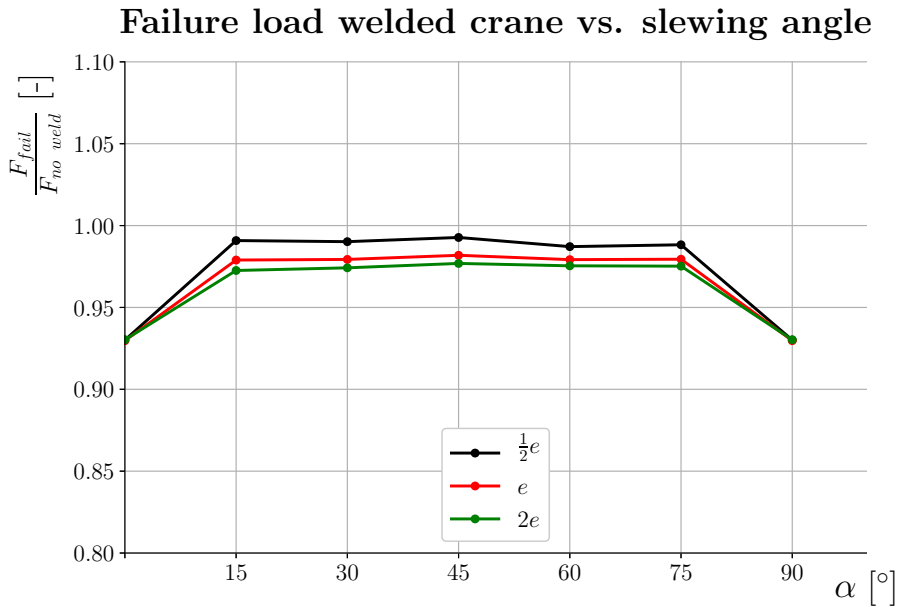

Figure 8.7: Ratio of welded vs. non-welded collapse load for various offset distances as function of angle α

Welded crane structure

The relative collapse load for the crane structure with two longitudinal welds over all four columns with respect to the non-welded structure is shown as function of the angle α in figure 8.7 for the three different offset distances. The variation in collapse load as function of the offset distance and angle α is similar as for the non-welded structure in figure 8.4. The minimum load capacity is again at an angle of 45 degrees with respect to the X-axis. The reduction in collapse load due to the longitudinal residual stress induced by the welds is quite stable for a wide range of angles α. This reduction is varying from 1% for an offset distance of 10m to a reduction of approximately 2.5% for an offset distance of 40m. The reduction in load capacity is slightly larger for increasing offset distance e. For larger offset distances a larger portion of the cross section of the column in maximum compression is loaded in heavy compression, and therefore plasticity will occur in a larger portion of the column, leading to premature buckling.

It can be clearly seen that the influence of the weld is maximum (7% reduction) at an angle of $\alpha = 0°$ and $\alpha = 90°$. In this load case the compressive force in the structure is applied evenly over the two columns closest to the point of displacement application. Only the side bars lying in the XZ-plane are able to resist the buckling of the columns, where in load cases with different angles of α all bars contributed to resist buckling of the columns. The

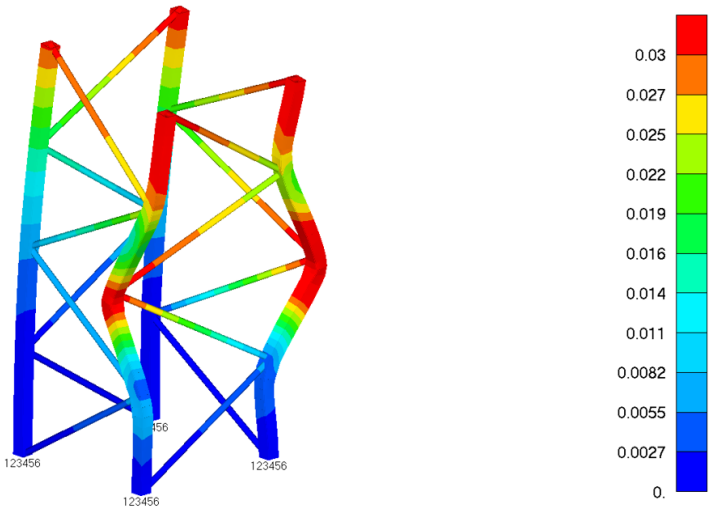

Figure 8.8: Total translation in buckled state for welded crane structure at $\alpha = 0$

failure modes for the welded crane sections at angles $\alpha = 0°$ and $\alpha = 45°$ are shown in figures 8.8 and 8.9 respectively. All buckled columns do buckle at mid length, and the failure mode for slewing angles other than 0 and 90 degrees are similar to the case where $\alpha = 45°$ in the sense that the shape of the buckled column is identical.

It is interesting to observe in the graph of figure 8.7 that the maximum reduction in failure load due to the weld is at slewing angles of 0 and 90 degrees. Referring back to the graph in figure 5.10 where the reduction in failure load for a clamped column is plotted as function of the slenderness ratio, it showed that the range of affected slenderness ratios is roughly between slightly less than 50 and 200. Due to the contribution of all side bars in load cases where $\alpha \neq 0°$ or $\alpha \neq 90°$, the side braces reduce the effective slenderness ratio of the column more than when $\alpha = 0°$ or $\alpha = 90°$, because then only a portion of the side bars contribute to a reduction in effective slenderness. The effective slenderness for cases where $\alpha \neq 0°$ or $\alpha \neq 90°$ is an increased distance to the left of $\frac{L}{\rho} = 80$ in figure 5.10 compared to cases where $\alpha = 0°$ or $\alpha = 90°$. Therefore an increased effect at these values for the slewing angles is expected.

As was the case for the non-welded crane structure, doubling the cross sectional area of the side bars did not have any influence on the results compared with the here analyzed initial cross sectional area. This can also be deduced from the failure modes shown, as the column buckling already occurs between the connections of the side bars only, and not over the full length of the column.

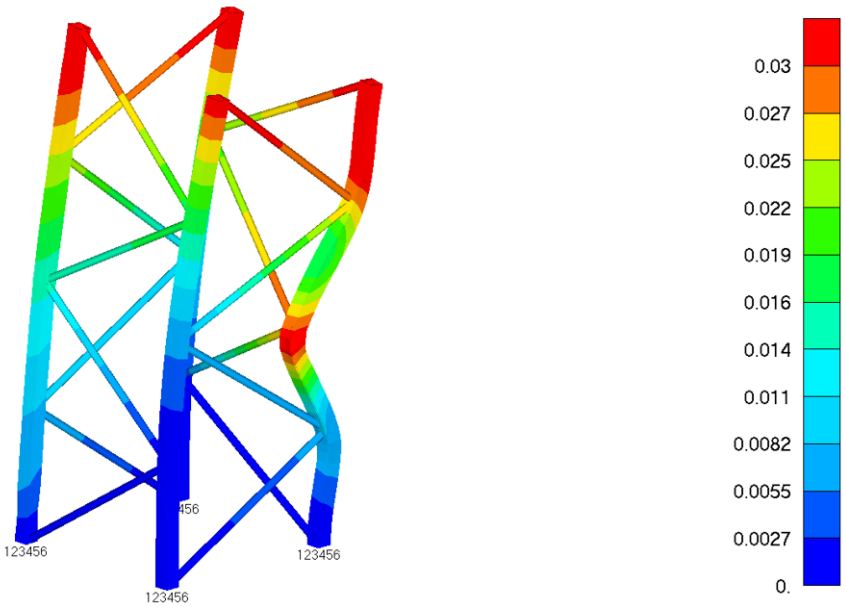

Figure 8.9: Total translation in buckled state for welded crane structure at $\alpha = 45$

Conclusions

Based on the experiment described in chapter 3 the following conclusions are drawn:

- For specimens A to F (all T-profiles) it is considered that a mean resulting curvature due to the welding process is hard to establish. The disturbance in the data may have been caused by the placement of the three tack welds along the specimen.
- Based on the measurements performed the resulting radii of curvature due to the welding process in specimen H (box-section) are 331m in the XY-plane and 275m in the ZX plane. It is doubtful if a reliable conclusion can be drawn based on the small measured curvature. The small resulting curvature is a result of two (almost) balancing deformations due to the two welds.
- The average axial shortening of the specimen may still provide information about the size of the two HAZs, but the measurements lack accuracy near the specimen's edges and therefore a reliable determination of the axial shortening based on this scanning data will be difficult.
- Based on the measurements performed the resulting radii of curvature due to the welding process in specimen G (L-profile) are 51m in the XY-plane and 48m in the ZX plane. Assuming the distribution of residual stresses as presented in subsection 3.1, the required total width of the HAZ is 23.3mm. This HAZ is asymmetrically distributed with the center of the plastic zone matching the Y-location of the actual weld.
- When the same approach is applied to specimen A (T-profile), a total HAZ width of 73mm is required to match the measured curvature. However, because the offset of the weld and the specimen's neutral axis is small, the obtained results are prone to assumptions about the HAZ centroid.

- The presence of a longitudinal weld in a both ended pinned column causes a significant reduction in compressive load capacity compared to a column without a longitudinal weld. This reduction is present for the various imperfections considered.
- The reduction is largest for columns in the range of intermediate slenderness ratios. For both stocky and slender columns the effect of the residual stresses is negligible, due to the dominance of other failure modes over the plasticity induced buckling.
- The effect of a longitudinal weld on the crane structure considered is less destructive compared to the single columns analysed.

Based on the finite element analyses performed in chapters 5, 6 and 7 the following conclusions are drawn:

- The presence of longitudinal residual stresses in a single column reduces its compressive load capacity for a certain range of slenderness ratios. The outer boundaries of the range of affected slenderness ratios is dependent on the boundary conditions, the width of the HAZ and whether or not imperfections are present.
- The maximum reduction due to welding residual stress slightly decreases with increasing amount of applied imperfection to the column.
- The upper boundary of the range of affected slenderness ratios is increasing for an increasing amount of imperfection.
- Both for the studied pinned and clamped columns made from material having an insignificant hardening modulus compared to the initial Young's modulus, and with a HAZ width equal to the found value in chapter 3, the maximum reduction in compressive load capacity is near 22%.
- For columns made from material with a hardening modulus near yielding of significant magnitude with respect to the initial Young's modulus, the maximum reduction in compressive load capacity is approximately 16%.
- For increasing width of the heat affected zone the amount of reduction in load capacity increases. At the maximum affected slenderness ratio this trend is approximately linear.
- The reduction factor on the load capacity due to welding induced residual stresses is the same for a column with imperfections due to load application offset as for a column with initial curvature, provided that the load offset distance at both ends is equal to the maximum deflection at mid length in case of initial curvature.

Based on the finite element analyses performed in chapter 8 the following conclusions are drawn:

- The collapse load of the modelled crane structure is minimum for a slewing angle of 45 degrees due to the uneven load distribution in the supporting columns.
- The reduction in collapse load due to the presence of longitudinal welds is ranging between 1% and 7%. The largest effect of the weld is reached when the slewing angle is at 0, 90, 180 or 270 degrees, because the effective slenderness of the considered column is then less reduced due to inactive side bars in the plane other than the bending plane.
- For slewing angles other than 0, 90, 180 or 270 degrees, the reduction in load capacity due to the presence of longitudinal residual stresses increases for increasing the offset distance where the compressive load is applied. However, the amount of added reduction for each increase in load offset is a decreasing trend.
- Increasing the cross sectional area of the side bars lead to the same results and did not improve performance of the considered structure.

Recommendations

Based on the experiments described in chapter 3 the following recommendations may be taken into account for future work:

- If used, tack welds should most likely be placed without an offset with respect to the full length weld line to maximize the homogeneity of the welding induced deformation.
- To study the occurring global curvature due to welding, the full length weld line as applied on the T-profiles can be placed more towards the midplane of the plates, for instance by means of chamfering, as done for the L- and box-profiles. In this way the shrinkage of the vertical section of the T-profile is more in-plane, reducing the likelihood of noise due to out-of-plane shrinkage.
- A measurement method should be used that is able to measure the specimen's ends with high accuracy. In this way a reliable axial deformation due to the welding process can be determined which is valuable for determining the residual stresses.
- The sensitivity of welding deformation as a function of the location of the center of shrinkage can be further investigated
- To exclude the possible effect of restricting the free deformation of the specimen due to the welding process, it is advised to place a plate that restricts translation in X-direction (as shown in figure A.7 in Appendix A) on one edge of the specimen only.

Based on the finite element analyses performed in chapters 5, 6 and 7 the following recommendations may be taken into account for future work:

- The effect of longitudinal residual stresses on the compressive load capacity may be further investigated for multiple layouts of welds along the column, and for columns with different cross sectional geometries.
- A similar study may be done for various distributions of residual stresses in the column, as these initial stresses may be caused by phenomena other than welding.

- The effect of longitudinal residual stresses on the compressive load capacity may be further investigated for material models with intermediate hardening moduli with respect to the initial Young's modulus, since the reduction in load capacity is different for materials showing high and low hardening moduli.

Based on the finite element analyses performed in chapter 8 the following recommendations may be taken into account for future work:

- The effect of longitudinal residual stresses on the compressive load capacity of a truss structure can be further investigated for truss structures where the slenderness ratio of the column structure is varied.
- The effect of various mechanical performance of the side bars in the truss structure may be further investigated. When the bars have significant dimensions compared to the columns, they are capable of carrying shear forces and bending moments. This likely will have an effect on the compressive load capacity of the total structure.
- The minimal required cross sectional properties of the side bars to induce a certain buckling mode of the crane structure can be further investigated.
- Similar analyses as in chapter 8 can be run with multiple crane sections on top of each other. In this way the boundary conditions at mid height of the structure will more and more according to reality. This may likely have an effect on the structure's performance in compression.

Bibliography

[1] Artem Pilipenko. *Computer simulation of residual stress and distortion of thick plates in multi-electrode submerged are welding. Their mitigation techniques.* PhD thesis, Norwegian University of Science and Technology Trondheim, 2001.

[2] De Onderzoeksraad Voor Veiligheid. Bezwijken torenkraan rotterdam 10 juli 2008, 2009.

[3] Charles Francis Walton and Timothy J Opar. *Iron castings handbook: covering data on gray, malleable, ductile, white, alloy and compacted graphite irons.* Iron Castings Society, 1981.

[4] Welding Handbook. Fundamentals of welding. *American Welding Society*, 1, 1976.

[5] Boverkets Handbok om Stålkonstruktioner. *BSK 94.* Boverket, byggavdelningen, 1997.

[6] Adam J Sadowski, J Michael Rotter, Peter J Stafford, Thomas Reinke, and Thomas Ummenhofer. On the gradient of the yield plateau in structural carbon steels. *Journal of Constructional Steel Research*, 130:120–130, 2017.

[7] EN 1993-1-1. Eurocode 3: Design of steel structures. part 1.1: General rules and rules for buildings, 2005.

[8] Lloyds Register. Code for lifting appliances in a marine environment, 2017.

[9] R. H. Leggatt. Residual stresses in welded structures. *International Journal of Pressure Vessels and Piping*, 85(3):144–151, 2008.

[10] E Armentani, R Esposito, and R Sepe. The effect of thermal properties and weld efficiency on residual stresses in welding. *Manufacturing Engineering*, 20(January):319–322, 2007.

[11] G. den Ouden and MJM Hermans. *Welding technology.* VSSD Delft, 2009.

[12] Jagabandhu Chakrabarty. *Applied plasticity, second edition*. Springer, 2010.

[13] Jean-Louis Batoz and Gouri Dhatt. Incremental displacement algorithms for nonlinear problems. *International Journal for Numerical Methods in Engineering*, 14(8):1262–1267, 1979.

Appendices

Appendix A

Photographs of welding experiment

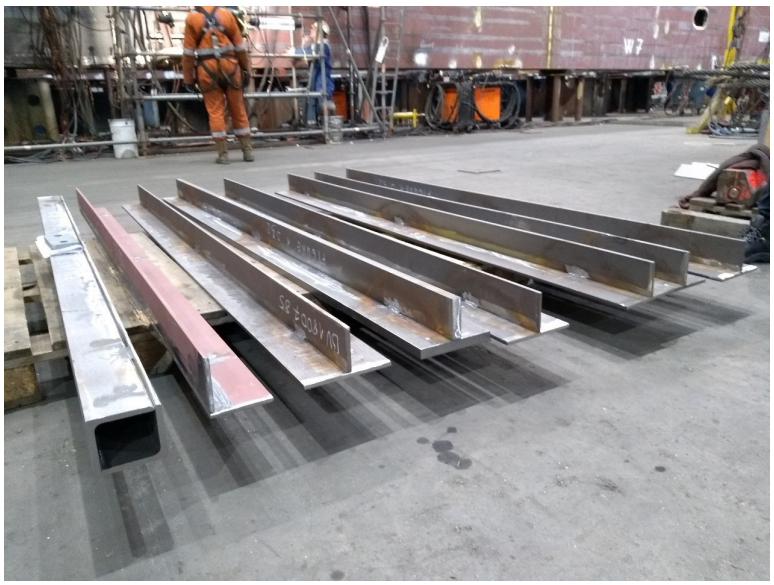

Figure A.1: Overview of all welded specimens

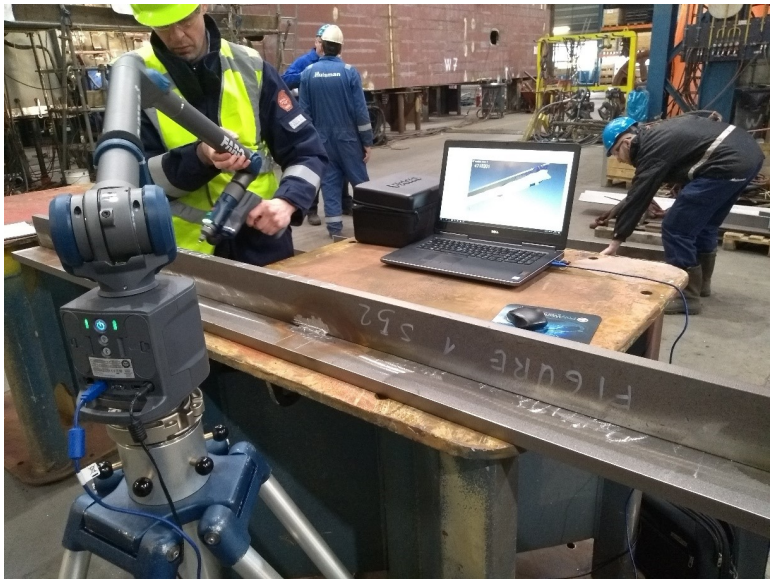

Figure A.2: Scanning procedure with measurement arm

Figure A.3: Scanning of edge geometry with measurement arm

Figure A.4: Use is made of mechanized welding machine for better weld consistency

Figure A.5: Welding process in action

Figure A.6: Boundary condition of one edge of specimen during welding

Figure A.7: Boundary condition of other edge of specimen during welding

Figure A.8: End of full length weld on specimen

Figure A.9: Post welding deformation clearly visible with naked eye

Appendix B

Best-fit of reference points

A			
Point 1			
	Nom.	Meas.	Dev.
X	2259.067	2258.977	-0.090
Y	100.351	100.351	0.000
Z	94.364	94.364	0.000
Point 2			
	Nom.	Meas.	Dev.
X	265.69	265.721	0.031
Y	99.128	99.133	0.005
Z	107.24	107.208	-0.032
Point 3			
	Nom.	Meas.	Dev.
X	265.151	265.209	0.058
Y	101.17	101.165	-0.005
Z	94.824	94.856	0.032

B			
Point 1			
	Nom.	Meas.	Dev.
X	110.515	110.627	0.112
Y	99.444	99.445	0.001
Z	85.475	85.456	-0.019
Point 2			
	Nom.	Meas.	Dev.
X	2333.218	2333.091	-0.127
Y	90.377	90.4	0.023
Z	84.991	84.707	-0.284
Point 3			
	Nom.	Meas.	Dev.
X	2196.023	2196.039	0.016
Y	88.717	88.693	-0.024
Z	113.139	113.441	0.302

Figure B.1: Best fit data for specimen A and B

C			
Point 1			
	Nom.	Meas.	Dev.
X	248.197	248.135	-0.062
Y	100.617	100.617	0.000
Z	104.339	104.339	0.000
Point 2			
	Nom.	Meas.	Dev.
X	2255.597	2255.62	0.023
Y	97.986	97.986	0
Z	93.597	93.606	0.009
Point 3			
	Nom.	Meas.	Dev.
X	2255.369	2255.408	0.039
Y	98.777	98.777	0
Z	105.757	105.749	-0.008

D			
Point 1			
	Nom.	Meas.	Dev.
X	2251.39	2251.299	-0.091
Y	100.937	100.937	0.000
Z	94.334	94.334	0.000
Point 2			
	Nom.	Meas.	Dev.
X	252.961	253.015	0.054
Y	100.367	100.367	0
Z	106.431	106.418	-0.013
Point 3			
	Nom.	Meas.	Dev.
X	252.499	252.535	0.036
Y	100.175	100.176	0.001
Z	94.178	94.191	0.013

Figure B.2: Best fit data for specimen C and D

E			
Point 1			
	Nom.	Meas.	Dev.
X	2246.797	2246.779	-0.018
Y	100.42	100.419	-0.001
Z	94.256	94.256	0.000
Point 2			
	Nom.	Meas.	Dev.
X	252.9	252.966	0.066
Y	99.013	99.017	0.004
Z	106.423	106.402	-0.021
Point 3			
	Nom.	Meas.	Dev.
X	246.934	246.885	-0.049
Y	101.745	101.74	-0.005
Z	94.086	94.107	0.021

F			
Point 1			
	Nom.	Meas.	Dev.
X	246.994	247.397	0.403
Y	98.211	98.211	0.000
Z	106.358	106.356	-0.002
Point 2			
	Nom.	Meas.	Dev.
X	2251.225	2250.929	-0.296
Y	98.493	98.491	-0.002
Z	93.49	93.461	-0.029
Point 3			
	Nom.	Meas.	Dev.
X	2244.284	2244.178	-0.106
Y	99.154	99.156	0.002
Z	106.248	106.279	0.031

Figure B.3: Best fit data for specimen E and F

G			
Point 1			
	Nom.	Meas.	Dev.
X	2239.42	2239.621	0.201
Y	108.305	108.305	0.000
Z	-1.506	-1.508	-0.002
Point 2			
	Nom.	Meas.	Dev.
X	253.032	253.108	0.076
Y	103.514	103.534	0.02
Z	-1.49	-1.415	0.075
Point 3			
	Nom.	Meas.	Dev.
X	247.443	247.167	-0.276
Y	106.821	106.8	-0.021
Z	10.752	10.679	-0.073

H			
Point 1			
	Nom.	Meas.	Dev.
X	2247.548	2247.274	-0.274
Y	12.953	12.953	0.000
Z	101	101	0.000
Point 2			
	Nom.	Meas.	Dev.
X	248.931	249.128	0.197
Y	13.278	13.323	0.045
Z	101.097	101.156	0.059
Point 3			
	Nom.	Meas.	Dev.
X	248.222	248.299	0.077
Y	-0.361	-0.406	-0.045
Z	83.202	83.144	-0.058

Figure B.4: Best fit data for specimen G and H

Appendix C

Python scripts used

C.1 Extract Data from point cloud

```
"""This module extracts the data points with maximum Y
   -coordinate for a user specified number of points
    """

__author__ = "Sander Hoogendorp"

import numpy as np
import matplotlib.pyplot as plt
from time import clock


# USER DEFINED FUNCTIONS

def read_line(file_object):

    """Generates 1 line of the file-object argument's
       content"""

    while True:
        line = file_object.readline()
        if not line:
            break
        yield line


def get_section_data(file_name, xmin, xmax):

    """Generates tuple with data point coordinates in
```

```
        specified X-range"""

    with open(file_name, "r") as f:

        for line in read_line(f):
            x, y, z = [float(coord) for coord in line.
                split(",")]
            if xmin < x < xmax:
                yield (x, y, z)


def data_generator(file_name):

    """Generates tuple with data point coordinates"""

    with open(file_name, "r") as f:

        for line in read_line(f):
            x, y, z = [float(coord) for coord in line.
                split(",")]
            yield (x, y, z)


# USER INPUT

file = "Gvoor.txt"
nr_points = 250
write_output = False

# DETERMINE XYZ RANGES OF MEASURED DATA

print("Extracting {} points from {}...".format(
    nr_points, file))

t1 = clock()

data1 = data_generator(file)

# Initialize xyz coordinates with first occuring data
    point
x_init, y_init, z_init = next(data1)

x_min = x_init
x_max = x_init
```

```
y_min = y_init
y_max = y_init

z_min = z_init
z_max = z_init

for coord in data1:
    x, y, z = coord
    if x < x_min:
        x_min = x
    if x > x_max:
        x_max = x
    if y < y_min:
        y_min = y
    if y > y_max:
        y_max = y
    if z < z_min:
        z_min = z
    if z > z_max:
        z_max = z

x_min_margin_incl = x_min - 1.
x_max_margin_incl = x_max + 1.

print("XYZ range determined")

# DETERMINE TOP Y COORDINATE OF EACH SECTION

data2 = data_generator(file)

# Initialize array with top Y data points
top_points = np.zeros((nr_points, 3))
top_points[:, 1] = y_min * np.ones((nr_points,))

section_length = (x_max_margin_incl -
   x_min_margin_incl) / nr_points

for coord in data2:
    x, y, z = coord

    # Floor division
    row_index = int(abs(x) // section_length)
```

```
        if y > top_points[row_index, 1]:
            top_points[row_index, 0] = x
            top_points[row_index, 1] = y
            top_points[row_index, 2] = z

print("Data points extracted")

plt.subplot(211)
plt.plot(top_points[:, 0], top_points[:, 1], "x",
    color="red")
plt.title("{} Y vs. X".format(file))
plt.ylabel("Y [mm]")
ax = plt.gca()
ax.set_xlabel("X [mm]",x=1,y=1)

plt.subplot(212)
plt.plot(top_points[:, 0], top_points[:, 2], "x",
    color="blue")
plt.title("{} Z vs. X".format(file))
ax = plt.gca()
ax.set_xlabel("X [mm]",x=1,y=1)
plt.ylabel("Z [mm]")
plt.show()

# IF REQUESTED, WRITE EXTRACTED DATA POINTS TO NEW .
    TXT FILE

if write_output:

    output_file = file.split(".")[0] + "_" + str(
        nr_points) + ".txt"

    with open(output_file, "w") as w:

        w.write("Xmin {}\n".format(x_min))
        w.write("Xmax {}\n".format(x_max))
        w.write("Ymin {}\n".format(y_min))
        w.write("Ymax {}\n".format(y_max))
        w.write("Zmin {}\n".format(z_min))
        w.write("Zmax {}\n".format(z_max))

        for row in range(np.shape(top_points)[0]):

            x = top_points[row, 0]
```

```
            y = top_points[row, 1]
            z = top_points[row, 2]

            w.write("{} {} {}\n".format(x, y, z))

t2 = clock()
print("It took {} seconds".format(t2-t1))
```

C.2 Interpolation of pre- and post-weld data

```
"""This module prints array with X-values and Y-values
    based on linear interpolating post-welded
   deformation"""

__author__ = "Sander Hoogendorp"

import numpy as np
from time import clock

# USER INPUT

# File to read X-coordinates from
before_file = "Hvoor_XY_250.txt"

# File with raw measurement points to extract Top Y-
   coordinates from
after_file = "Hna_XY_250.txt"

# STORE DATA IN ARRAYS AND SHRINK "AFTER ARRAY" TO FIT
    X-VALUES IN "BEFORE ARRAY"

t1 = clock()

data_before = np.genfromtxt(fname=before_file,
   skip_header=6, delimiter=" ")
data_after = np.genfromtxt(fname=after_file,
   skip_header=6, delimiter=" ")

# Check whether X-values in "data_before-array" are
   within range of "data_after-array"
while data_before[0, 0] < data_after[0, 0]:
    data_before = data_before[1:, :]

while data_before[-1, 0] > data_after[-1, 0]:
```

```
    data_before = data_before[:-1, :]

x_values = data_before[:, 0]

# INTERPOLATE

nr_of_x_values = np.shape(x_values)[0]
y_values = np.zeros(nr_of_x_values)

for i in range(nr_of_x_values):

    for j in range(np.shape(data_after)[0]-1):

        if x_values[i] > data_after[j, 0] and x_values
           [i] < data_after[j + 1, 0]:

            start = data_after[j, 1]
            offset = x_values[i] - data_after[j, 0]
            slope = (data_after[j + 1, 1] - data_after
               [j, 1]) / (data_after[j + 1, 0] -
               data_after[j, 0])
            y_values[i] = start + offset * slope

            break

print(x_values.reshape((np.shape(x_values)[0], 1)))
print(y_values.reshape((np.shape(x_values)[0], 1)))

t2 = clock()
print("It took {} seconds".format(t2-t1))
```

C.3 Interpolation of pre- and post-weld data

```
"""This module prints the X- and Y/Z-location of the
   best circle fit, its radius and residu, based on
   the .txt input file
 specified in the "filename" variable. An array with
    points on the circle is also printed.
 Use is made of published code on "https://scipy-
    cookbook.readthedocs.io/items/Least_Squares_Circle
    .html"."""

__author__ = "Sander Hoogendorp"
```

```
from scipy import optimize
import matplotlib.pyplot as plt
import numpy as np

# USER DEFINED FUNCTIONS


def calc_R(xc, yc):
    """ calculate the distance of each 2D points from
        the center (xc, yc) """

    return np.sqrt((x - xc) ** 2 + (y - yc) ** 2)


def f_2(c):
    """ calculate the algebraic distance between the
        data points and the mean circle centered at c=(
        xc, yc) """

    Ri = calc_R(*c)

    return Ri - Ri.mean()


# USER INPUT

filename = "H_XY_curve.txt"

# READ FILE AND STORE DATA POINTS IN ARRAY

data = np.genfromtxt(fname=filename, delimiter=" ")

x_min = data[0, 0]
x_max = data[-1, 0]

x = data[:, 0]
y = data[:, 1]

# READ FILE AND STORE DATA POINTS IN ARRAY

# Initial guess of circle center
x_m = np.average(x)
y_m = y[0]
```

```
# Floor division to find approximate mid-index of
    array
mid_index = len(y) // 2

if y[mid_index] > y[0] and y[mid_index] > y[-1]:
    sign = 1
elif y[mid_index] < y[0] and y[mid_index] < y[-1]:
    sign = -1
else:
    print("No curvature direction established")
    raise Exception

center_estimate = x_m, y_m
center_2, ier = optimize.leastsq(f_2, center_estimate)

xc_2, yc_2 = center_2
Ri_2 = calc_R(*center_2)
R_2 = Ri_2.mean()
residu_2 = sum((Ri_2 - R_2) ** 2)

test_x = np.linspace(x_min, x_max, len(y))
test_y = sign * np.sqrt(R_2 ** 2 - (test_x - xc_2) **
    2) + yc_2

print(xc_2)
print(yc_2)
print(R_2)
print(residu_2)

plt.plot(x, y, "x", color="red", label="Displacement
    data")
## plt.plot(xc_2, yc_2, "x", color="blue")
plt.plot(test_x, test_y, color="green", label="Circle
    fit")
plt.title("Y vs X for specimen H")
plt.xlabel("X [mm]")
plt.ylabel("Y [mm]")
plt.legend()
plt.show()

print(np.hstack((test_x.reshape((len(test_x), 1)),
    test_y.reshape((len(test_y), 1)))))
```

Appendix D

Specimen circle fit data

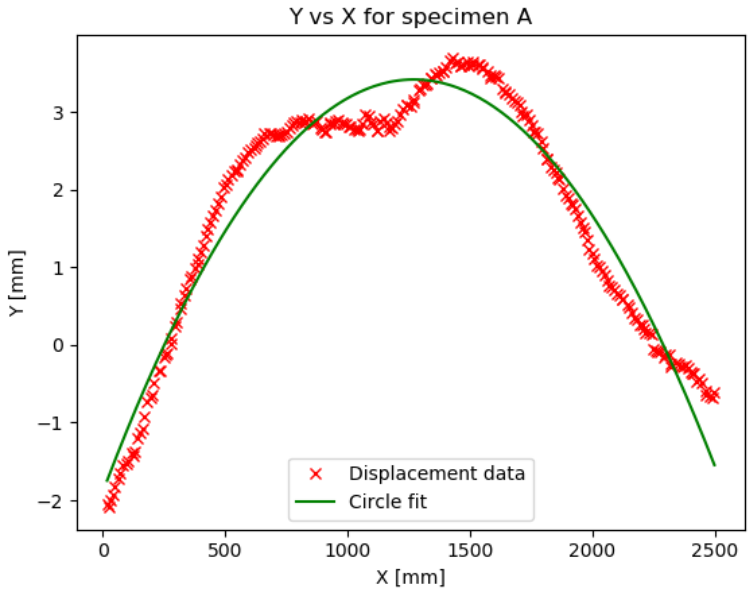

Figure D.1: Circle fit (green) in XY-plane for specimen A

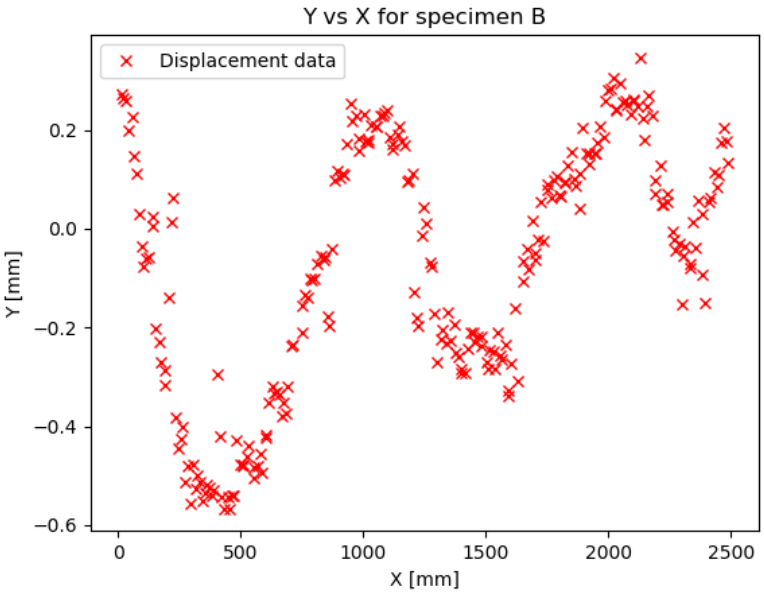

Figure D.2: Circle fit (green) in XY-plane for specimen B

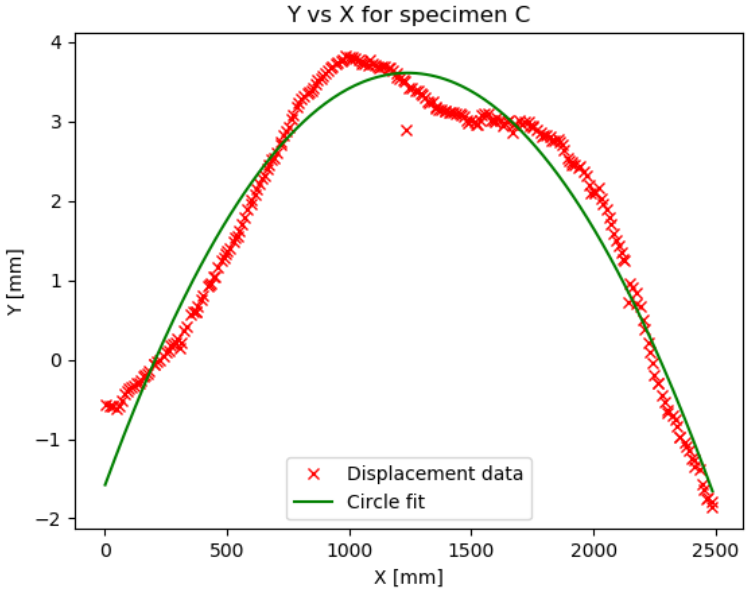

Figure D.3: Circle fit (green) in XY-plane for specimen C

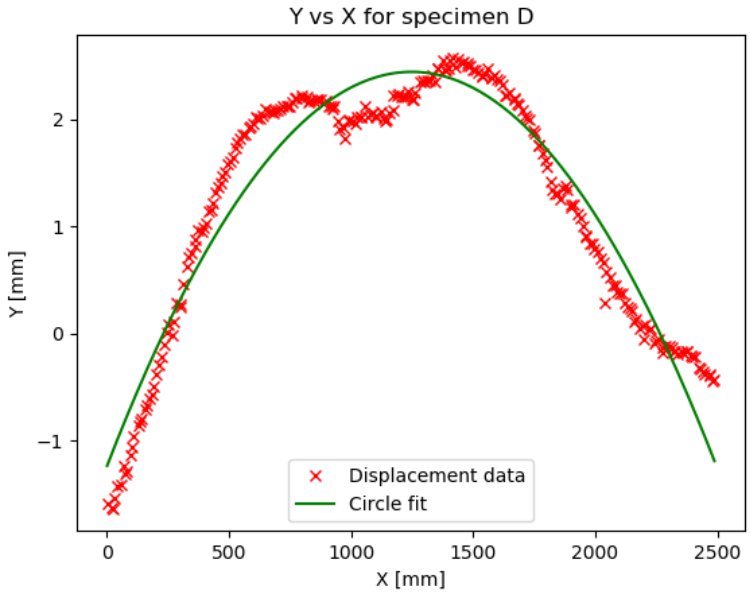

Figure D.4: Circle fit (green) in XY-plane for specimen D

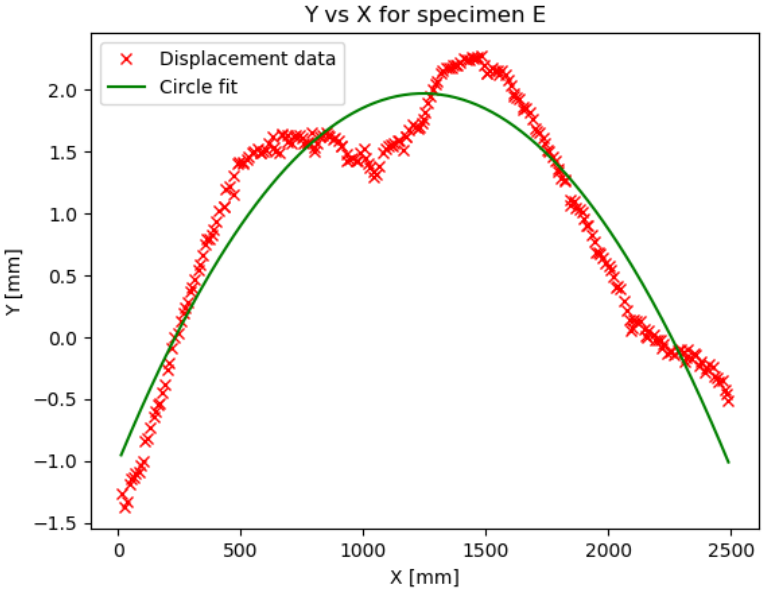

Figure D.5: Circle fit (green) in XY-planefor specimen E

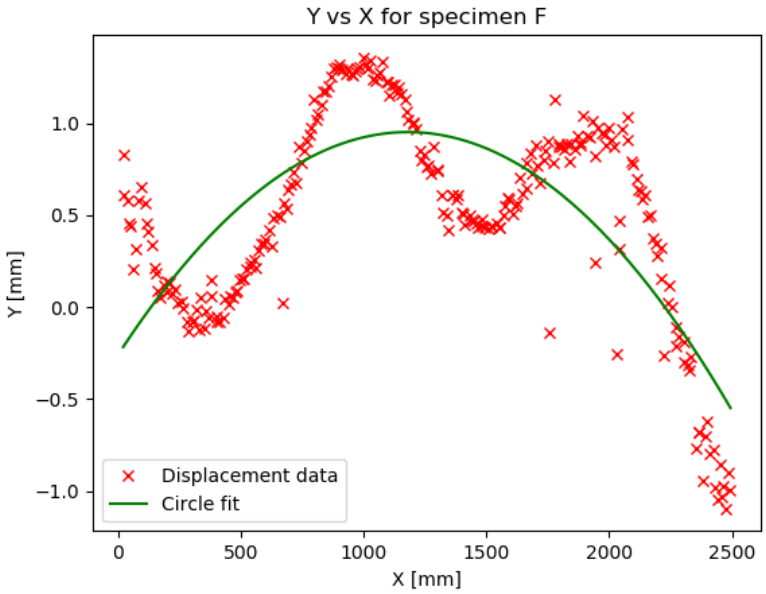

Figure D.6: Circle fit (green) in XY-plane for specimen F

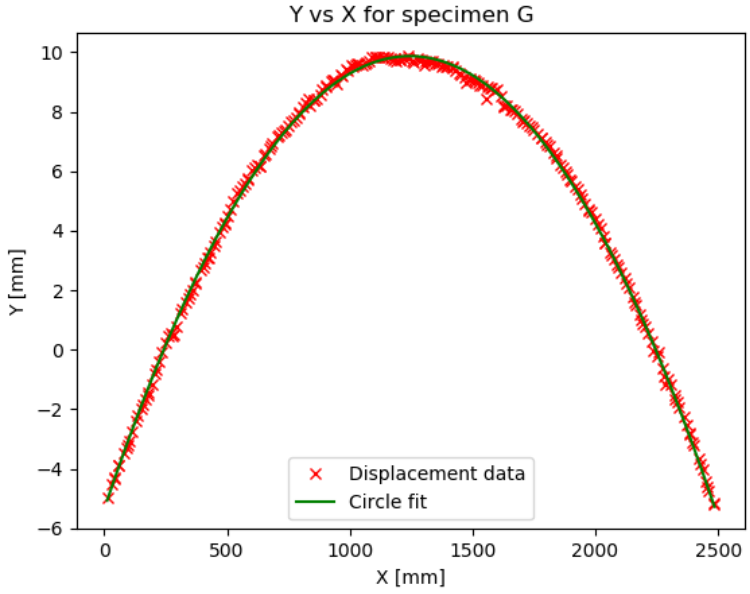

Figure D.7: Circle fit (green) in XY-plane for specimen G

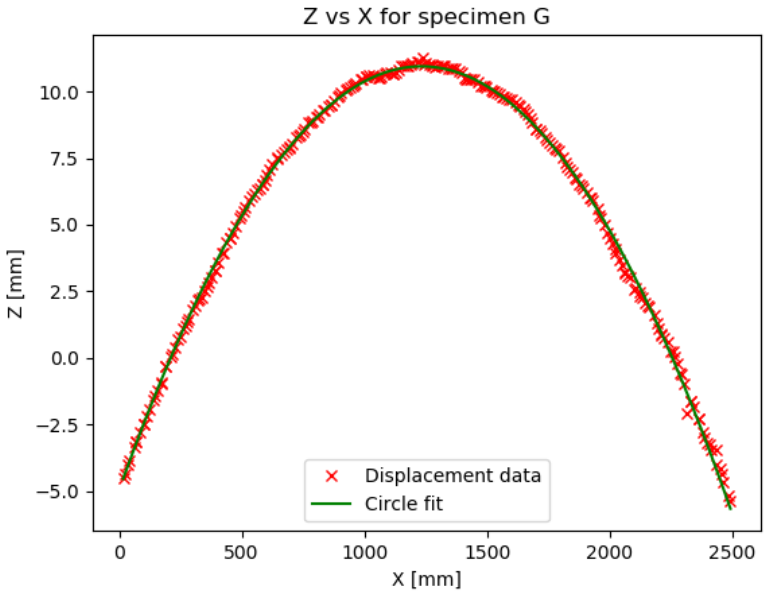

Figure D.8: Circle fit (green) in XZ-plane for specimen G

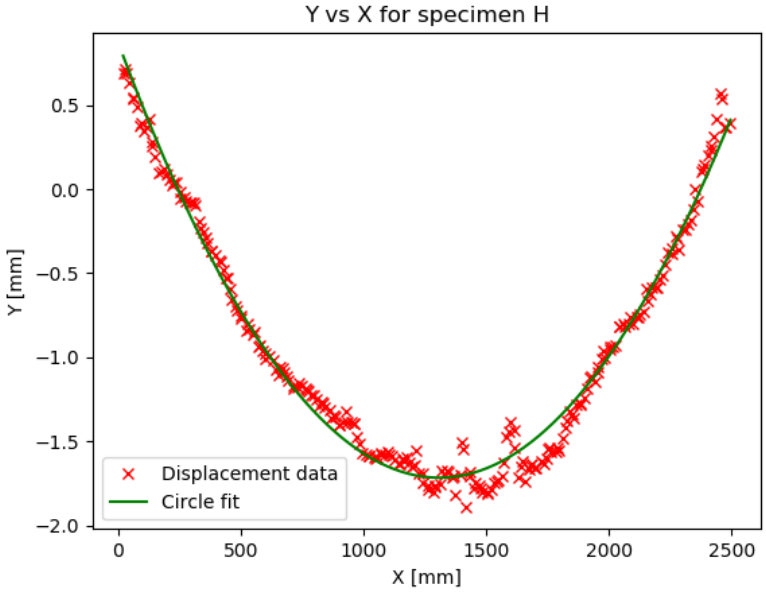

Figure D.9: Circle fit (green) in XY-plane for specimen H

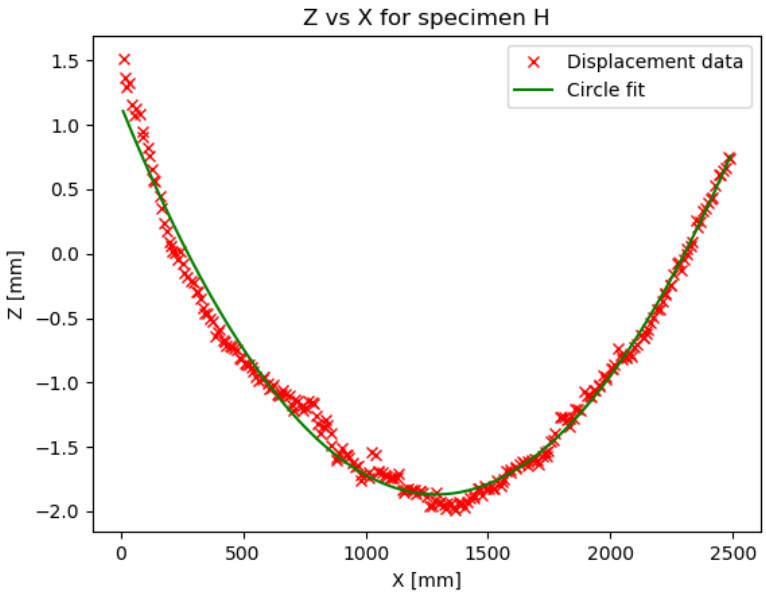

Figure D.10: Circle fit (green) in XZ-plane for specimen H